

Spring 2012

Development of an expedited objective fracture severity assessment methodology

Anthony Thomas Kilburg
University of Iowa

Copyright 2012 Anthony T. Kilburg

This thesis is available at Iowa Research Online: <https://ir.uiowa.edu/etd/2916>

Recommended Citation

Kilburg, Anthony Thomas. "Development of an expedited objective fracture severity assessment methodology." MS (Master of Science) thesis, University of Iowa, 2012.
<https://doi.org/10.17077/etd.u4zrehm2>

Follow this and additional works at: <https://ir.uiowa.edu/etd>

Part of the [Biomedical Engineering and Bioengineering Commons](#)

DEVELOPMENT OF AN EXPEDITED OBJECTIVE FRACTURE SEVERITY
ASSESSMENT METHODOLOGY

by
Anthony Thomas Kilburg

A thesis submitted in partial fulfillment
of the requirements for the Master of
Science degree in Biomedical Engineering
in the Graduate College of
The University of Iowa

May 2012

Thesis Supervisor: Associate Professor Donald D. Anderson

Graduate College
The University of Iowa
Iowa City, Iowa

CERTIFICATE OF APPROVAL

MASTER'S THESIS

This is to certify that the Master's thesis of

Anthony Thomas Kilburg

has been approved by the Examining Committee
for the thesis requirement for the Master of Science
degree in Biomedical Engineering at the May 2012 graduation.

Thesis Committee: _____
Donald D. Anderson, Thesis Supervisor

Thomas D. Brown

Joseph M. Reinhardt

J. Lawrence Marsh

ACKNOWLEDGMENTS

I would like to thank all the people who helped me during my time at the University of Iowa. I certainly would not be where I am today without the help and guidance of these people. I would first like to sincerely thank my research advisors from the University of Iowa Orthopaedic Biomechanics Laboratory (OBRL), Drs. Don Anderson and Tom Brown. They have been two strong guiding forces for me in my education and research. Their knowledge, expertise, and commitment to the field of Orthopaedics and Biomechanics are truly an inspiration. I would additionally like to thank the other members of my committee, Drs. J. Lawrence Marsh and Joseph Reinhardt for their helpful analysis and input to my work. I would like to thank the funding for my research, provided by the NIH NIAMS Program Grant P50 AR055533 and AR048939. The students and faculty of the OBRL not already mentioned have provided great additional support through conversations and discussions about their and my work. I owe them a great deal of gratitude for advancing and broadening my research even further. I would last like to thank my friends and family. Their guidance, love, and support have helped me all through my life.

TABLE OF CONTENTS

LIST OF TABLES	v
LIST OF FIGURES	vi
LIST OF EQUATIONS	ix
PREFACE	x
CHAPTER ONE: INTRODUCTION.....	1
CHAPTER TWO: LITERATURE REVIEW.....	3
The Ankle	3
Major Anatomical Structures	3
Tibial Plafond Fractures	4
Fracture Characteristics	5
Post-traumatic Osteoarthritis (PTOA).....	7
Treatment and Surgical Decision-Making.....	7
Development of Post-Traumatic Osteoarthritis.....	8
Post-traumatic OA Classification.....	11
Computed Tomography (CT)	14
Full Fracture Severity Metric.....	17
Basis of Calculation.....	17
Additional Fracture Severity Components.....	18
Results and Limitations	21
The Rationale for an Expedited Fracture Severity Metric.....	22
CHAPTER THREE: METHODS.....	24
Gray Level Co-occurrence Matrix (GLCM).....	25
Description and Input Parameters	25
Input Parameters Chosen.....	28
GLCM Heterogeneity Property	30
Expedited Metric Preparation.....	32
Watershed Segmentation.....	32
Post Segmentation Setup.....	34
Post GLCM Analysis Setup.....	36
Normalization of Intact Contralateral Limb	38
CT Convolution Kernel	39
CT Image Spatial Scaling.....	45
Intact Surrogate Curve.....	51
Calculation of Severity Components.....	52
Fracture Energy Surrogate.....	52
Dispersion.....	53
Articular Comminution	55
Combined Metric.....	57
CHAPTER FOUR: RESULTS	58
Articular Slice Location.....	59
Expedited Severity Component Results	61
Comparison to Initial Severity Metric	64
Severity Components.....	64

Concordance with KL scores.....	68
OA Development Comparison	71
Calculation Time	74
CHAPTER FIVE: DISCUSSION.....	78
Inter-/Intra-User Variability.....	78
Variability Test Setup.....	78
Segmentation Comparison.....	79
Articular Slice Comparison	82
Severity Results Comparison	83
Advantages of the Expedited Severity Metric.....	85
Future Applications	86
Clinical Application.....	86
Translation to Other Joints	87
Major Extremity Trauma Research Consortium (METRC).....	88
Limitations.....	88
CHAPTER 6: CONCLUSION	91
APPENDIX A: EXPEDITED FRACTURE SEVERITY ANALYSIS: USER MANUAL.....	93
REFERENCES	110

LIST OF TABLES

Table 1: KL score characteristics and delineation.....	13
Table 2: Results of varying ROI's for articular disruption using dispersion.....	57
Table 3: Patient age, sex, height, weight, in-plane pixel size (mm), CT image slice thickness (mm), and convolution kernel used in CT image reconstruction for each case.....	59
Table 4: Severity component results from expedited metric analysis.....	61
Table 5: Normalized components and combined scores for expedited severity metric.....	63
Table 6: Contingency table for a threshold value of 27.75.....	73

LIST OF FIGURES

Figure 1: The ankle joint structures and major landmarks.[3].....	4
Figure 2: Large compressive forces delivered to the tibia through the talus can result in complex fractures of the tibial plafond.[8].....	5
Figure 3: Variation in comminution for fractures of the tibial plafond. © 1994 American Academy of Orthopaedic Surgeons. Reprinted from the <i>Journal of the American Academy of Orthopaedic Surgeons</i> , Volume 2 (6), pp. 297-305 with permission.	6
Figure 4: AO/OTA fracture classification system. © 1994 American Academy of Orthopaedic Surgeons. Reprinted from the <i>Journal of the American Academy of Orthopaedic Surgeons</i> , Volume 2 (6), pp. 297-305 with permission.	8
Figure 5: Degeneration of articular cartilage resulting in post-traumatic OA [28-30].....	9
Figure 6: Example radiographs of differing KL scores in the knee. [47].....	13
Figure 7: X-rays being transmitted through a 2D area and collected on a 1D detector. The convolution kernel chosen to reconstruct the 2D area can influence the resulting texture of the image.	15
Figure 8: Image texture differences between convolution kernels for the same image.	16
Figure 9: The effects of metal artifact on CT image quality and texture.....	16
Figure 10: Interfragmentary surface area calculation for a fractured tibia [52].	19
Figure 11: Calculation of fragment dispersion/displacement.	20
Figure 12: GLCM image analysis example showing the results of the linear scaling method used on images.	26
Figure 13: GLCM before and after a GLCM analysis was run on the rescaled image of Figure 12.	26
Figure 14: Differences between GLCM's with and without the symmetry option.	28
Figure 15: Image adjustment parameters applied to a CT image.	29
Figure 16: Neighboring pixel offsets chosen for the GLCM analysis.	29
Figure 17: Homogeneity comparison (intact vs. fractured limbs).	31
Figure 18: Effect of differing threshold values on the watershed segmentation.	33

Figure 19: Unwanted fragments from the tibia segmentation. Unwanted fragments are not part of the tibia and want to be excluded from the GLCM analysis.	34
Figure 20: Watershed segmentation and convex hull results.....	35
Figure 21: Distal fragment removal from convex hull.	36
Figure 22: Articular slice selection graph and ensuing slice location.	37
Figure 23: Initial distribution of heterogeneity summations.....	39
Figure 24: Convolution kernel effects on CT images.....	39
Figure 25: Effects of diffusion time step-size on calculation time and heterogeneity.....	42
Figure 26: Effects of diffusion step-size on CT images.	42
Figure 27: Effects of total diffusion time on calculation time and heterogeneity.	43
Figure 28: Effects of total diffusion time on CT images.....	43
Figure 29: Effect of anisotropic diffusion filter on CT image and image heterogeneity.	44
Figure 30: Effect of convolution kernel adjustment on heterogeneity summation.....	45
Figure 31: Effect on heterogeneity of the image area analyzed.....	46
Figure 32: Effect of in-plane pixel size on image texture.....	49
Figure 33: Effect of CT image spatial adjustments on heterogeneity summation.....	50
Figure 34: Effect of anthropometric adjustments on heterogeneity summation.....	51
Figure 35: Proximal and distal curve fittings to the surrogate intact heterogeneity distribution data.....	52
Figure 36: Example showing 1-1 relationship (green) differences between the intact and fractured limbs. The 1-1 relationship is used to determine fragment dispersion.....	54
Figure 37: Differences in surrogate curves around the articular region with 4 different slopes isolated showing the variation seen in this region.....	56
Figure 38: These CT images are from the slices identified as involving the articular surface for each case.....	60
Figure 39: 1-1 relationship at the proximal end of the tibia with medullary cavity area included (Left) and the distal end where bone is tailing off (Right). (Convex Hull - Green, 1-1 Relationships - Red).....	62
Figure 40: Comparison between expedited severity components' normalized values.....	63

Figure 41: Correlation between expedited and initial severity values for fracture energy (Problem cases in red).	65
Figure 42: Comparison between expedited and full severity metrics' overall dispersion and displacement values.	66
Figure 43: Comparison between the normalized expedited severity metric and the normalized full severity metric articular disruption values.....	67
Figure 44: Comparison between combined severity scores for the expedited and full severity metrics (for the original 20 cases).	68
Figure 45: Comparison between normalized expedited severity components and KL scores.	70
Figure 46: Comparison between the combined severity scores of the expedited metric and the KL scores.....	70
Figure 47: Comparison between the expedited severity values for cases with OA vs. no OA development.....	72
Figure 48: Receiver Operating Characteristic (ROC) curve for varying severity thresholds of the expedited severity metric	74
Figure 49: Breakdown of total calculation time for the expedited severity metric.	75
Figure 50: Breakdown of total user intervention time for the expedited severity metric.....	75
Figure 51: Breakdown of total non-user calculation time for the expedited severity metric.....	77
Figure 52: Initial results for the inter/intra user variation between user segmentations.	80
Figure 53: Differences in image cropping for User D's 1st and 2nd runs (1st Run - Left, 2nd Run - Right).	81
Figure 54: Effect of re-run for User D on segmentation results for Case I.	82
Figure 55: Differences in the articular slice between users for Case IV.	83
Figure 56: Differences in components and overall fracture severity values between users in the inter-/intra-user variability test.....	84
Figure 57: Variation in severity stratification for combined severity scores between users in the inter-/intra-user variability test.....	85

LIST OF EQUATIONS

Equation 1:	30
Equation 2:	30
Equation 3:	31
Equation 4:	46
Equation 5:	46
Equation 6:	47
Equation 7:	47
Equation 8:	47
Equation 9:	47
Equation 10:	47
Equation 11:	48
Equation 12:	48
Equation 13:	80

PREFACE

The development and refinement of an expedited fracture severity assessment methodology described in this thesis is part of a long line of research. It would not have advance to its present level without the prior dedicated work of Drs. Christina Beardsley and Thad Thomas. Dr. Beardsley's time spent at the University of Iowa working on the fracture mechanics of bone laid the groundwork for the development of a severity metric. Her research on the fracture energy release rate of bone and other surrogate materials, along with her investigation into the use of clinical CT scans as an avenue to measure the fracture energy, were crucial in the development of the full severity metric. When Dr. Beardsley left, Dr. Thomas stepped in to further develop the fracture severity analysis methodology toward clinical application, to the starting point for the present work. His time and effort developing the principles and components in the objective fracture severity assessment were instrumental in laying the groundwork for the present work. Thad's additional doctoral studies in developing a virtual pre-operative reconstruction planning platform provided key components for the expedited severity metric, such as the 3D watershed segmentation method used. Without these individuals' prior efforts, along with others in the lab who contributed to the development and implementation of a fracture severity metric, the work presented here would not have been possible.

CHAPTER ONE: INTRODUCTION

Post-traumatic osteoarthritis (PTOA) is a debilitating disorder resulting from trauma to an articulating joint. The condition imposes a significant physical and emotional burden on an individual, with substantial financial implications, as well. The severity of the joint trauma has been shown to correlate highly with the risk of subsequent PTOA development, so treating surgeons have adopted fracture severity assessment methods to aid in their treatment decision-making. However, current systems for classifying the severity of the trauma are highly subjective and have poor reproducibility. This makes it difficult to differentiate PTOA development attributable to the initial injury from that potentially influenced by the chosen treatment. The most common situation in which this problem arises is for an articular fracture, treatment of which involves decisions related to trying to restore the fragmented articular surface.

To address these limitations in assessing fracture severity, a CT-based severity metric was previously developed, with the goal of providing an objective, quantifiable measure of initial injury severity. Utilizing fracture mechanics theory, the CT-based severity metric used measures of interfragmentary surface area to infer the amount of energy absorbed during fracture, the amount of comminution in the resulting fracture, and the level of dispersion and displacement of the fracture fragments. Combining these components into a single overall severity score produced a reliable metric for objective assessment of fracture severity. However, this assessment approach did present some practical limitations, which precluded its use in routine clinical care. The greatest limitation was the time required to obtain a severity score. At roughly 8 hours, it was too much time before a surgeon could get a score to assist in treatment planning. Another major challenge in using the severity metric was that its acquisition depended upon the contralateral intact limb being included in the CT scan, for taring purposes. Even though using the intact contralateral would be ideal, obtaining this limb in the CT scan for each

patient would be a difficult challenge impeding the implementation of the expedited metric in the routine clinical setting.

To address these limitations, an expedited approach for severity assessment has been developed. The expedited approach builds upon the prior fracture mechanics methods, but it utilizes a textural image analysis of CT images from the fractured bone, in lieu of measurement of interfragmentary surface area. The focus of this thesis is the implementation and development of an expedited fracture severity metric that can be used clinically. Such a metric would aid in showing the relative benefits of certain surgical treatments as well as in guiding the surgeon in developing a treatment plan for their patients.

CHAPTER TWO: LITERATURE REVIEW

The Ankle

A fully developed fracture severity metric has the potential to be used on any fracture to an articular surface. Articular fractures are susceptible to the development of post-traumatic osteoarthritis and could benefit from an objective severity metric. The tibial plafond was the joint chosen to be the platform for which the fracture severity metric would be developed. The ankle has a low occurrence of primary osteoarthritis development, which made it an ideal location for severity metric development.

Major Anatomical Structures

The ankle joint is the articulation between the leg and the foot. It is the confluence of three bones, forming two related joints (Figure 1). The tibia, fibula, and talus (the superior-most bone of the foot) form the main articulation, which acts to a first approximation as a hinge joint, with its axis predominantly along a medial-lateral direction. It is generally termed the tibiotalar joint, in recognition of the primary role of the articulation between the tibia and the talus. The distal-most extension of the tibia (the medial malleolus) acts as a medial buttress to the talus. The distal-most portion of the fibula provides lateral support, preventing lateral translation of the talus [1]. The distal articular surface of the tibia, which serves as the primary superior articulating surface of the joint, is called the tibial plafond. The term plafond is a combination of the Middle French terms “plat” meaning “flat” and “fond” meaning “bottom.” In English, plafond is described as an elaborate ceiling [2]. This surface has a slight concavity to it that closely matches the convexity of the superior talar dome, which in turn acts as the reciprocating articular surface to the tibial plafond. This relationship between the talar dome and the tibial plafond serves to provide additional stability to the joint. Additional stability for this joint is provided by the inferior tibiofibular joint (syndesmosis), which is surrounded by four major ligamentous structures that resist separation of the fibula and the tibia.

When looked at as a whole, the ankle resembles the structure seen in a mortise and tenon joint, providing a highly stable articulation (Figure 1) [1].

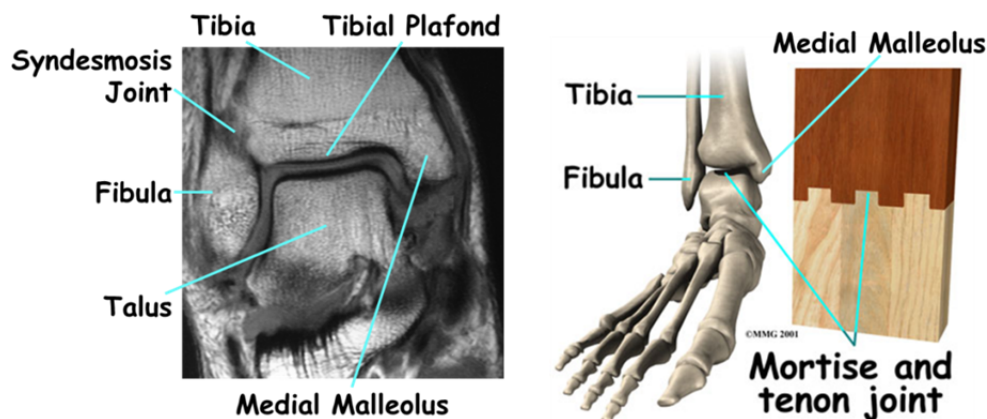


Figure 1: The ankle joint structures and major landmarks.[3]

Tibial Plafond Fractures

Fractures of the tibial plafond, also known as tibial pilon fractures, constitute roughly 7% of tibial fractures. These fractures typically result from an abrupt axial compressive force which drives the talus into the tibia (Figure 2) [4]. Some degree of shearing and bending of the bone are also seen in these fractures, but axial compression is generally the primary cause of fracture [5]. These fractures are usually associated with higher-energy injuries resulting from a fall from a height, a motor-vehicle accident, or any other injury resulting from a vertical loading [2]. In contrast, injuries seen in skiing or other sporting events are typically low-energy fractures, resulting from primarily torsional loading. These low-energy fractures typically produce a spiral fracture, with a lower amount of bone fragmentation [6, 7].



Compressive Force

Figure 2: Large compressive forces delivered to the tibia through the talus can result in complex fractures of the tibial plafond.[8]

Fracture Characteristics

Fractures of the tibial plafond are among the most complex injuries of the lower limb [9], causing a spectrum of damage to the bones and the surrounding tissues. When reviewing a fracture, certain characteristics are identified to assess the severity and to plan treatment. While many characteristics of the fracture are analyzed (subluxation, anatomical orientation at the time of injury, etc.), four main characteristics are emphasized in prognostication of outcomes. These include the degree of fracture comminution (fragmentation), the amount of comminution involving the articular surface, overall fragment displacement and dispersion, and surrounding soft tissue damage [2, 10, 11].

A comminuted fracture is one in which the bone is broken into a number of smaller pieces (Figure 3). The amount of comminution in an articular fracture is directly related to the amount of energy imparted to the bone [12]. Low-energy injuries generally produce spiral fractures with large fragments of bone, while high-energy injuries result in fractures with multiple bone fragments. While comminution at any site in the bone is a concern, comminution of the articulating surface has a greater influence on the difficulty

of the surgical reduction of fragment displacements, as well as on the long-term health of the joint, especially when considering post-traumatic osteoarthritis [13].

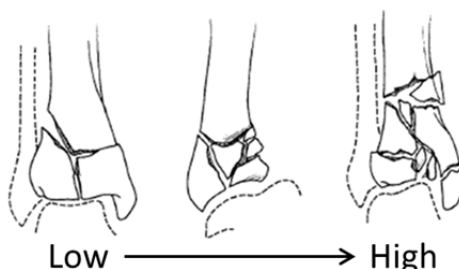


Figure 3: Variation in comminution for fractures of the tibial plafond.

© 1994 American Academy of Orthopaedic Surgeons. Reprinted from the *Journal of the American Academy of Orthopaedic Surgeons*, Volume 2 (6), pp. 297-305 with permission.

When a fracture of the tibial plafond occurs, bone fragments are often displaced from their intact state. Many times, the fragments will move radially away from each other in the transverse plane, which is referred to as dispersion. Additionally, depending on the type of fracture, a fragment, or fragments, will be displaced proximally or distally. Similar to fracture comminution, fragment dispersion and displacement are related to the energy of the fracture. Compression fractures, whose energy values are often in the higher ranges, typically result in higher comminution associated with moderate to high levels of dispersion and/or displacement. Lower energy fractures, which typically are a result of rotational or torsional loads, involve large bone fragments with minimal to no fragment displacement, especially at the articular surface [10].

The surrounding soft tissue can be greatly affected by a tibial plafond fracture, and this is especially important in the distal leg because of the relatively sparse quantity of soft tissues. Injuries to the muscle, skin, cartilage, and other soft tissue structures vary depending on the severity of the fracture. A number of issues, including swelling,

fracture blisters, infection, articular cartilage damage, wound breakdown, and vascular issues all can cause complications in treatment along with long term health issues with the joint. High energy injuries are commonly associated with open fractures, where the soft tissues are stripped from the bone, blood vessels are lacerated or severed, and significant damage to the articular cartilage can be seen [10, 14]. While damage to the bone and soft tissue of the joint during the injury is important in determining the overall health of the joint, treatment and surgical methods can be equally as important.

Post-traumatic Osteoarthritis (PTOA)

Treatment and Surgical Decision-Making

After a fracture of the tibial plafond, the treatment chosen can have a considerable effect on the short and long term health of the joint. Prior to repairing the joint, surgeons often attempt to classify the severity of the fracture. Classification systems by Rüedi and Allgöwer use articular and metaphyseal displacement and comminution to separate fractures into different categories [15]. Over time, these systems along with other past systems such as Böhler[16] and Gay and Evard[17], have evolved into some of the more widely used current classification schemes. The AO/OTA fracture classification system provides the most comprehensive and detailed approach today [2] (Figure 4). However, classification systems are inherently subjective, observer-based techniques comprised by low interobserver reliability [18-20]. While classification systems are currently the best available, a more objective basis needs to be developed.

Many different treatment methods have been used for reconstructing fractures of the tibial plafond. These methods include nonsurgical care, open reduction and internal fixation, external fixation with or without limited internal fixation, and primary arthrodesis [2, 21-23]. Correctly classifying the fracture to an appropriate category can help the surgeon to narrow the options for which treatment method to choose. It is important to note that because of the poor reproducibility of categorical fracture

classification, literature supporting which methods produce the most optimal results for certain classifications is lacking, and no definitive conclusions can be drawn on one method over another [2].

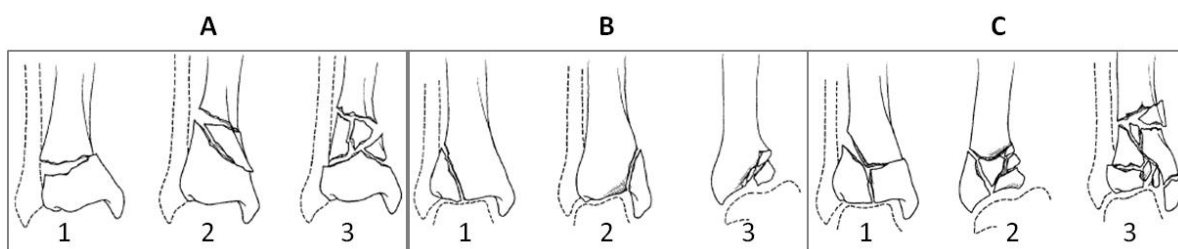


Figure 4: AO/OTA fracture classification system.

© 1994 American Academy of Orthopaedic Surgeons. Reprinted from the *Journal of the American Academy of Orthopaedic Surgeons*, Volume 2 (6), pp. 297-305 with permission.

Once the physician decides to surgically reconstruct the fracture, there are two primary goals. The first is to restore the articular anatomy; the second consideration is to provide conditions for optimal healing of the injured soft tissues [24]. With these goals in mind, immediate surgery is often not pursued. Allowing for the soft tissues to recover from the initial trauma so that they can endure the additional trauma of surgery is often essential to a successful outcome. Depending on the complexity of the fracture, often times a computed tomography (CT) scan will be taken of the fractured ankle to assist in creating a plan for surgery [14, 25].

Development of Post-Traumatic Osteoarthritis

After the surgery is completed, a number of complications may arise from the surgery and/or the injury. These include wound problems, infections, malunions, nonunions, arthrodesis, and post-traumatic osteoarthritis (OA). The main focus of the

work described in this thesis was post-traumatic OA, and the ability to predict its development.

Post-traumatic OA is the development of osteoarthritis resulting from an injury or traumatic event to the joint. This trauma may entail tears of the meniscus (in the knee), ligaments, or capsule, along with joint dislocation. A common final outcome is eventual degeneration of the articular cartilage. The development of post-traumatic OA can occur directly from the initial trauma or secondary to enduring irregularities of the joint after treatment [26, 27]. Post-traumatic OA of the tibial plafond will typically present within the first one to two years after the injury [10].

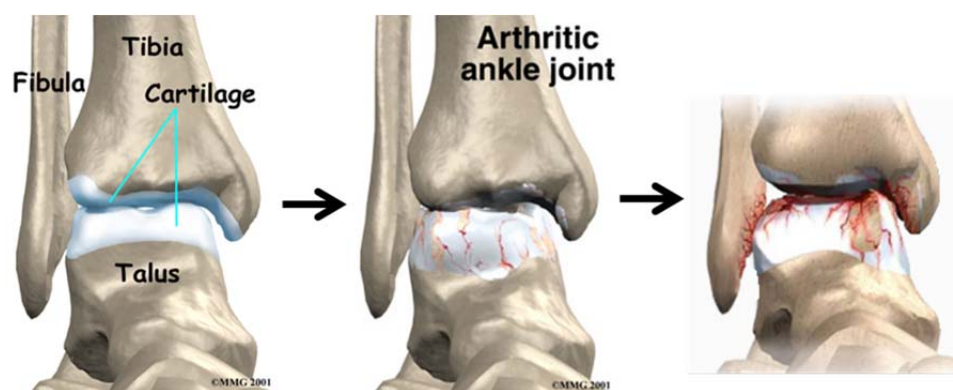


Figure 5: Degeneration of articular cartilage resulting in post-traumatic OA [28-30].

Post-traumatic OA development can begin shortly after the injury to the joint. Before other apparent signs of cartilage deterioration, changes in the physiology and organization of proteoglycans can occur [31]. This change in the proteoglycans can lead to a reduction in the stiffness, as well as to greater permeability of the cartilage. As a result, loading of the collagen network and associated structures of the cartilage will increase, which can then lead to further damage to the cartilage. In addition to the effect on proteoglycans, injury may also cause deformations of the collagen extracellular

matrix, disturbances between the collagen fibril and proteoglycan relationship, and swelling of the cartilage matrix [32].

Most of the discussion has been focused on post-traumatic OA developing from the initial trauma to the joint. As mentioned above, cartilage degeneration can additionally result from joint irregularities. Perfect reconstruction of the articular joint in surgery is extremely difficult, and oftentimes impossible to achieve. As a result, incongruities of the articular surface may present. These incongruities can lead to increases in contact stress at certain locations of the articular surface. If the increases in contact stress are great enough, localized damage to the matrix of the cartilage can occur [33]. Over time this damage could lead to chondrocyte apoptosis and resulting degradation of the cartilage [34]. The degraded cartilage could then cause new incongruities of the articular surface, leading to further degeneration and eventual post-traumatic OA development [35].

Post-traumatic OA is a form of secondary OA, meaning that it develops from a specific cause (articular fracture, chondral injury, or ligament or meniscal injury). This is different from primary OA, which is an idiopathic development. While the end-stage pathology of each form of OA (primary vs. secondary) is similar, distinction between the two is important. Approximately 12% of patients presenting with symptomatic OA are suffering from post-traumatic OA of the lower extremities, i.e. the hip, knee, and ankle. The direct financial burden resulting from patients with post-traumatic OA is roughly \$3.06 billion per year. Additionally, the age of patients with post-traumatic OA is comparatively younger than patients with OA as a whole.

Focusing more specifically on post-traumatic OA development of the tibial plafond, the average age of patients exhibiting post-traumatic OA in the ankle is roughly 14 years younger than those for primary ankle OA. Additionally, 79.5% of patients presenting with symptomatic OA of the ankle develop post-traumatic OA. This is substantially higher than the 1.6% and 9.8% prevalence in the hip and knee, respectively,

making the ankle an ideal joint in which to perform research involving post-traumatic OA [26]. The percentage of people who develop severe post-traumatic OA after a fracture of the tibia plafond can also be high. In one study, looking at patients 5-12 years after injury, the prevalence of severe post-traumatic OA was as high as 74% [36]. There is also evidence that the number of fractures of the tibial plafond is on the rise. One of the common sources of trauma in fractures of the tibial plafond is motor vehicle accidents. With the development of better safety measures, air bags for instance, patients are more likely to survive an accident in which lower extremity trauma resulting in tibial plafond fractures occurs [37, 38].

Post-traumatic OA Classification

While excellent outcomes of a fractured articular joint are possible through optimal reduction, fixation, and rehabilitation, the quality of the reconstruction has been shown to have only a relatively weak association with the development of post-traumatic OA [10, 35]. If the quality of the reconstruction cannot always predict post-traumatic OA development [39-41], by implication there must be other causes that predispose the joint to post-traumatic OA. Many believe that the best predictor of the development and severity of post-traumatic OA is the energy transmitted through the joint in the insulting trauma itself [5, 6, 42-44].

As noted above, multiple systems exist to classify fractures of the tibial plafond. The most commonly accepted system is the AO/OTA classification. While other systems also exist, most of them do not sufficiently stratify the fractures. Inability to appropriately classify the severity of the fracture can lead to errors in treatment, and to prognosis uncertainty [2]. Another common issue with classification systems is that they involve subjective evaluations, depending heavily on a surgeon's experience and opinion [10]. This makes it difficult to evaluate surgical methods of reconstruction if there exists significant interobserver and intraobserver variability within the literature [2, 42].

In addition to pre-operative severity classification systems, multiple systems also exist to gauge the severity and effect of post-traumatic OA on the patient. The Iowa Ankle Score utilizes a patient's self-assessment of pain and function, in addition to physical assessment of the range of motion, gait, and deformity [45]. The results are then categorized on a 100-point scale. The Short Form-36 (SF-36) is an additional system often used to estimate the effects of PTOA. The SF-36 is a questionnaire given to the patient which focuses on the patient's health-related quality of life, by evaluating how the fracture affected their physical and emotional health. While these systems are widely used, they have been shown to have weak correlations with the presence of post-traumatic OA [36].

One system that is widely accepted for assessing the degree of OA development is the Kellgren-Lawrence (KL) score [46]. This score is obtained by examining a radiograph of the joint. Criteria considered in determining the score are the development of osteophytes, narrowing of the joint space, development of sclerosis, and deformities in bone contour. After analyzing the radiograph for each of these issues, a score is then given ranging from 0 to 4, where 0 represents no signs of OA development and 4 represents severe OA. Table 1 further illustrates the criteria for each KL score. Additionally, radiographic examples of each KL score are shown in Figure 6 [47]. A joint with a KL score of 0 or 1 is often considered to not be arthritic, while scores of 2 or higher indicate mild to severe radiographic OA. While this score is widely accepted, it is still the result of a subjective analysis, which leads it to have some inconsistencies.

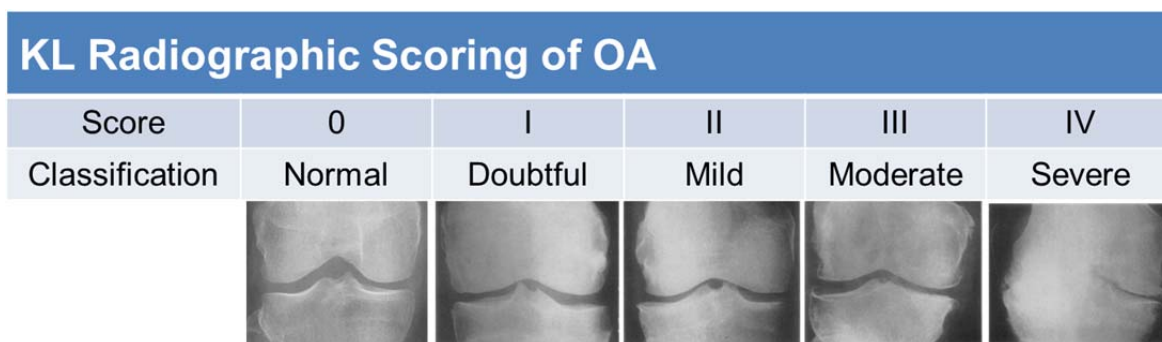


Figure 6: Example radiographs of differing KL scores in the knee. [47]

Table 1: KL score characteristics and delineation.

KL Score	Characteristics
0	· No signs of OA development
1	· Doubtful narrowing of joint space · Possible osteophytic lipping
2	· Definite osteophytes · Definite narrowing of joint space
3	· Moderate multiple osteophytes · Definite narrowing of joint space · Some sclerosis · Possible deformity of bone contour
4	· Large osteophytes · Marked narrowing of joint space · Severe sclerosis · Definite deformity of bone contour

Despite all of these fracture classification systems, there has existed no objective way to reproducibly measure the severity of the fracture. While the quality of the reduction of the articular surface is believed to influence the health of the joint, there is currently no way to demonstrate this point. One of the biggest challenges for research aimed at showing the effects of articular reduction quality upon outcomes is separating the effects of the initial trauma from those of incongruous reduction. Without the ability

to make this distinction, it is impossible to draw any conclusions on the effects of surgical reconstruction and anatomic reduction. To address this issue, an objective tool is needed that is capable of reliably and quickly measuring the amount of energy absorbed by the articular surface and determining the initial damage to the joint [35].

Computed Tomography (CT)

Fractures of the tibial plafond are frequently quite complex. A CT scan is often taken to assist in surgical planning, due to its superiority to plain film x-ray in visualizing bone fragments and their three dimensional displacements [25]. It is for this reason that CT scans are an ideal resource for developing a fracture severity metric. CT scans utilize the principle of x-ray attenuation to develop a 3D array of intensity values, called Hounsfield Units (HU). The HU values are indicative of the density of a given structure, with the convention that water has an HU value of 0, and air a value of -1000. Soft tissue intensities on CT range from -100 to 100 HU, cortical bone can range from 500 to 2000+ HU (averaging around 1000 HU), and metal will typically exhibit roughly 3000 HU [48, 49].

For present purposes, image properties of CT scans are important to understand, as they play a key role in the development of the expedited severity metric that lies at the heart of this thesis. The first property of importance is the pixel size of the CT image. In-plane pixel size of the image can vary greatly, depending on the CT scanner and the size of the field of view used in acquisition. In the cases studied, in-plane pixel sizes ranged from 0.243 mm to 0.782 mm. Differences in pixel sizing can cause significant variations in the quality and texture of the resulting images [50].

The second noteworthy property of the CT image is the convolution kernel used to reconstruct the image. CT images are generated by gathering x-ray beams on a detector. The data from the detectors are a 1D representation of the 2D cross section through which the x-ray is transmitted (Figure 7). Data are collected at the detectors at

multiple angles through the cross section. In order to reconstruct a 2D representation of the cross section, a convolution kernel is applied to the detector data [49].

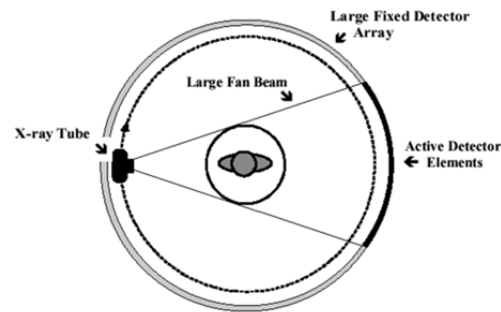


Figure 7: X-rays being transmitted through a 2D area and collected on a 1D detector. The convolution kernel chosen to reconstruct the 2D area can influence the resulting texture of the image.

Multiple convolution kernels exist, having different purposes for the final image. Some kernels make it easier to distinguish bone structures and edges. While such kernels can make it easier to see bone edges, they typically are more susceptible to pixel noise and thus can appear grainy. Conversely, other kernels exist that will blend structures together. With such kernels, bone edges are not as definitive, but the images are typically smoother and improve the ability to detect objects that have low contrast against the background, for instance soft tissue structures [51]. Because of the different goals of different convolution kernels, images of differing textures can result from the same CT scan acquisition (Figure 8). These differing textures play a significant role in the expedited severity metric development.

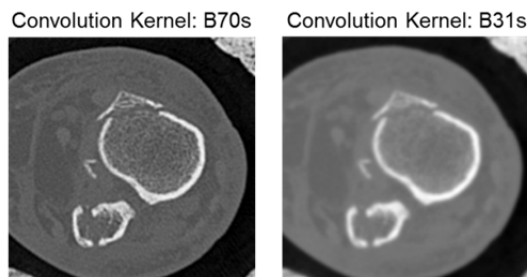


Figure 8: Image texture differences between convolution kernels for the same image.

The final property to discuss also relates to the appearance of the image. Many times a spanning external fixator is applied to the ankle joint before the pre-operative CT scan is obtained, in order to restore the length and alignment of the fractured limb. This external fixator is made of metal and is necessarily included in the resulting scan. The metal can cause scattering of the x-rays, thereby disturbing the image (referred to here as metal artifact – Figure 9). The scattering produces artifacts in the HU values that are obtained. These altered HU values present a substantial challenge to obtaining an expedited severity metric due to the resulting changes in the image texture, which is the basis of the expedited severity metric development.

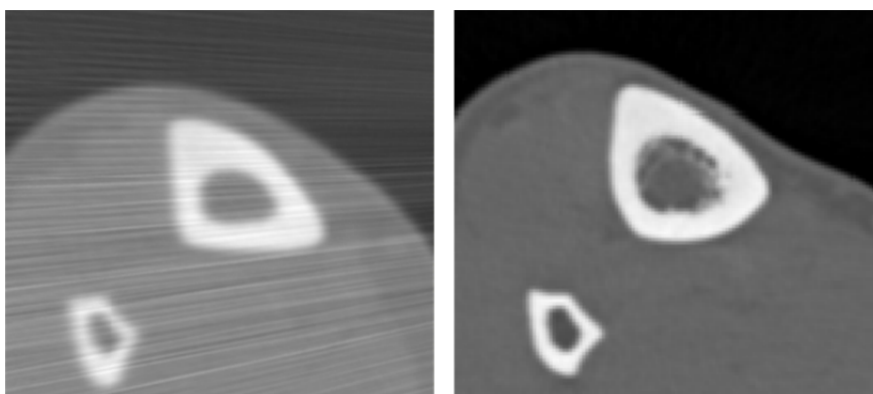


Figure 9: The effects of metal artifact on CT image quality and texture.

Full Fracture Severity Metric

Basis of Calculation

The present thesis aims to provide an expedited method to quantify fracture severity from CT scan data. Since it builds upon prior work in this area[46, 52, 53], the following discussion provides a brief synopsis of that earlier work. The fracture severity metric that was previously developed was based upon the fracture energy imparted to the tibia by trauma to the ankle joint. In the case of tibial plafond fractures, in particular, the fracture energy is almost exclusively delivered to the tibia directly through the tibio-talar articular cartilage. For this reason, the tibial plafond fracture was chosen for development of a fracture severity metric. This initial metric was focused on the energy absorbed by the tibia, ignoring the fibula, since the fracturing of the fibula requires significantly less energy than the tibia, and some of that energy circumvents the tibio-talar articular surface.

The prior fracture severity metric was based primarily on a specific property of the fracture mechanics of bone. Brittle solids, such as bone, will absorb mechanical energy by fracturing, creating new surface area. The amount of liberated surface area is proportional to the amount of energy absorbed [54]. The previous severity metric relied upon deduction of the fracture surface area from a CT scan of the patient's fractured limb. A CT scan of the contralateral limb was additionally obtained, and it was used for taring purposes in the severity calculation. In order to determine the changes in the fractured limb, it would be necessary to know how the fractured limb differs from the limb prior to the fracture. The intact contralateral limb served as a surrogate for the pre-traumatic fractured limb. The tibia was then segmented from the surrounding bone and soft tissue, using a semi-automated process. This process entailed initially running the CT images through an automated program which proposed possible edges of the tibia bone. After candidate bone edges were established, the user went through the CT images

slice by slice adding, editing, or deleting the edges until a satisfactory segmentation of the bone was obtained. From the segmentation, the perimeters of the fractured and contralateral intact bone could be calculated. Coupling the segmentation with the in-plane pixel size and slice thickness of the CT image, the surface area of each bone in each slice could be deduced. Summing these values over the length of each limb would then give the total surface area of the fractured tibia and its intact counterpart [55]. It is from these surface areas that the energy of the trauma was calculated.

The surface areas would then be coupled with scaling factors to account for the bone density and age of the patient. Since the density of a brittle material can determine the amount of energy absorbed over a given liberated surface, determining density of each patient's bone is crucial to determining the amount of energy that was absorbed in the injury [56]. A bone density scaling factor was determined by calculating the median HU intensity of all the segmented bone in the proximal intact tibia. Because the strength of bone decreases monotonically with age, an additional scaling factor was calculated accounting for the age of the patient. These scaling factors were utilized with the fragment surface areas to determine the energy of the trauma [52].

Additional Fracture Severity Components

The full fracture severity metric incorporated assessment of three different components of the fracture deemed to contribute to the development of post-traumatic OA. In the development of the expedited metric, it was attempted to account for these three components. The first component is one which has been shown to have a direct relationship with outcome: fracture energy. This component compares the surface area of the fractured limb to that of the intact limb. The difference between the surface areas provides the interfragmentary surface area, or the area liberated from the absorbed energy of the injury (Figure 10). This interfragmentary surface area is then combined with the scaling factor accounting for bone density and age, noted as the energy release rate, to

determine the overall energy absorbed by the tibia during the trauma, i.e., the fracture energy.

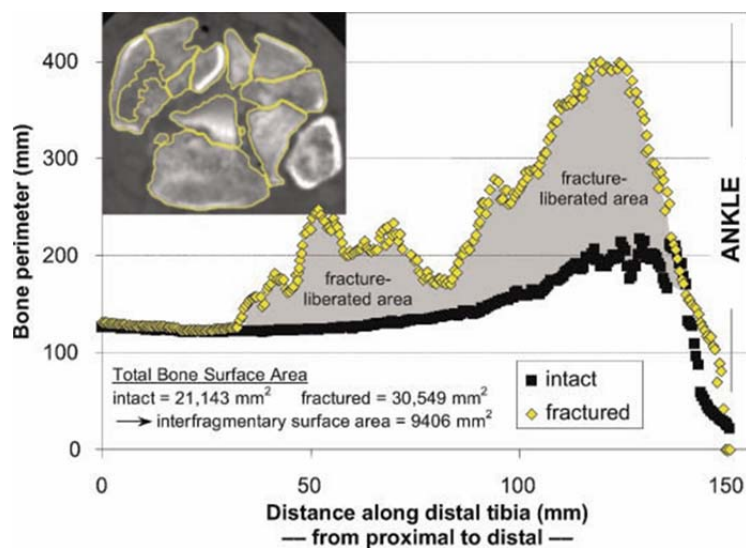


Figure 10: Interfragmentary surface area calculation for a fractured tibia [52].

The second component used to describe fracture severity is the amount of articular comminution. This component captures the disturbance that occurred at the articular surface. Since this is the location where cartilage degeneration occurs, accessing the damage to this area is especially important. To quantify articular comminution, first the articular region of the bone needs to be identified. This was done by analyzing CT slices within 1.5 mm proximally and distally (3 mm total) from the articular surface. The percent difference between the fractured surface area and the contralateral intact surface was determined over this region. The resulting percentage was then compared amongst the patients to determine the level of disruption [46].

The third and final assessed component of fracture severity is fragment dispersion and displacement. This component involved an analysis supplemental to those stemming from fracture mechanics of bone. The first part in the computation of this component is

to align the proximal base of the fractured tibia to the corresponding position of the mirrored contralateral intact. A convex hull was generated for each limb. A convex hull is the smallest convex polygon circumscribing an object. The volume of the intact limb was calculated and subtracted from the aggregate volume of the mirrored intact/fractured limb, to determine the fragment dispersion and displacement (Figure 11) [52].

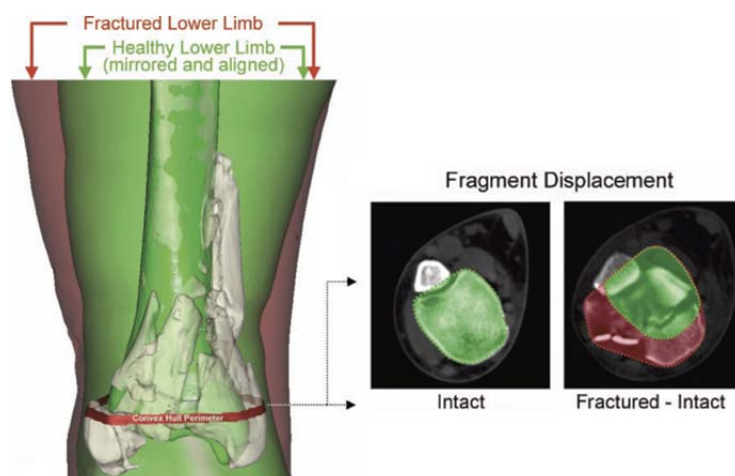


Figure 11: Calculation of fragment dispersion/displacement [52].

Since each of these components were parts contributing to the overall fracture severity of the limb, combining these together into one metric was the next step. Before this could be done, each metric was normalized to a range from 0 to 100, where 0 is the least severe case and 100 is the most severe case. This was necessary because the different components of fracture severity possessed different units of measure. A multivariate linear regression was then carried out using each of these components as the independent variables, and the KL scores of each patient obtained at a two year follow-up exam as the dependent variables.

Results and Limitations

The above fracture severity metric was used to analyze 20 different fractures. (While the expedited severity metric would subsequently be used to analyze more than just these 20 fractures, its severity values and results were often compared to those of the full metric for these 20 patients.) These patients consisted of 13 males and 7 females, ranging in age from 20-64. These cases were selected from a larger group treated at the University of Iowa Hospitals and Clinics by an experienced orthopaedic surgeon, to represent an appropriate range and distribution of fracture severities. Patients returned for a follow-up exam approximately 2 years after the injury, and a KL score was assigned based upon a weightbearing radiograph taken at that time. In order to be eligible for analysis, the patient had to have suffered an isolated closed or open unilateral fracture. Additionally, in order for the severity metric to be obtained, pre-operative CT scans needed to be available for both the fractured and intact contralateral limb.

Due to the discrete nature of the KL score, the statistical measure chosen for comparing the severity scores to the KL score was concordance. The concordance represented the probability that a severity variable would correctly differentiate the arthrosis (KL) scores of a given pair of cases. The concordance value ranges from 0 to 1, with 0.5 representing a chance agreement and 1 representing a perfect agreement.

Concordance values were calculated for each of the components of the severity metric, in addition to the combined metric. The fracture energy component ranged from 5.2 to 27.2 Joules. The concordance between fracture energy and the KL score was roughly 81%. Articular comminution percentages ranged from 51% to 156% and had roughly a 78% concordance with the KL score. Fragment dispersion/displacement values ranged from 3.8 to 48.5 cm³ with approximately 79% concordance with KL scores.

At the 2 year follow-up exam, 11 of the 20 patients had developed some level of post-traumatic OA (a KL score of 2 or greater). The severity values for these cases were additionally compared to those that did not develop PTOA (KL score of 0 or 1). A two-

sample independent t test was run between these two groups, with resulting p values of 0.003, 0.031, and 0.007 for fracture energy, articular comminution, and dispersion/displacement respectively.

A regression analysis run to determine the optimal contribution of each component in the combined metric determined that the fragment dispersion/displacement component did not significantly contribute to improve the model's predictive ability. The component was therefore excluded from the combined metric. The final combined metric consisted of a 48% weighting of fracture energy and a 52% weighting of articular comminution. This combined metric was able to strongly predict the PTOA as an outcome, with an 88% concordance to the KL score. Additionally, the combined score for cases that developed PTOA was statistically significantly different from the combined scores of cases that did not develop PTOA.

The Rationale for an Expedited Fracture Severity Metric

The full fracture severity metric was shown to be an excellent predictor for development of post-traumatic OA, but it suffers from several limitations. Ideally, this metric would be implemented in a clinical setting to help the surgeon in the treatment of the joint. For example, if the severity score is significantly high and well above a PTOA severity threshold, surgical treatment might undertake a salvage procedure such as joint fusion. On the other hand, if the score is near the threshold, the surgeon might focus the treatment on the quality of the articular reduction, to reduce the possibility of deleterious contact stresses.

One of the biggest limitations for this initial severity metric is its cumbersome nature for clinical application. This is primarily due to the time required to obtain a severity score. Because of the time required to meticulously segment the bone in each CT image, the average time to calculate a severity score was roughly 8 to 10 hours per case [46]. For a severity metric requiring such a large amount of time to obtain, a clinical

application is extremely unrealistic. If the severity metric is ever to be applied clinically, the time required to obtain a severity score must be significantly reduced. Also, the full fracture severity metric required the use of the intact contralateral limb for taring purposes. This requirement significantly limits the number of cases capable of being analyzed, as the intact limb is not standardly obtained in the CT scans. This dependency on the intact contralateral limb, coupled with the extended time needed to obtain the full fracture severity metric underscored the need for an expedited severity metric. With this expedited metric, an objective classification system for fracture severity could be developed for clinical application.

CHAPTER THREE: METHODS

The theory behind the expedited metric was initially conceived as a secondary development of the full severity metric, prior to the undertaking of this thesis research. Work in this thesis involved taking the theory behind the expedited metric, along with some preliminary analyses, and developing it to be capable of handling any CT image of a fractured tibial plafond. The work presented will include refining the expedited analysis to optimally analyze the CT images, and enhancing the segmentation process to allow for minimal user intervention. Secondary work involved developing a method of registration for the fractured tibia to its intact counterpart. The registration landmark chosen was the articular slice. How this slice is automatically extracted from the CT image, along with locating the proximal-most slice of the image containing a fractured fragment, is additionally discussed.

Significant progress was also made in the development of a surrogate representation of the intact limb. Through the use of edge-preserving image filters, along with scaling factors accounting for the differences in CT image and patient-specific factors, an intact surrogate model was developed. This surrogate would replace the intact contralateral limb for taring purposes for the metric. Incorporating these advances represents an important contribution to enhancing the clinical applicability of the final expedited severity metric.

The development of surrogate components for fracture energy, articular comminution, and dispersion/displacement of fragments was also accomplished in the work here reported. Just as for the full metric, each component was then combined to produce an overall severity score for each case. Optimizing the weighting factors in the combined score would be the final piece of development for the expedited metric. The resulting overall scores would then be an objective measure of fracture severity, calculable in an expedited time frame.

Gray Level Co-occurrence Matrix (GLCM)

Description and Input Parameters

The concept behind the development of this expedited fracture severity metric was that a textural analysis of a CT dataset would provide a suitable surrogate for the differences in surface area central to the previous fracture severity metric. In essence, a textural measure was sought that could capture the disruption in the spatial distribution of CT intensities associated with an intact bone becoming a fractured bone. Toward this end, a textural analysis methodology was developed using existing gray level co-occurrence matrix (GLCM) functions in MATLAB.

The initial step in the GLCM analysis portion of the expedited metric is rescaling of the image intensities to a specified number of integer levels (Figure 12). This specified number of levels determines the resulting size of the GLCM. For example, rescaling an image to 10 integer levels will result in a 10 by 10 matrix filled with zeros (Figure 13). In the expedited metric, it was important to choose a value for the number of levels that is small enough to allow for an efficient analysis but not too small such that significant distinctions are not differentiated. The number of levels chosen for the expedited severity metric was 10. This value differentiated bone structures, while still affording a swift analysis of the image. After the number of values had been decided, the image is then rescaled using a linear scaling method to obtain the image for the GLCM analysis. For example, in Figure 12 below, the initial image is rescaled to integer values ranging from 1 to 10.

Once the image is rescaled and the GLCM is defined, the textural analysis of the image begins. The GLCM approach compares intensity values of each pixel in an image to the intensity values of specified neighboring pixels and constructs a matrix that counts the frequency of occurrence of given neighboring intensity pairings. For instance, say the analysis were to look at the neighboring pixel to the right of each pixel analyzed. In the

image included in Figure 12, the pixel in the 1st row and 1st column (1, 1), which has a rescaled intensity of 1, would be compared to the pixel in the 1st row and 2nd column (1, 2), a rescaled intensity value of 4. The relationship between the intensities then determines the position within the GLCM (row 1, column 4) to be incremented by one (Figure 13). This analysis proceeds pixel-by-pixel through the original image matrix until each pixel of the image has been analyzed.

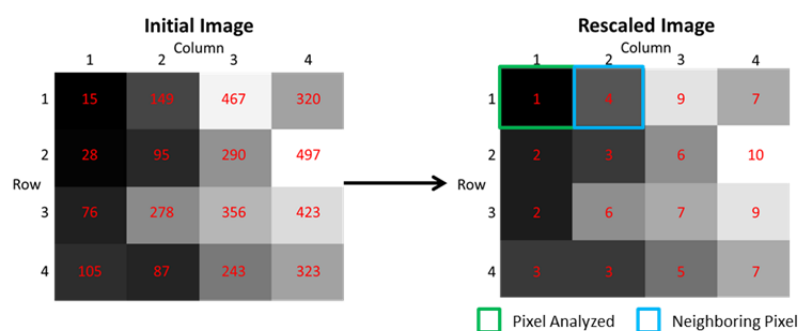


Figure 12: GLCM image analysis example showing the results of the linear scaling method used on images.

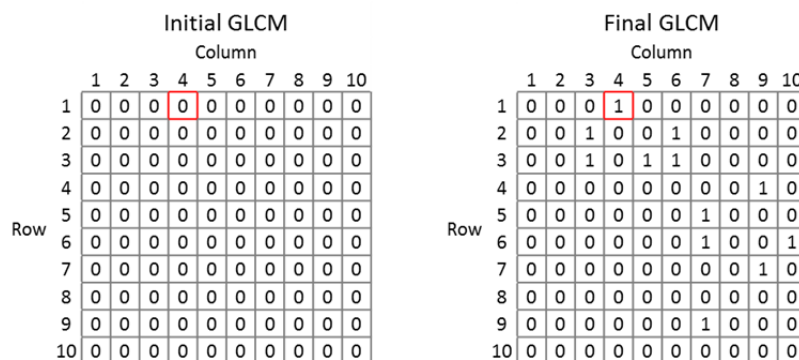


Figure 13: GLCM before and after a GLCM analysis was run on the rescaled image of Figure 12.

One area of concern with this analysis comes when a pixel is located on the edge of the image. If the pixel being analyzed is located on the edge of the image and it is trying to analyze a neighboring pixel which is nonexistent due to being outside the dimensions of the image, the analysis will ignore these instances and continue on in the process. For example, assume the previous setup where the neighboring pixel is the pixel to the right of the one analyzed. For any of the pixels located in the 4th column, their resulting neighboring pixel would be in the nonexistent 5th column, so the analysis ignores that comparison and moves on to the next pixel in the image.

When performing this analysis, the function requires 4 different input arguments: gray limits, number of levels, symmetry, and offset. The gray limits argument sets the minimum and maximum intensities for the rescaling process. The number of levels argument tells the function how many integer levels the image must be rescaled to, and thus dictates the size of the GLCM. Anything below the minimum value will be set to 1 and anything above the maximum value will be set to the maximum integer value. The offset argument sets the direction and distance of the neighboring pixel to be analyzed. Multiple offsets can be chosen for a single analysis. Finally, if the symmetry option is chosen, the function will not only increase the count for the GLCM position specified through the intensity relationship, but will also increase the count of the corresponding cross-diagonal position. For example, in the previous analysis, in addition to increasing the count at the matrix position (1, 3), it will also increase the count at position (3, 1).

Non-symmetric GLCM		Symmetric GLCM	
Column		Column	
	1 2 3 4 5 6 7 8 9 10		1 2 3 4 5 6 7 8 9 10
1	0 0 0 1 0 0 0 0 0 0	1	0 0 0 1 0 0 0 0 0 0
2	0 0 1 0 0 1 0 0 0 0	2	0 0 1 0 0 1 0 0 0 0
3	0 0 1 0 1 1 0 0 0 0	3	0 1 2 0 1 1 0 0 0 0
4	0 0 0 0 0 0 0 0 1 0	4	1 0 0 0 0 0 0 0 1 0
5	0 0 0 0 0 0 1 0 0 0	5	0 0 1 0 0 0 1 0 0 0
6	0 0 0 0 0 0 1 0 0 1	6	0 1 1 0 0 0 1 0 0 1
7	0 0 0 0 0 0 0 0 1 0	7	0 0 0 0 1 1 0 0 2 0
8	0 0 0 0 0 0 0 0 0 0	8	0 0 0 0 0 0 0 0 0 0
9	0 0 0 0 0 0 1 0 0 0	9	0 0 0 1 0 0 2 0 0 0
10	0 0 0 0 0 0 0 0 0 0	10	0 0 0 0 0 1 0 0 0 0

Figure 14: Differences between GLCM's with and without the symmetry option.

Input Parameters Chosen

Because the expedited metric is intended as a surrogate measure of fractured surface area, it primarily focuses on boundary regions between bone and soft tissue. It does not require differentiating soft tissue structures from one another, nor does it require differentiating varying densities of cortical bone. As a result, to focus on those intensities important to the expedited metric, the gray limits were chosen to be 100 HU for the minimum and 1100 HU for the maximum. Anything less than 100 HU is treated as soft tissue and anything greater than 1100 HU is treated as cortical bone. Further differentiation beyond these limits is not necessary for the analysis. As can be seen in Figure 15 below, when the gray limits are applied to the initial image, the resulting rescaled image no longer contains any discrimination within the soft tissues and it shows no noticeable change in the cortical bone regions of the image, leaving just the region of interest for textural analysis.

When choosing the value for the number of levels, it was important to choose a value that was appropriate for the analysis. If a value too small was chosen, the rescaled image may lump differing structures such as the soft tissue and cancellous bone together. As a result, a bone edge may be lost in the resulting image. However, if the value is too large, it may excessively discriminate between structures and add unneeded calculation

time to the analysis due to the resulting larger GLCM. A value of 10 was decided to be the appropriate number of levels for the image. As seen in Figure 15, the chosen value shows discrimination between soft tissue and cancellous bone, and additional discrimination between cancellous and cortical bone. While no test was done to determine if this was the optimal number of levels, the results obtained for PTOA prediction using this value proved it to be an appropriate choice.

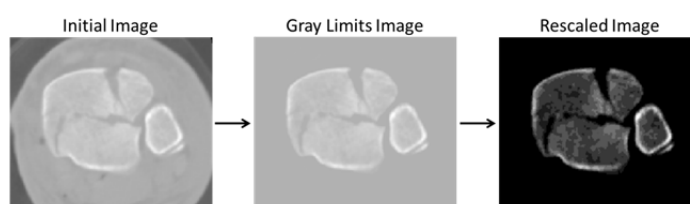


Figure 15: Image adjustment parameters applied to a CT image.

The offset and symmetry options were closely related in this application. When determining the input for the offset, four different directions were chosen with each bordering the pixel being analyzed. The pixels diagonally above and to the left, directly above, above and to the right, and directly to the right of each pixel were evaluated (Figure 16). Analyzing all eight neighboring pixels was deemed unnecessary because enabling of the symmetry option provides a comparable result. Because symmetry adds an additional count to the transverse location in the GLCM, the other pixel relationships are implicitly represented in the final analysis.



Figure 16: Neighboring pixel offsets chosen for the GLCM analysis.

GLCM Heterogeneity Property

Once the GLCM has been constructed, it is then passed to the GLCM properties function. The properties function analyzes the GLCM and returns four different properties describing the texture of the image: contrast, correlation, energy, and homogeneity. Contrast returns a measure of the intensity contrast between a pixel and its neighbors over the whole image. Correlation returns a measure of how correlated a pixel is to its neighbors over the whole image. Energy returns the sum of squared elements in the GLCM. Finally, homogeneity returns a value that measures the closeness of the distribution of elements in the GLCM to the GLCM diagonal.

After reviewing the four properties, it was decided that the homogeneity property was the most appropriate of the four to relate to fractured surface area. When calculating the homogeneity value, Equation 1 below is applied to each element of the GLCM, which is represented as the variable $p(i, j)$, where i and j represent the row and column positions of the GLCM. From the equation, one can see that the further the matrix element is from the diagonal of the matrix (i.e., the greater the difference between i and j), the greater the reduction in the count value at that element. The sum of the new matrix (q) is then divided by the sum of the original matrix (p) to obtain the homogeneity value (h) in Equation 2, which will range from 0 to 1.

$$\text{Equation 1:} \quad q(i, j) = \frac{p(i, j)}{1 + |i - j|}$$

$$\text{Equation 2:} \quad \text{Homogeneity } (h) = \frac{\sum_{i, j} q(i, j)}{\sum_{i, j} p(i, j)}$$

The homogeneity value was determined to be the most appropriate because it best captured the interfragmentary surface area of the fractured bone. When comparing the homogeneity value of a fractured limb to the limb before fracture (approximated by the intact contralateral limb), Figure 17, the fractured limb would contain the same pixel-to-pixel relationships in the GLCM with the exception of the interfragmentary surfaces.

Along these interfragmentary surfaces the previous bone-bone relationships of the intact limb would be replaced by a bone-soft tissue relationship in the fractured limb. The difference between these relationships should be greater for the bone-soft tissue relationships, placing a greater distribution of the counts further from the diagonal of the GLCM. After Equation 1 is applied to the intact and fractured GLCM matrices, the resulting sum of the fractured matrix will be less than the intact matrix due to this different distribution. As a result, the fractured homogeneity would be less than the intact, as shown in Figure 17.

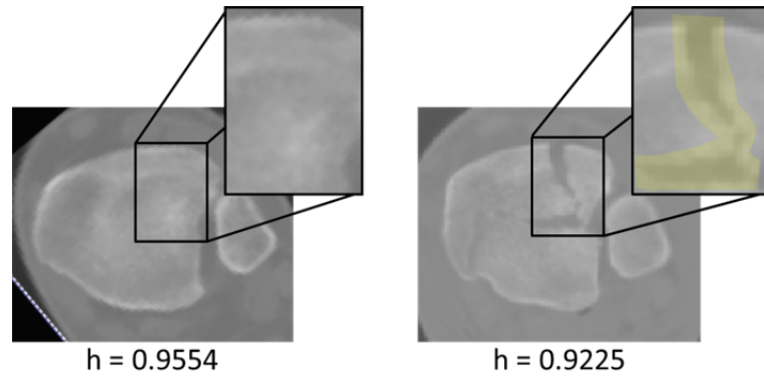


Figure 17: Homogeneity comparison (intact vs. fractured limbs).

This inverse relationship between CT intensity homogeneity and the fracture severity is less than ideal for purposes of assessment. For this reason, instead of looking at a fracture for its homogeneity, the property was adjusted to define the heterogeneity of the image (Equation 3).

Equation 3:

$$\text{Heterogeneity } (H) = 1 - \frac{\sum_{i,j} q(i,j)}{\sum_{i,j} p(i,j)}$$

Expedited Metric Preparation

Watershed Segmentation

Prior to applying the GLCM functions to the CT image data, the tibia needed to be isolated for analysis. The first step in the process was CT file management. The CT images were received as separate DICOM files, but they were then stacked into one NifTi file. Often the images extended well beyond the region of interest containing the fracture and presented an axial field of view much larger than the tibia, occasionally even including both limbs. To save time in the analysis, the image was cropped in all three planes to contain just the fractured tibia portion of the image.

The next step is to segment the tibia so as to exclude extraneous soft tissue, plaster casts, noise, and other bones from analysis. Rather than doing a manual segmentation on each slice of the image to isolate the tibia, the expedited metric utilized an existing 3D watershed segmentation method. The watershed segmentation method was previously developed to segment tibial fragments as a basis for later fracture reduction planning [57]. While this segmentation method was in a developmental stage and could not consistently and reliably provide segmentations similar to the manual segmentations, a portion of the code was found to provide a gross but sufficient segmentation for the GLCM analysis.

The initial step of the segmentation process was to choose a HU value for thresholding that would separate the tibia, fibula, and talus. Choosing a threshold that was too low would under-segment and combine the tibia, fibula, or talus bones together. A threshold chosen too high would over-segment the image and unnecessarily divide one fragment into two or more. Examples of different thresholds for one case can be seen in Figure 18 below.

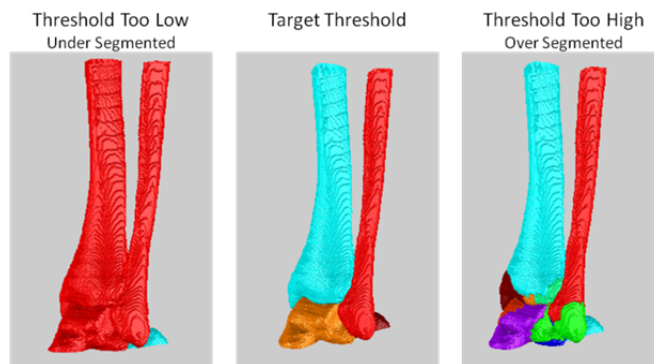


Figure 18: Effect of differing threshold values on the watershed segmentation.

Once an appropriate threshold value has been chosen, the watershed segmentation works to remove the fibula and talus from the overall segmentation of bone. It addresses fibular removal by analyzing the proximal slice of the segmentation. It separates different volumes in that slice and captures the area properties of each volume. All volumes located on the perimeter of the image are erased. This is done to rid the image of any plaster cast in the first slice. The remaining volume with the largest area, assumed to be the tibia, is then kept and all other volumes in the slice are erased from the overall segmentation. This results in the deletion of most fibular fragments. Next the distal slice is analyzed. The program assumes that the image has been appropriately cropped so that no portion of the tibia is located in the distal-most slice, and it erases all fragments located in that slice. This will ideally result in the deletion of the talus and any other bone or fragments in that slice. A segmentation containing just the tibia would be the ideal result obtained by applying this process. However, this is often not the case, and portions of the fibula, talus, or cast can still remain throughout the segmentation (Figure 19). As a result, these unwanted remnants need to be manually selected and removed from the segmentation. After all the unwanted remnants are removed, the remaining fragments are fused together into one object for the purposes of the remaining analysis.

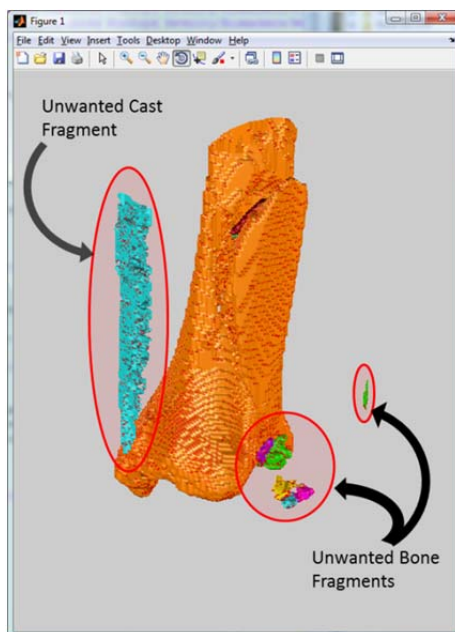


Figure 19: Unwanted fragments from the tibia segmentation. Unwanted fragments are not part of the tibia and want to be excluded from the GLCM analysis.

On occasion, a portion of the fibula or talus was found to be too close to the tibia to be differentiated by the segmentation method. Additionally, tibial fragments could be omitted from the segmentation in the removal processes. In these cases, the 3D volume of the segmentation along with the CT image data was transferred to the ITK-Snap program for manual additions or deletions of the tibia. While this process adds to the calculation time, the edits are generally minor and save overall time compared to re-running the segmentation process, which might not even fix the issue in the end.

Post Segmentation Setup

Once the segmentation has been finalized, a convex hull is fit to the image. The convex hull is a binary image that is formed by wrapping each fragment in each slice of the segmentation into one convex polygon. All pixels inside the polygon are then set to 1 and everything outside is set to 0, to create a binary mask. The convex hull is used to include any cancellous bone that may not have been captured by the watershed

segmentation. An example of a watershed segmentation result is shown in Figure 20. It is evident that the segmentation is particularly rough. This segmentation certainly could not be used for interfragmentary surface area calculation purposes, and additionally does not even include all of the cancellous bone if the GLCM analysis were run on just the segmented area. However, after applying the convex hull to the segmentation and analyzing just the highlighted region with the GLCM, all the bone and its corresponding relationships would be included.

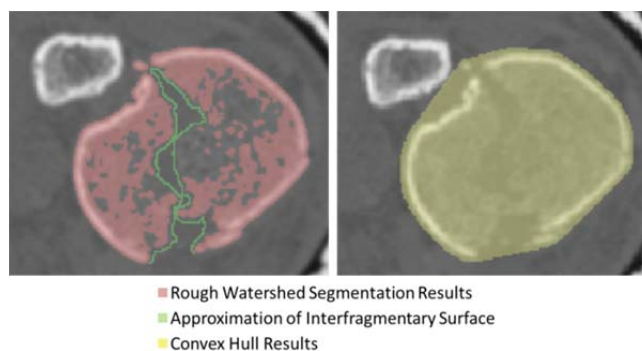


Figure 20: Watershed segmentation and convex hull results.

After the convex hull mask has been created, it is applied to the image to remove any bone that was determined not to be part of the tibia. This process removes most of this bone; however, the shape of the tibia near its distal end causes the convex hull approach to encompass parts of the fibula or talus, as seen in Figure 21. To account for these occurrences, the segmentation of the tibia was subtracted from the segmentation containing all bone in the image. What remained was a segmentation of all the bone not classified as tibia. The complement of this binary image segmentation was applied to mask the CT image, thereby removing all remaining unwanted bone from analysis.

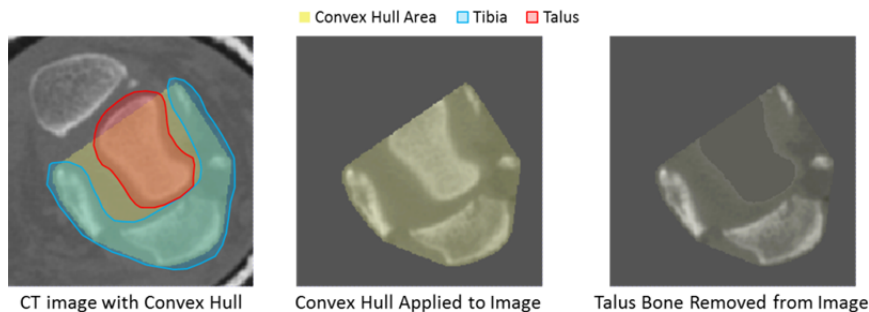


Figure 21: Distal fragment removal from convex hull.

Post GLCM Analysis Setup

The purpose of the previous steps was to create a CT image stack/volume encompassing only the tibia. It was on this image stack that the GLCM analysis was run and the heterogeneity properties were obtained. Similar to the prior fracture severity metric, the intact limb heterogeneity was subtracted from the fractured limb heterogeneity to obtain severity results. Before this could be done, the two limbs needed to be registered to one another so that similar regions of the bone were being compared. While multiple tibial landmarks were considered for the registration point, the articular surface of the tibia was decided to be the most appropriate registration position. This position was chosen because it most likely is the area through which the energy from the trauma was passed. The initial step in determining the image slice representing the articular surface was to focus on the distal 100 mm of the tibia. This was determined by locating the last slice in the segmentation of the tibia, and moving 100 mm proximally from there. The total intensity of each slice of the image passed to the GLCM analysis was then summed and plotted, represented by the blue curve in Figure 22.

After these summations were calculated, the slope of the summation curve was found for each point, represented by the red curve in Figure 22. The purpose of utilizing the slope of the curve was to isolate a window containing the articular slice, represented

by the teal highlighted region in Figure 22. The summation of intensity values for each slice located distally from the articular slice decreased since the amount of bone diminished after that point. The slope in this region typically contains the largest negative slope. This point thus determines the distal end of the window. Also, due to the large amount of cancellous bone and the sparse amount of cortical bone in the epiphyseal region of the tibia, a drop-off in the summation of intensities can additionally be seen slightly proximal to the articular surface. This usually will result in a local maximum in the slope. To locate this position the slope values are analyzed moving proximally from the distal window position until a positive slope of half the magnitude of the distal position slope is found. This then set the proximal window position.

The articular surface was then determined to be the point of maximum slice intensity within this window. The reason that the articular surface is the maximum point in this window is that the subchondral plate of the tibia is oriented more transversely than the cortical shell in the metaphyseal region. In addition to the graph of summations and their slopes for one case, Figure 22 also shows the calculated articular slice of that case from the transverse, sagittal, and coronal planes. The results proved to be an appropriate and repeatable landmark for the expedited fracture severity analysis.

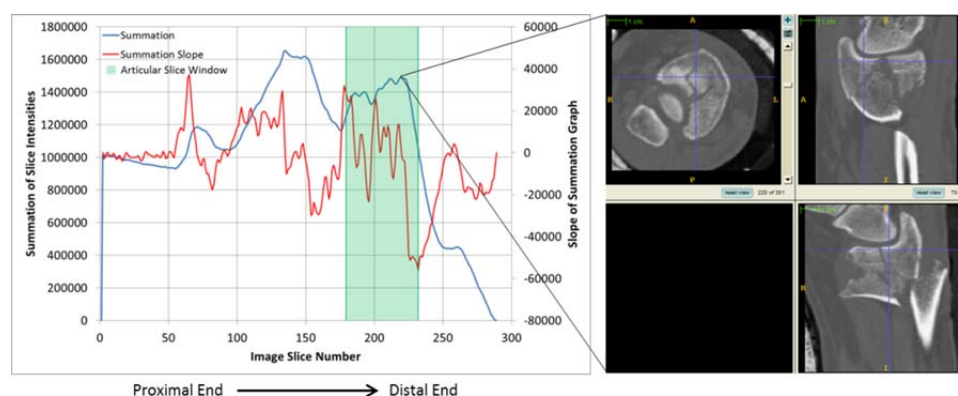


Figure 22: Articular slice selection graph and ensuing slice location.

Normalization of Intact Contralateral Limb

Just as for the prior fracture severity metric, the expedited metric required the inclusion of the intact contralateral limb for taring purposes. This requirement loomed as a major restriction in the development of this analysis for clinical use. Reliably obtaining a CT image that included this contralateral limb, which is not the standard of care, proved to be very difficult in the clinic. Logistical issues along with concerns regarding added radiation exposure to the patient limited the number of cases that could be obtained for analysis. A patient-specific method of normalization was therefore developed to serve as a surrogate for having CT data from the actual intact contralateral limb.

Prior normalization methods for use with the full fracture severity metric relied upon a single anthropometric scaling based on the patients' height [58]. Different settings and fields-of-view used while acquiring a CT scan can greatly influence the resulting image appearance. Normalizing for the GLCM texture analysis therefore required the inclusion of two additional parameters: spatial resolution of the CT image acquisition and CT image reconstruction settings. The first step in development of the normalization process was to determine the heterogeneity values for each intact limb available in the study. The heterogeneities were then summed from the distal to the proximal end of the limb. Using prior anthropometric data that an individual's tibia length is 0.246 times their height [59], the summation of each limb's heterogeneity was then plotted versus each slice's percent distance along the tibia, proximally from the articular surface of the limb. The initial distribution of these summations is shown in Figure 23 for 28 cases used in this normalization process. The goal of the normalization process is to reduce the scatter seen in this distribution, so that a function can be fit to the data to act as an intact surrogate model.

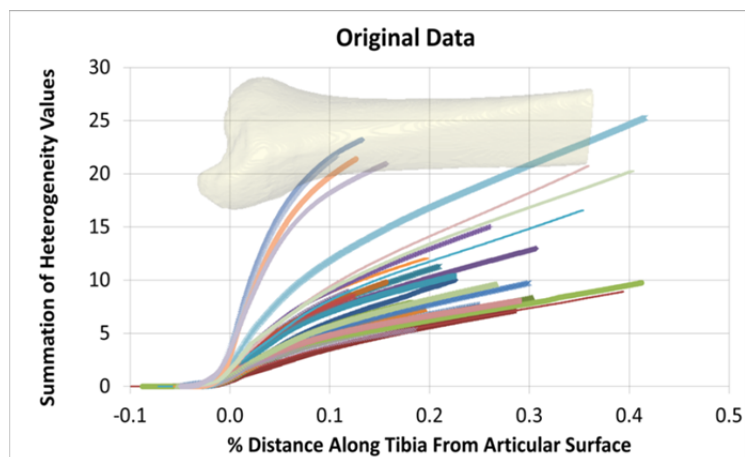


Figure 23: Initial distribution of heterogeneity summations.

CT Convolution Kernel

When creating a CT image, different convolution kernels can be chosen to show greater cancellous bone detail, to more greatly differentiate soft tissue structures, or to create a smooth image with limited noise. The specific kernel chosen can therefore cause differences in the resulting texture of the image. Some differences are subtle and small, while others are quite noticeable and cause significant differences in the resulting heterogeneity (Figure 24 – note the graininess for kernels B80f and B70s).

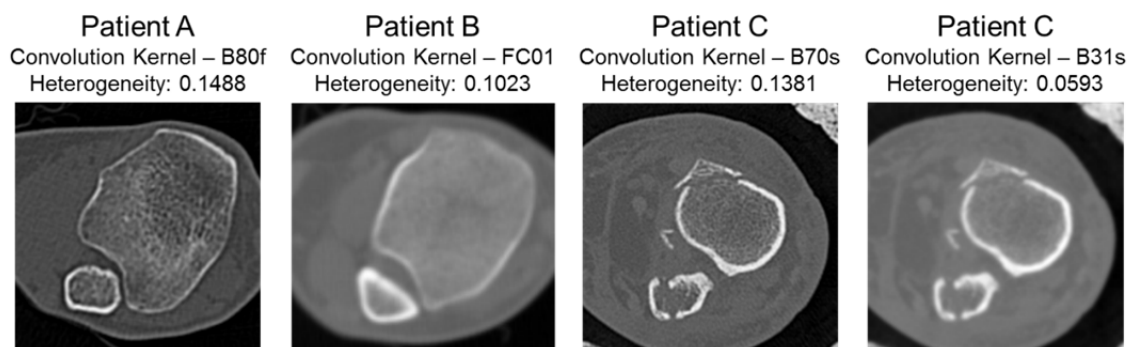


Figure 24: Convolution kernel effects on CT images.

To account for the different convolution kernels in patient CTs, an edge-preserving anisotropic diffusion filter was applied to each CT image. Applying this filter to each of the images, regardless of convolution kernel texture, would smooth over the cancellous bone regions and the soft tissue regions, while maintaining the bone-bone or bone-soft tissue edges. If the edges were also smoothed over, then some of the heterogeneity, and as a result some of the sensitivity to fracture edge, could be lost. It is in these edges that the heterogeneity and resulting fracture severity score is most affected, so preserving these edges is essential for the analysis.

An anisotropic diffusion filter was implemented in Matlab. The goal of this filter was to reduce the effect that the convolution kernel had on the baseline heterogeneity of the image, in as efficient a manner as possible. Smoothing over the image as much as possible without taking excessive time would reduce the effect of the convolution kernel, thus improving the distribution of the heterogeneity summation data for the intact limbs.

The Matlab filter required four different inputs: scheme, eigenmode, diffusion time step-size, and total diffusion time [60]. With all the different options, determining the settings to provide the best predictive results for the expedited metric would require substantial investigation. As a result, only some of the options chosen were investigated, merely to test the efficacy of the filter. These options produced an expedited severity metric with a strong predictive ability for PTOA outcome and were not further adjusted. Further investigation into these options (scheme and eigenmode) may provide further refinement to the normalization and resulting fracture severity results.

The first option chosen was the scheme. The scheme input determined the main analysis the filter applied to the image. Five separate schemes were provided with the filter. They included rotational invariance, optimized derivative kernels, implicit discretization, standard discretization, and non-negativity discretization. The rotational invariance option was chosen for the normalization process. This was chosen because the

tibia's shape in the transverse plane tends to be circular in nature. Choosing a scheme to account for this seemed like a sufficient place to begin for the filter.

The eigenmode input determined the method used in the partial differential equation used in the filter process. This input also offered a number of different options for the filtering process. The choices included a Weikerts equation - line like kernel option, a Weikerts equation - plane like kernel option, a coherence enhancing diffusion option, a hybrid diffusion with continuous switch option, and finally an edge-enhancing diffusion option. As already mentioned, because the heterogeneity is most affected by the relationships along bone edges, maintaining these structural edges after the filtering process was a goal in the normalization process. As a result, the edge enhancing diffusion eigenmode was implemented because it was thought to best maintain the structural edges.

The final two options for the Matlab anisotropic diffusion filter were then selected by adjusting them to obtain the smoothest image possible in a reasonable amount of time. The diffusion time step-size has a default value of 1 when the rotational invariance scheme is chosen. Based off the default value, the variable was chosen to be tested from 0.1 to 3.0 in increments of 0.1. The other input options were kept constant through the analysis. These options were set at rotational invariance for the scheme, edge enhancing diffusion option for the eigenmode, and 40 for the total diffusion time (determined from other testing of the filter). Figure 25 below shows the results of the analysis with graphs of the total calculation time for the filter and the output image heterogeneity versus the diffusion time step-size. Figure 26 shows the visual effects the different step-sizes had on the image chosen for the heterogeneity values in Figure 25.

From these figures, it is apparent that as the step-size increases, the calculation time decreases. The heterogeneity value also slightly increases with step-size increase from roughly 0.1 to 2.0. After this point, it appears that the filter scheme becomes unstable and thus not able to be used. Due to the significant decrease in calculation time

with only a slight increase in heterogeneity, it was decided to choose a step-size as large as possible, while still remaining stable. This would minimize the calculation time of the function, while having little ensuing effect on the heterogeneity value of the image. As a result, 2.0 was chosen as the diffusion time step-size input value for the anisotropic diffusion filter.

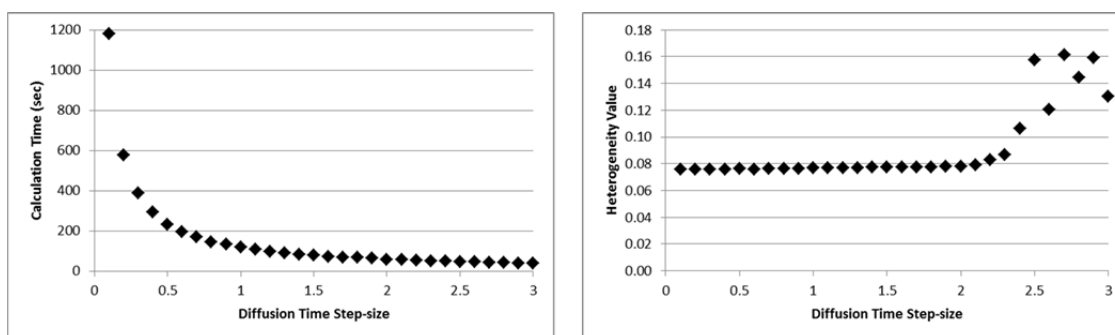


Figure 25: Effects of diffusion time step-size on calculation time and heterogeneity.

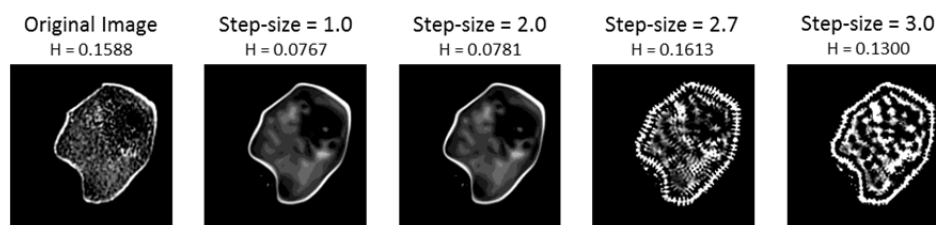


Figure 26: Effects of diffusion step-size on CT images.

The final input variable remaining was the total diffusion time. This variable determined the number of times that the filter would be applied to the image. With the rotational invariance scheme and edge enhancing diffusion eigenvalue chosen as inputs, the total diffusion time was then tested across a range from 1 to 44. With the step-size set at the default value of 1, changes to the calculation time and resulting heterogeneity

values of the output image were observed for the changing total diffusion time values. Figure 27 shows the changes in calculation time and heterogeneity value versus the changing total diffusion time values. Figure 28 shows the effects of the filter on the image at differing total diffusion time values compared to the original image.

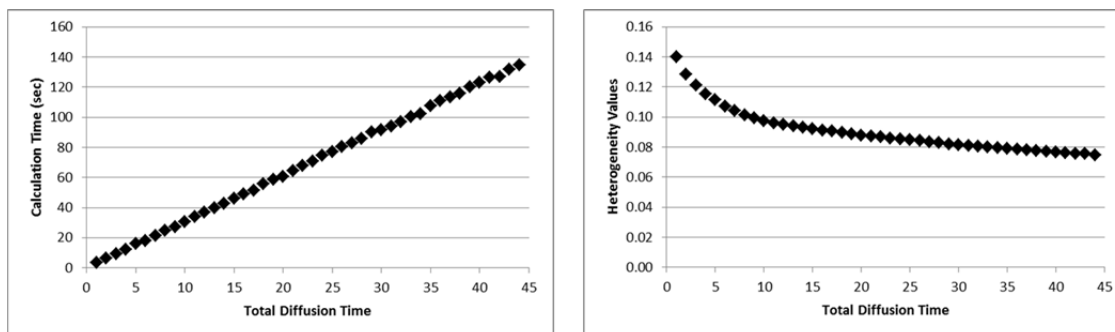


Figure 27: Effects of total diffusion time on calculation time and heterogeneity.

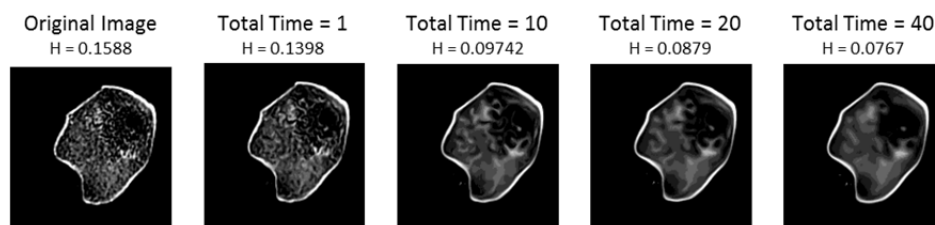


Figure 28: Effects of total diffusion time on CT images.

These figures show that as the total diffusion time increases, so does the calculation time, in a linear fashion. However, as the total diffusion time increases, the heterogeneity value decreases at a much more rapid rate initially, and then seems to settle into a slower, quasi-linear decrease. The final decision for determining the optimal total diffusion time input value was chosen by the minimal value that provided a satisfactory distribution for the normalization curve to be fit to. Values of 1, 5, 10, 20, 40, 60, and 80

were all included in this process. In the end, 80 was the value determined to provide a sufficient distribution amongst the intact cases. While this value did add time to the calculation, the added time was found to be worth the improvement in the distribution of the data.

With the input variables for the anisotropic diffusion filter chosen (scheme: rotational invariance, eigenmode: edge enhancing diffusion, diffusion step-size: 2.0, and total diffusion time: 80), the filter could be applied to the images. Results of the filter to the images previously shown can be seen in Figure 29, along with their adjusted heterogeneities. The images show a reduction in the differences of heterogeneity values between the images of different convolution kernels.

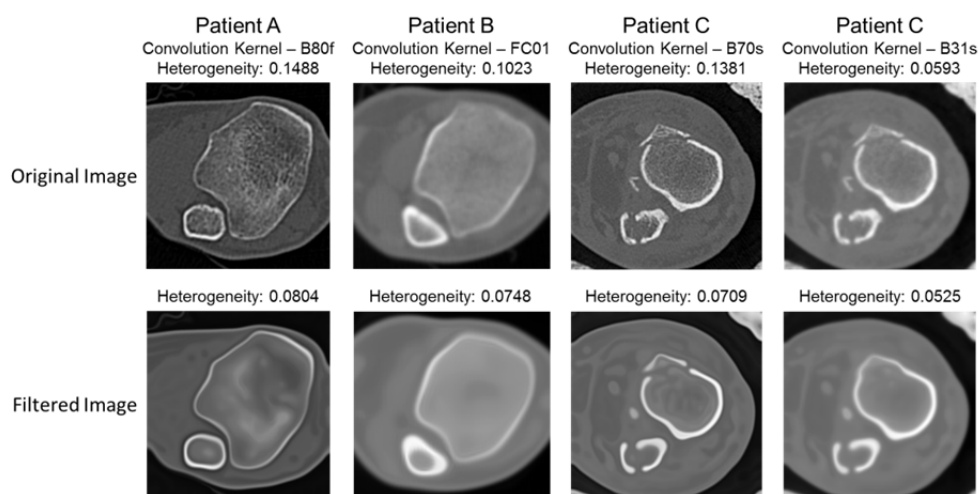


Figure 29: Effect of anisotropic diffusion filter on CT image and image heterogeneity.

With the filter applied to each of the 28 patients in the normalization analysis (Figure 30), the distribution showed some slight improvement over the original data. While this improvement is not satisfactory yet, it does show significant promise for the remaining normalization parameters.

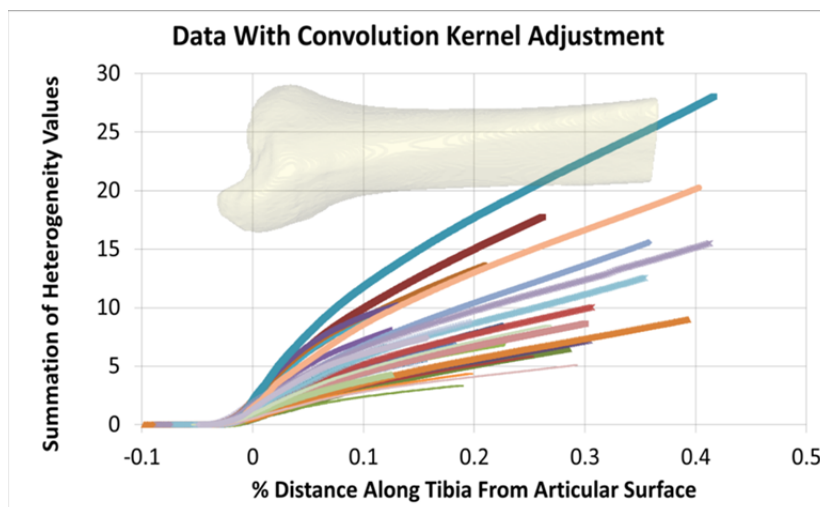


Figure 30: Effect of convolution kernel adjustment on heterogeneity summation.

CT Image Spatial Scaling

When performing the GLCM analysis on an image, the spatial properties of that image have a strong influence on the resulting heterogeneity. Three different image spatial factors were found to be particularly influential. These were (1) the image area analyzed, (2) the pixel size (i.e., the in-plane resolution) of the CT image, and (3) the CT slice thickness. The first of these three, image area analyzed, was found to have the greatest influence.

If the heterogeneity of an image whose area is analyzed is half the area of a second image analyzed, a significant difference would most certainly be seen. For example, Figure 31 below shows a single slice of a patient's CT scan run through a GLCM analysis with differing areas. In the figure, the areas analyzed are represented by the red lines. As the area analyzed decreases, the heterogeneity increases, to the point where the final image has more than double the heterogeneity of the first image. This difference is due to the decrease in the number of 1-1 relationships analyzed by the GLCM. The GLCM relationships seen around the bone remain the same throughout each image; however, there is less background and hence fewer 1-1 relationships to query.

This reduces the number of counts located along the diagonal of the GLCM, makes the heterogeneity value more dependent on the pixel relationships located further away from the diagonal. To accommodate this, each intact CT was standardized to involve roughly the same in-plane area ($\sim 4500 \text{ mm}^2$).

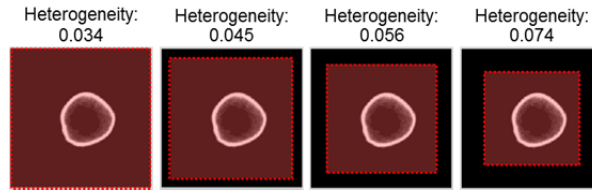


Figure 31: Effect on heterogeneity of the image area analyzed.

Upon further investigation, it was determined that the change in heterogeneity could be calculated if the original image GLCM and the standardized (new) image GLCM were known. To explain this conversion some variables need to be introduced:

H_o : Heterogeneity of Original Image

H_n : Heterogeneity of New Image

h_o : Homogeneity of Original Image

h_n : Homogeneity of New Image

$GLCM_o^p$: Original GLCM before Equation 1

$GLCM_n^p$: New GLCM Matrix before Equation 1

$GLCM_o^q$: Original GLCM after Equation 1

$GLCM_n^q$: New GLCM Matrix after Equation 1

It is already known from Equations 1 and 2 that:

Equation 4:
$$H_o = 1 - h_o = 1 - \frac{GLCM_o^q}{GLCM_o^p} = \frac{GLCM_o^p - GLCM_o^q}{GLCM_o^p}$$

and

Equation 5:
$$H_n = 1 - h_n = 1 - \frac{GLCM_n^q}{GLCM_n^p} = \frac{GLCM_n^p - GLCM_n^q}{GLCM_n^p}$$

Given that the only difference between the standardized image and the old image is background pixels of 1, the only difference between the new and old corresponding GLCM matrices is the value at the (1,1) location. For example:

$$GLCM_o^p = \sum \begin{bmatrix} 10 & 2 & 3 \\ 4 & 7 & 4 \\ 9 & 2 & 6 \end{bmatrix} = 47 \quad \text{and} \quad GLCM_n^p = \sum \begin{bmatrix} 3 & 2 & 3 \\ 4 & 7 & 4 \\ 9 & 2 & 6 \end{bmatrix} = 40$$

Applying Equation 1:

$$GLCM_o^q = \sum \begin{bmatrix} 10 & 1 & 1 \\ 2 & 7 & 2 \\ 3 & 1 & 6 \end{bmatrix} = 33 \quad \text{and} \quad GLCM_n^q = \sum \begin{bmatrix} 3 & 1 & 1 \\ 2 & 7 & 2 \\ 3 & 1 & 6 \end{bmatrix} = 26$$

From this example, and given the fact that only the (1, 1) location will change between the new and old matrices, the following equation can be derived:

$$\text{Equation 6:} \quad GLCM_n^p - GLCM_o^p = GLCM_n^q - GLCM_o^q = \begin{bmatrix} -7 & 0 & 0 \\ 0 & 0 & 0 \\ 0 & 0 & 0 \end{bmatrix} = -7$$

Solving for $GLCM_n^q$, it follows that:

$$\text{Equation 7:} \quad GLCM_n^q = GLCM_o^q + (GLCM_n^p - GLCM_o^p)$$

Substituting this value into Equation 5 produces the following result:

$$\text{Equation 8:} \quad H_n = \frac{GLCM_n^p - [GLCM_o^q + (GLCM_n^p - GLCM_o^p)]}{GLCM_n^p} = \frac{GLCM_o^p - GLCM_o^q}{GLCM_n^p}$$

Dividing the new heterogeneity by the old heterogeneity then yields:

$$\text{Equation 9:} \quad \frac{H_n}{H_o} = \frac{\frac{GLCM_o^p - GLCM_o^q}{GLCM_n^p}}{\frac{GLCM_o^p - GLCM_o^q}{GLCM_o^p}} = \frac{GLCM_o^p}{GLCM_n^p}$$

Equation 9 can then be rewritten as:

$$\text{Equation 10:} \quad H_n = \left(\frac{GLCM_o^p}{GLCM_n^p} \right) H_o$$

If the given area analyzed is a rectangular box, then the $GLCM_o^p$ and $GLCM_n^p$ variables can be determined as long as the new and old image dimensions are known. The variables mentioned are simply the total count of relationships in an image. Since we know the size of the image and the directions of the relationships analyzed in the GLCM process, we can determine the total count of relationships in each image. For each relationship, the number of counts is the height times the width of the image, minus the number of edge pixels needing to be ignored due to non-existent neighbors. Choice of

the symmetry option for utilization in the GLCM process means that we must double the total count for each relationship. After analyzing each of the four relationships for edge pixels, and summing the total count together, the GLCM count can be calculated using Equation 11.

$$\text{Equation 11: } \text{GLCM total count} = 8(\#rows)(\#columns) - 6(\#rows + \#columns) + 4$$

Substituting Equation 11 into the appropriate locations in Equation 10 we get:

$$\text{Equation 12: } H_n = \left(\frac{8(\#_o \text{ rows})(\#_o \text{ columns}) - 6(\#_o \text{ rows} + \#_o \text{ columns}) + 4}{8(\#_n \text{ rows})(\#_n \text{ columns}) - 6(\#_n \text{ rows} + \#_n \text{ columns}) + 4} \right) H_o$$

From this equation, a new heterogeneity can be calculated from the old heterogeneity.

The only requirements for the equation to be functional and remain valid are that the size of each image must be known and that only the background (pixels of intensity value equal to 1) is removed or added in the adjustment between the images. This equation is capable of adjusting to any of the image area differences seen in the normalization process or in the expedited severity metric.

As mentioned, other spatial properties were found to also affect the heterogeneity of an image. When capturing the CT image, the size of each pixel and its thickness can vary between scans. If the final CT image focuses on one limb in the image, the pixel size can vary greatly compared to the pixel size of a CT image containing both limbs. In the 28 patients observed in this normalization study, the pixel size ranged from 0.244 mm to 0.782 mm. These differences in pixel size can cause significant differences in the gradient of intensities (i.e., the texture) seen on structure borders, as shown in Figure 32. This difference in gradient can have a significant effect on the resulting heterogeneity. It is due to this difference that a scaling factor based upon the pixel size was applied to the resulting heterogeneity.

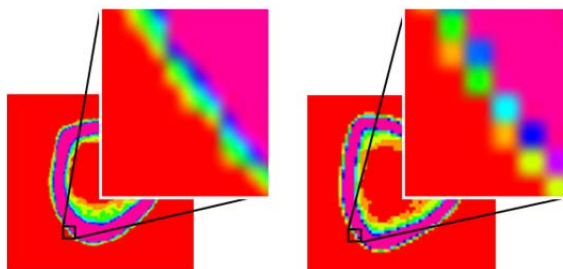


Figure 32: Effect of in-plane pixel size on image texture.

While the difference was significant, dividing by the actual pixel size proved to be overcompensation. However, dividing by the square root of the pixel size proved to best account for these differences. Given the square dimensions of the image, dividing by the square root of the pixel size seems logical. This adjustment disentangled the differences in heterogeneity and also accommodates for some of the gradient difference seen.

Additionally, differences in CT machines used along with other parameters in scanning the patient can vary the resulting thickness of each slice. The slice thickness among these patients ranged from 0.5 mm to 1.0 mm. When the sum of the heterogeneities for one CT scan with a slice thickness of 0.5 mm are compared over the same physical distance to the summation for a CT scan with slice thickness of 1.0 mm, a difference will be observed simply because of the difference in the number of slices included. The CT scan with slice thickness 0.5 mm would have twice as many slices analyzed, resulting in a heterogeneity summation roughly twice as high as the CT image with a 1.0 mm slice thickness.

To adjust for these differences, the heterogeneity for each slice is multiplied by the slice thickness.

When the adjustments made for image area analyzed, in-plane pixel size, and slice thickness are added to the adjustments already made for convolution kernels, an even greater improvement in the distribution of the data can be seen (Figure 33).

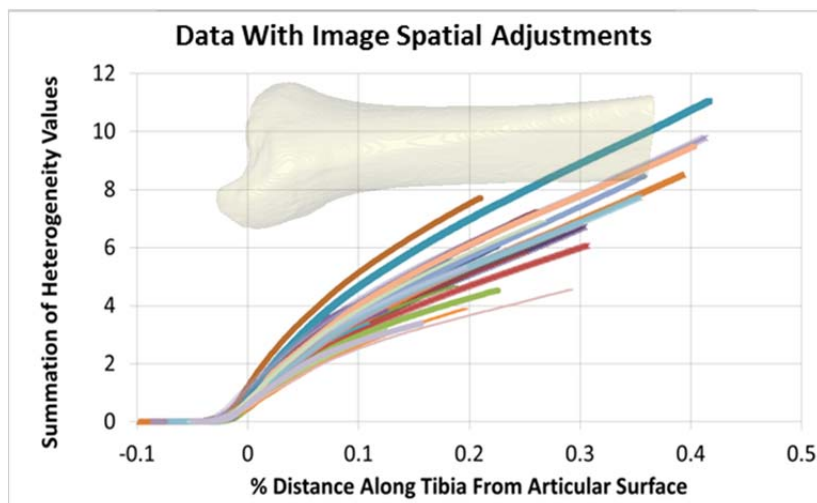


Figure 33: Effect of CT image spatial adjustments on heterogeneity summation.

While this distribution is approaching the point where a curve or curves could be fit to the distribution and used in place of the actual intact values, it still requires one final normalization step. As mentioned initially in this section, patient-specific anthropometric data were also used in the normalization process. Differences in a patient's height and weight can have an effect on their bone size and bone density. While these differences do not have a large influence on the resulting heterogeneity of the image, they are a factor when taking a summation of heterogeneities over a given distance. Therefore, by dividing by scaling factors based upon the patient's height and weight, a final adjustment could be made to the already improved distribution of intact heterogeneity summations, seen in Figure 34. This distribution was determined to be sufficient for curve fitting to move forward and develop a model representation for the data.

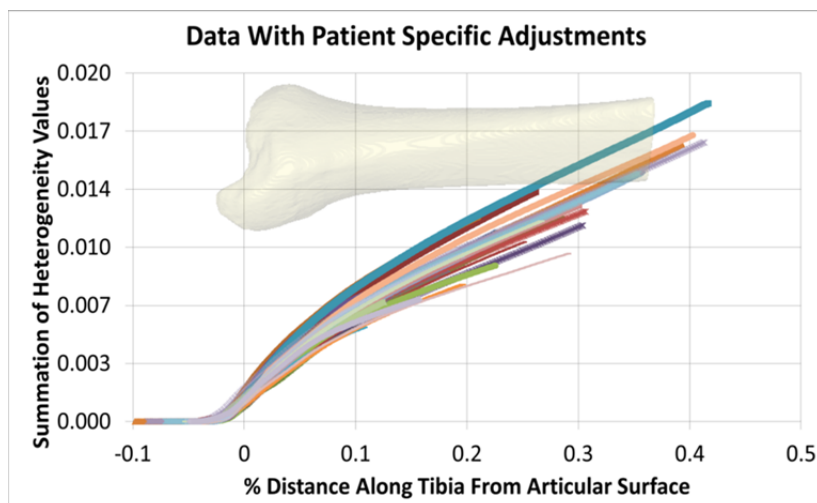


Figure 34: Effect of anthropometric adjustments on heterogeneity summation.

Intact Surrogate Curve

After looking at the data distribution, it was decided that a simple, bi-linear fitting of the data would work as an intact surrogate model. The point of convergence for these two lines was empirically chosen to be at a length 10% proximally up the tibia from the articular surface. The data were then split into the data proximal to this location and the data distal to this location. A line was fit to the proximal region of the data, and after the distal data were trimmed to the relevant data, a line was fit to that region. The results of the curve fittings can be seen in Figure 35. The two curve fittings were then saved for use later in the severity component calculations.

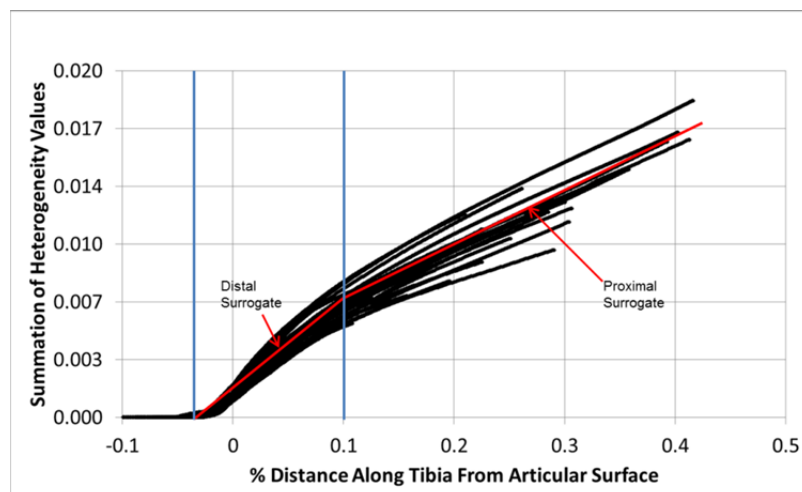


Figure 35: Proximal and distal curve fittings to the surrogate intact heterogeneity distribution data.

Calculation of Severity Components

To derive a comprehensive fracture severity score, an effort was made to include the same severity components in the expedited approach as in the prior full severity metric. The components of fracture energy, dispersion, and articular comminution were modeled after those of the full metric components, but derived only from the GLCM and heterogeneity, in lieu of fractured surface area.

Fracture Energy Surrogate

In the full severity metric, the fracture energy was mainly determined by subtracting the fractured surface area from the intact surface area. In a similar fashion, the expedited severity metric developed a surrogate of the fracture energy by subtracting the fractured heterogeneity from the intact heterogeneity. Before this could be done, however, the two limbs needed to be registered and the length of the fracture along the tibia needed to be determined. As already discussed, the registration of the two limbs was done by determining the articular surface of the intact and the fracture tibia and utilizing this location as a common point between the two.

The next step was to determine the first slice of the CT which contained a fracture. To find this location, the CT image was masked using the segmentation of the tibia. The resulting image was then thresholded using a binary matrix with a threshold value of 1300 HU. The analysis then looked for a change in the number of fragments of the resulting matrix. Starting at the proximal-most slice of the image and moving distally, the first slice which contained two fragments along with the previous slice was designated as the first fractured slice. Two consecutive slices were required to ensure that a fragment was isolated as opposed to errors caused by noise that are only present in single slices. To account for slight error, the calculation used the slice located 5 mm proximally from this slice.

With the articular slice and the first fractured slice calculated, the fracture length was then determined. This distance was determined by first subtracting the articular slice from the first fractured slice then multiplying by the slice spacing to get the physical length of the fracture. The fracture length was then divided by the length of the tibia. Once the fracture length was determined as a percentage of the length of the tibia, the heterogeneity values were summed for the fractured limb from the most distal portion of the tibia to the calculated first fractured slice. The corresponding intact heterogeneity surrogate summation was then subtracted from the fractured heterogeneity summation to determine the fracture energy surrogate. It is important to note that this measurement is not a direct measurement of fracture energy. Rather, it was a surrogate value developed to capture the interfragmentary surface area through the heterogeneity property.

Dispersion

As a direct result of the insulting trauma to the tibia, the fragments of the fractured bone are displaced and dispersed from each other. As a general rule, the more dispersed the bone fragments, the more severe the trauma to the joint. The expedited metric developed a component to incorporate this property into the analysis. One

significant difference between this component and its counterpoint in the full severity metric is that the expedited metric looked only at the dispersion of the fragments but not at the displacement. However, in the end, dispersion alone provided a sufficient PTOA predictive ability for the expedited severity metric.

To calculate the dispersion component, the expedited metric only required the GLCM, and not the heterogeneity property. Before trauma occurred, the convex hull of the segmentation of the intact bone would mostly be comprised of bone-bone (higher intensity) relationships. As a result, the (1, 1) location of the GLCM, which represents the soft tissue or background relationships, should have a relatively low count at that position. After the insult, with the fragments dispersed from one another, soft tissue and lower intensity materials would occupy the space between the bones. As a result, the number of 1-1 relationships seen within the convex hull of the fractured limb would be greater (Figure 36). The greater the dispersion, the greater the change would be in the counts at the (1, 1) location of the GLCM.

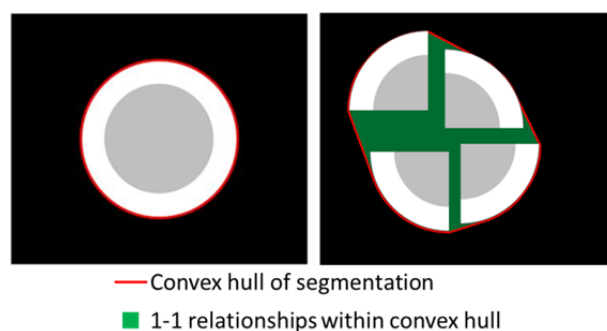


Figure 36: Example showing 1-1 relationship (green) differences between the intact and fractured limbs. The 1-1 relationship is used to determine fragment dispersion.

The dispersion component utilized this concept. To calculate this component, the fractured CT image was multiplied by the convex hull (mask) of the fractured limb.

Anything outside of the convex hull was set to Not-a-Number (NaN). Setting these values to NaN effectively excluded them from the formation of the GLCM. The GLCM was then formed for the portion of the image inside the convex hull. The 1-1 values of the matrix were then summed over the length of the fracture and multiplied by the normalization factors for CT image spatial differences. The result provided a comparable measure for the dispersion of the fracture, which could be incorporated in the expedited metric.

Articular Comminution

The third and final component of the expedited metric involves articular comminution. The articular comminution component of the full expedited severity metric was determined by calculating the percent difference between the surface area of the fractured limb and the intact limb over the articular slice of the limb. When calculating the articular comminution for the expedited metric, two methods were considered. The first was to calculate a percent difference between the fractured limb and the surrogate intact limb heterogeneities, just as the full metric did. The second was to compare the dispersion of the fragments over the articular region.

When the articular comminution was calculated in the full metric, a 3 mm region was analyzed, centered on the articular slice of the image. The 3 mm region was found to be the optimal area to analyze for measuring articular comminution in the full metric. When using the intact contralateral limb in the expedited metric, the 3 mm region was also found to produce the best results. However, when the intact surrogate curve was used in place of the actual intact values the concordance for the articular comminution when compared to the KL score in the expedited metric dropped from 81.4% to 48.1%. The main reason for this significant change was due to the inaccuracy of the surrogate model curve in the articular region. When utilizing the surrogate curve for the fracture energy component, the gross value of the curve was used. The gross value provided an

end value similar to that seen for the actual intact limb. However, the articular region focused on a very small portion of the curve (Figure 37). Because of the great variation in the slopes of the curve at this location, the surrogate curve could not be used to represent the actual intact values in this region.

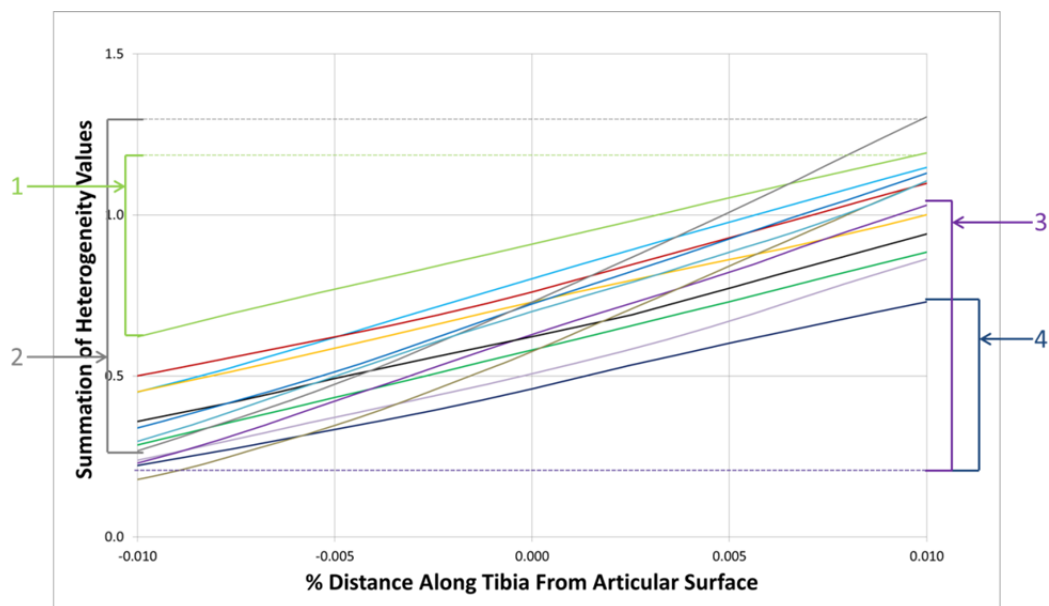


Figure 37: Differences in surrogate curves around the articular region with 4 different slopes isolated showing the variation seen in this region.

This issue led to the investigation of using a measurement other than the heterogeneity value to calculate the articular comminution portion of the metric. Because it was only calculated from the fractured image and did not rely on the intact surrogate curve, dispersion was the next method used to calculate the articular comminution. The first item to investigate with this new method would be the region of interest. When using the heterogeneity values to calculate the articular comminution, a 3 mm region was chosen as the optimal region to calculate the value, but it was not clear if this would also be an appropriate region using dispersion.

An analysis was run calculating the dispersion of the fractured limb at four different region sizes: 3, 6, 9, and 12 mm. Each region was centered on the articular slice of the limb. The results were then compared to the KL scores and the resulting concordances were compared. Additionally, the cases that developed OA were compared to those that did not develop OA. A p-value was then calculated using the Wilcoxon Ranked Sum test, comparing the dispersion values between these two groups. In the end, it was determined that the 9 mm length was the optimal region. It showed the highest concordance, 68.3%, and the lowest p-value, 0.0235, of all the regions (Table 2).

Table 2: Results of varying ROI's for articular disruption using dispersion.

	3mm	6 mm	9 mm	12 mm
Concordance	68.3 %	67.1%	68.3%	66.9%
P-Value	0.0325	0.0292	0.0235	0.0263

Combined Metric

The final step in determining a severity score for the expedited metric was to combine the three components (fracture energy, dispersion, and articular comminution) into a single comprehensive severity metric. To do this, each component was normalized so that values ranged from 0 to 100. Their contributions were then tested at different percentages of the combined metric ranging from 0% to 100%. The resulting combined metric values were compared among the 30 cases analyzed and a concordance value was calculated by comparing the combined values to their KL scores. After the components were analyzed for all possible variations between 0% and 100%, an optimum combination was determined. From this, the optimal combination was determined to be 32% fracture energy, 60% dispersion, and 8% articular comminution.

CHAPTER FOUR: RESULTS

The expedited fracture severity approach was used to analyze the pre-operative CT scans of 30 patients with tibial plafond fractures (18 male and 12 female). In addition to the 20 patients previously analyzed using the full fracture severity assessment methods, an additional 10 patients were analyzed for the expedited severity metric. These cases could not be analyzed before primarily due to the intact contralateral limbs being absent in the pre-operative CT scans.

Details regarding patient demographics, CT image spatial properties, and the CT convolution kernels are included in Table 3. The same inclusion criteria were used for patient eligibility in the expedited severity metric as for the full severity metric: an isolated closed or open fracture treated using a splint or a spanning external fixator to return the limb to normal length and alignment, and a CT scan covering the entire length of the fracture. One significant difference between the full severity metric criteria and the criteria for the expedited severity metric was that the expedited metric did not require the inclusion of the intact contralateral limb in the CT image, due to the normalization attributes of the expedited metric.

Table 3: Patient age, sex, height, weight, in-plane pixel size (mm), CT image slice thickness (mm), and convolution kernel used in CT image reconstruction for each case.

Case	Full Metic Case	Age	Sex	Height (cm)	Weight (kg)	In-Plane Pixel Size	CT Slice Thickness	Convolution Kernel
1	X	26	F	160	61.4	0.47	0.50	FC01
2		42	F	160	69.4	0.35	0.30	B31s
3		40	F	170.2	170.5	0.66	0.30	B80s
4		23	F	160	69.6	0.28	1.00	FC01
5	X	55	F	162.5	72.7	0.43	0.30	B80s
6		49	F	152.4	59.9	0.41	0.50	FC01
7	X	28	M	190.5	70.0	0.39	0.30	B80s
8	X	29	M	188	97.0	0.33	0.50	FC01
9		21	M	179	87.2	0.49	0.50	FC01
10	X	20	M	175.3	55.0	0.51	1.00	FC01
11	X	37	F	162.5	79.5	0.33	0.50	FC01
12	X	48	F	162.5	62.0	0.55	0.50	FC01
13		57	F	158.8	89.8	0.41	0.50	FC03
14	X	36	F	170.2	72.3	0.68	0.50	FC01
15		41	M	180.3	95.3	0.46	0.30	B80f
16		54	M	181	80.4	0.36	0.50	FC01
17	X	40	M	180	84.1	0.68	0.50	FC01
18	X	24	M	177.8	80.9	0.66	0.50	FC01
19	X	57	F	180.3	86.2	0.63	0.50	FC01
20	X	25	M	170	90.9	0.28	0.50	FC01
21	X	64	M	178	95.0	0.25	0.50	FC01
22	X	26	M	175	120.5	0.33	0.30	FC01
23	X	21	M	190.5	113.6	0.59	0.50	FC01
24	X	41	F	167.6	75.0	0.33	0.50	FC01
25		42	M	177.8	109.0	0.24	0.50	FC01
26		40	M	177.8	86.2	0.39	0.50	FC01
27	X	26	M	180.3	110.0	0.29	0.50	FC01
28	X	34	M	180	83.0	0.24	0.50	FC01
29	X	42	M	184	89.3	0.41	0.30	B31s
30	X	56	M	182.9	154.2	0.78	0.50	FC01

Articular Slice Location

Since proper identification of the fractured articular surface is important in accurately determining the fracture energy component of the severity metric, the automated articular slice selection for each limb was carefully analyzed. The results show a consistent selection of slices at the plafond of the tibia (Figure 38), providing visual evidence of the robustness of the approach. From these images, the variety in severity and type of fractures at the articular surface can also be seen.

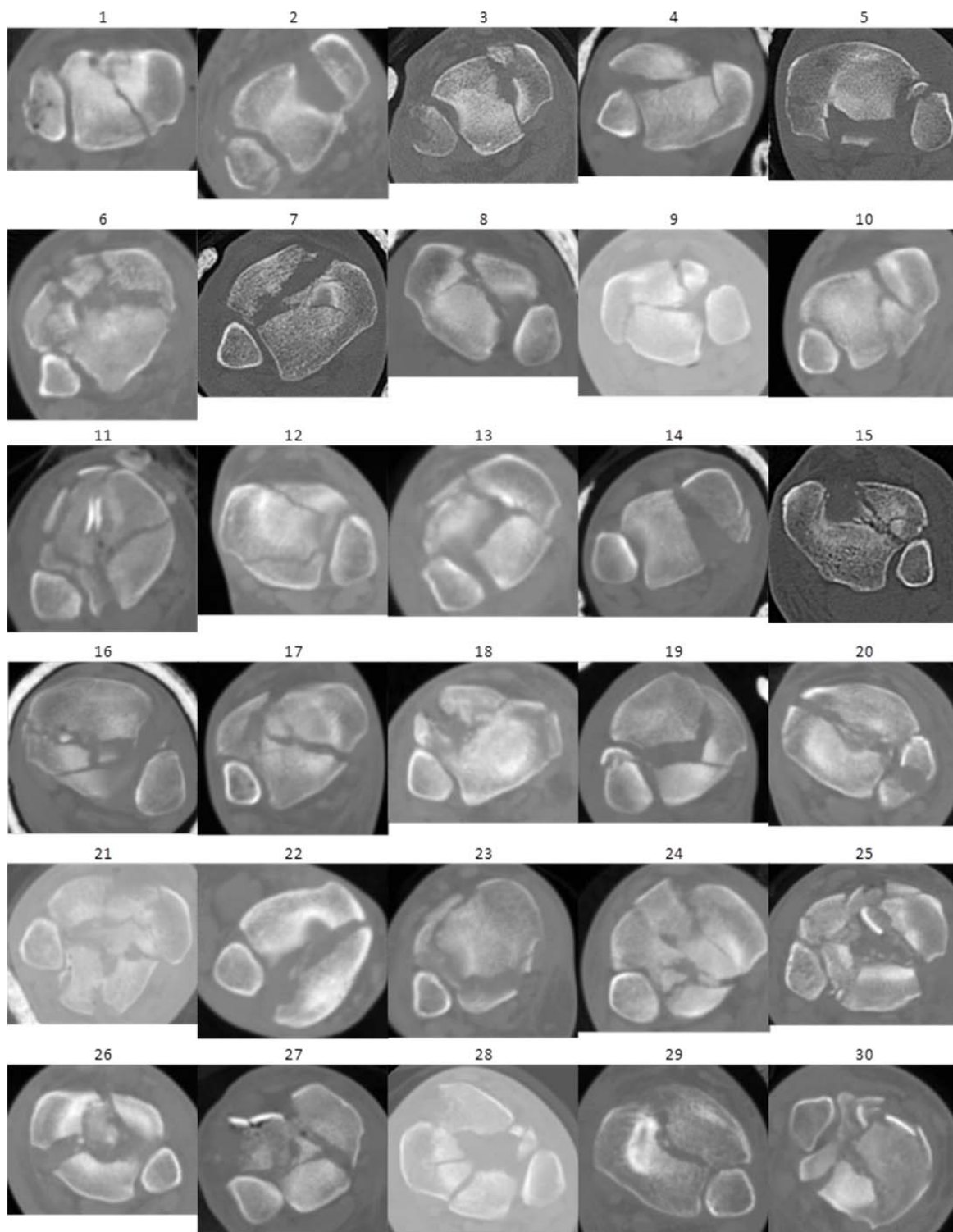


Figure 38: These CT images are from the slices identified as involving the articular surface for each case.

Expedited Severity Component Results

The details of the results for the expedited severity assessments are shown in Table 4. The fracture energy surrogate values ranged from -0.79 to 2.96. It is important to note that this is only a surrogate value for the energy, so a negative value here is possible. Additionally, while the surrogate model curve works to replicate intact limb heterogeneities quite well, it is still a surrogate representation. Consequently, it is likely that the surrogate curve overestimated the intact representation, resulting in negative values for fractures of lower severity.

Table 4: Severity component results from expedited metric analysis.

Case	Initial Metric	KL Scores	Fracture Energy	Articular Dispersion (mm ³)	Overall Dispersion (mm ³)	Case	Initial Metric	KL Scores	Fracture Energy	Articular Dispersion (mm ³)	Overall Dispersion (mm ³)
1	X	0	-0.08	1352	5847	16		3	0.82	3587	27331
2		0	-0.78	4274	15046	17	X	1	1.32	3632	26984
3		2	-0.22	3411	10598	18	X	3	1.80	3513	22886
4		0	-0.79	2302	20928	19	X	1	1.77	4093	23668
5	X	0	-0.49	3471	18777	20	X	2	0.32	3545	38362
6		4	0.31	2407	15093	21	X	3	-0.75	2812	51839
7	X	0	0.51	4609	16918	22	X	3	1.31	5266	37637
8	X	0	0.51	2745	19082	23	X	4	1.90	4758	32874
9		0	0.76	1807	18314	24	X	0	1.50	5666	39233
10	X	0	1.25	1778	15499	25		3	1.54	5487	39425
11	X	2	1.26	2685	15233	26		3	1.86	4893	47853
12	X	1	1.14	1869	18200	27	X	4	1.80	6334	47551
13		3	0.79	4210	19733	28	X	4	1.34	7449	51339
14	X	3	0.65	3644	23016	29	X	2	1.27	5484	67548
15		2	1.29	4665	17397	30	X	2	2.96	7956	80639

The values observed in the overall dispersion for the fractures ranged from 5.8 to 80.6 cm³. These values are roughly twice as large as the range observed by the full severity metric, 3.8 to 48.5 cm³. A reason for this difference could be that the expedited metric is most likely including some additional area in its calculation. Because the expedited metric does not use the intact limb, the fractured limb is the only source to measure the dispersion currently. Anything that does not have a 1-1 relationship (neighboring pixel intensity relationships of 1 and 1) within the convex hull of the

fractured image is considered part of the intact surrogate area. Anything that does have a 1-1 relationship is assigned as part of the dispersion area. However, this area may also be present in the intact bone. 1-1 relationships may exist, especially in the proximal regions of the bone where the medullary cavity is present and in the distal regions where the tibia bone begins to taper and it appears elongated and convex in cross-section (Figure 39). With these areas included in the expedited metric it would be understandable that the values are higher, possibly to the point of being almost twice as large. The articular dispersion values ranged from 1.35 to 7.96 cm³. These values seem reasonable, especially considering that the overall dispersion component seems to be estimating the values at approximately double the comparable values of the full metric.

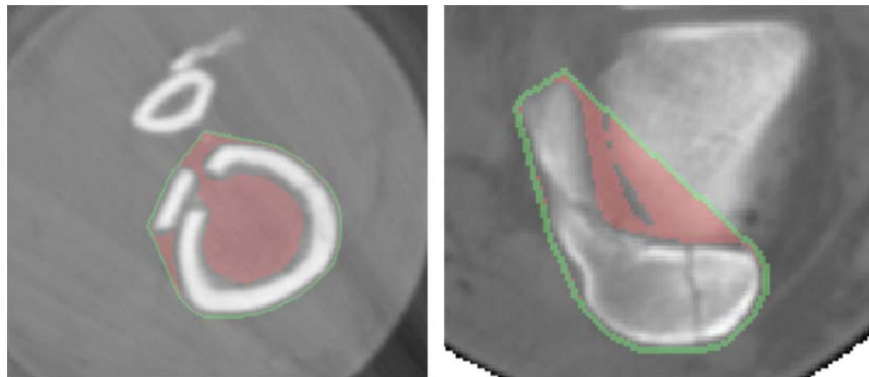


Figure 39: 1-1 relationship at the proximal end of the tibia with medullary cavity area included (Left) and the distal end where bone is tailing off (Right). (Convex Hull - Green, 1-1 Relationships - Red).

As mentioned previously, the optimal contribution of each of the components to the combined score is 61% for overall dispersion, 33% for fracture energy, and 6% for articular dispersion. With each component normalized to range from 0 to 100, 0 being the least severe and 100 being the most, the combined scores were calculated (Table 5).

Table 5: Normalized components and combined scores for expedited severity metric.

Case	Initial Metric	KL Scores	Normalized			Combined Score	Case	Initial Metric	KL Scores	Normalized			Combined Score
			Fracture Energy	Articular Dispersion	Overall Dispersion					Fracture Energy	Articular Dispersion	Overall Dispersion	
1	X	0	18.91	0.00	0.00	6.24	16		3	43.00	33.84	28.73	33.74
2		0	0.09	44.24	12.30	10.19	17	X	1	56.37	34.52	28.26	37.91
3		2	15.23	31.17	6.35	10.77	18	X	3	69.11	32.72	22.78	38.67
4		0	0.00	14.38	20.16	13.16	19	X	1	68.45	41.51	23.83	39.61
5	X	0	8.05	32.09	17.29	15.13	20	X	2	29.68	33.21	43.47	38.31
6		4	29.43	15.97	12.36	18.21	21	X	3	0.98	22.11	61.49	39.16
7	X	0	34.57	49.32	14.80	23.40	22	X	3	55.95	59.26	42.50	47.95
8	X	0	34.62	21.09	17.70	23.49	23	X	4	71.83	51.58	36.14	48.84
9		0	41.42	6.89	16.67	24.25	24	X	0	61.13	65.32	44.64	51.32
10	X	0	54.40	6.45	12.91	26.21	25		3	62.07	62.61	44.89	51.63
11	X	2	54.62	20.19	12.55	26.89	26		3	70.60	53.62	56.16	60.78
12	X	1	51.46	7.82	16.52	27.53	27	X	4	69.27	75.44	55.76	61.40
13		3	42.22	43.28	18.57	27.85	28	X	4	56.78	92.33	60.83	61.38
14	X	3	38.53	34.70	22.96	28.80	29	X	2	54.85	62.56	82.50	72.18
15		2	55.42	50.17	15.44	30.72	30	X	2	100.00	100.00	100.00	100.00

Each component was additionally compared to each other to see how strong of a relationship there was between components (Figure 40). As might be anticipated, the articular dispersion and the overall dispersion have the greatest correlation. At roughly 56%, this fair correlation makes sense as the articular dispersion makes up a portion of the overall dispersion. The fracture energy component correlated relatively weakly with articular dispersion at 32.6% and with overall dispersion at 24.7%.

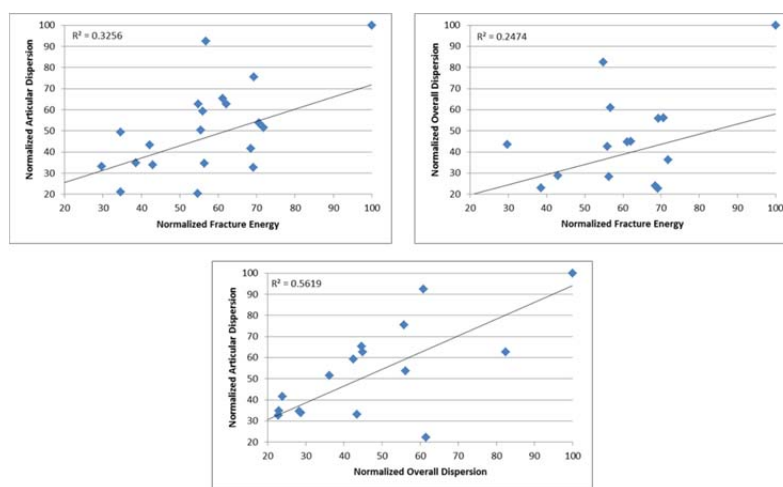


Figure 40: Comparison between expedited severity components' normalized values.

Comparison to Initial Severity Metric

Severity Components

The final goal of the expedited severity metric was to develop a metric capable of predicting PTOA outcome in the joint. While it was developed around the principles used in the full severity metric, it was not intended to provide direct replicas of the full severity metric components. As a result, great correlation between the full severity metric and the expedited severity metric values is not required. However, because the expedited components were developed based on the full metric principles, differences in the values for each component of each metric were further investigated.

The fracture energy surrogate values were created to capture the liberated interfragmentary surface similarly used in the previous work, but not to specifically measure the amount of energy absorbed. As a result, comparing the raw values between these two metrics directly would not strictly be appropriate. However, the normalized data could be compared to see if there was a correlation between these respective data sets. When this was done, there was a very poor correlation between the respective sets of data, only 5.7%. However, two of the data points strongly influenced this lack of correlation. With these problem cases removed the correlation goes up to a significantly better correlation of 42.8% (Figure 41). These points were solely removed from the correlation analysis to view the effects of outliers. The points were maintained in the further analysis of the expedited severity metric.

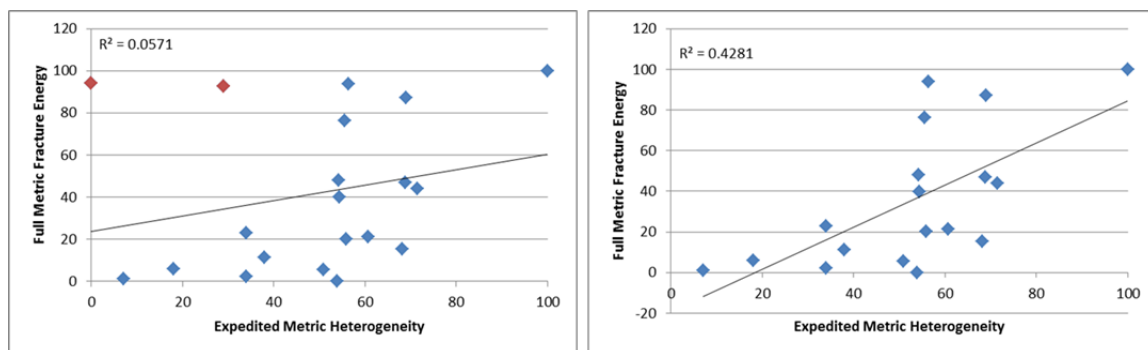


Figure 41: Correlation between expedited and initial severity values for fracture energy (Problem cases in red).

While this is a significant improvement in the correlation, it is still not terribly strong relationship. One reason for the differences in the values could stem from the use of the surrogate intact curve in determining the value. Some information was understandably lost when replacing the actual contralateral intact limb with the surrogate limb in calculating the fracture energy. Additionally, while the semi-automated watershed segmentation method is adequate for GLCM analysis, it is not an accurate segmentation and some bone may not have been properly included in the analysis. One final possibility to explain the differences between the expedited and the initial values for fracture energy may relate to the GLCM analysis. While the GLCM can capture interfragmentary surface area, other relationships within the image may be captured and represented in the final heterogeneity value.

The overall dispersion component of the expedited metric analyzes dispersion similarly to the full severity metric, thus allowing for a direct comparison between values. The dispersion values correlated better between the expedited severity metric and the full severity metric, at almost 60% correlation (Figure 42). While these results were somewhat satisfying, the slope of the line fit for the full metric values versus the expedited metric values was about 0.5. While it would ideal if the slope was closer to 1, it does reaffirm the previous observation that the expedited metric overestimates the full

metric dispersion values by roughly a factor of two. As mentioned, this happens because of an over-estimation of dispersion area in the expedited measure.

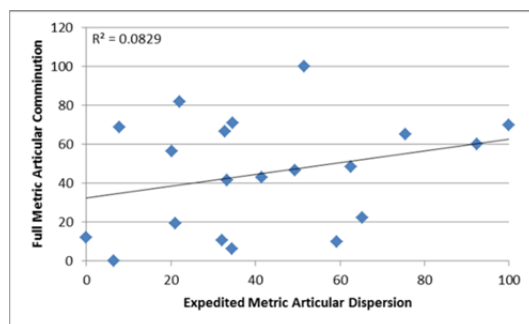


Figure 42: Comparison between expedited and full severity metrics' overall dispersion and displacement values.

Due to the use of dispersion instead of comminution to measure the articular disruption, direct comparison between the articular comminution values of the full severity metric and the articular dispersion values of the expedited metric would be unfitting. Just as with the fracture energy component, however, the correlation between the normalized articular values for each metric could be compared. However, the correlation between the normalized expedited articular dispersion values and the normalized full metric articular comminution values was very poor, at only 8.3% (Figure 43).

The poor correlation between these parameters most likely stems from the fact that the expedited and full metric are not actually measuring the same thing. While both are attempting to measure articular disruption, they are measuring two different aspects of articular disruption. The full metric is measuring the percent difference in interfragmentary surface area between the fractured and intact limb, while the expedited metric is simply measuring the dispersion in the articular region. Another reason for the discrepancy between values is the region of interest for each analysis. The full severity

metric was able to capture the articular disruption in a 3 mm region, while the expedited metric utilized a 9 mm region to capture the disruption. At three times the area analyzed by the full severity metric, the expedited metric values may have been influenced by the area not included in the full metric.

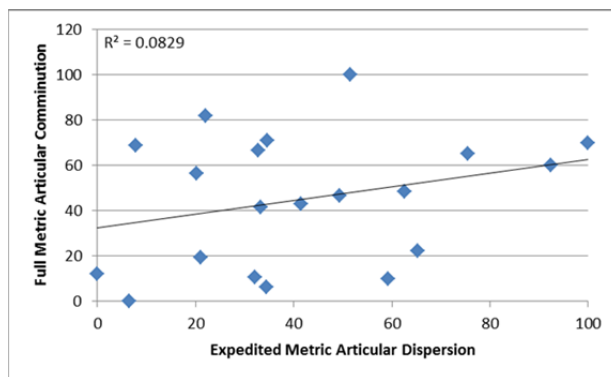


Figure 43: Comparison between the normalized expedited severity metric and the normalized full severity metric articular disruption values.

After combining the normalized components for each metric into their respective optimized severity scores, the correlation between the combined values for the respective groups was calculated. A correlation of 40% was found, showing a fair, but certainly not impressive relationship between the data sets (Figure 44). However, this limited correlation is understandable. The weighting for the expedited severity metric (35% fracture energy, 5% articular dispersion, and 60% overall dispersion) was very different from that for the prior full severity metric (48% fracture energy, 52% articular comminution, and 0% dispersion/displacement). Since these weightings of components are so different, it is not surprising that only a modest correlation was present. Additionally, given that the two components used in the full metric weighting were the two that correlated least with these counterparts in the expedited metric, even a 40% correlation was a somewhat surprising result.

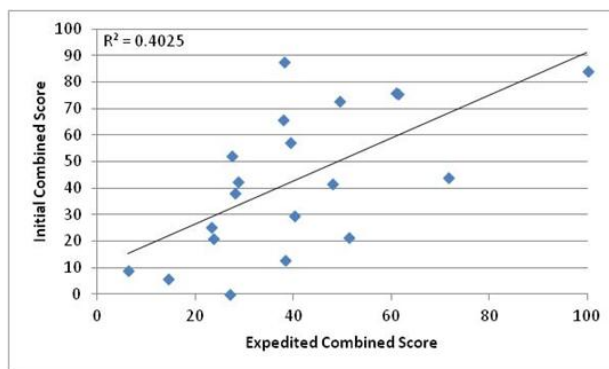


Figure 44: Comparison between combined severity scores for the expedited and full severity metrics (for the original 20 cases).

Concordance with KL scores

The calculated severity scores were compared to KL scores obtained from radiographs at a two year follow-up exam. The radiographs were examined and assigned a score by an experienced orthopaedic surgeon. Due to the categorical nature of the KL scores, a linear regression analysis between the severity scores and the KL scores was not performed. Instead, the statistical analysis used to compare the two values was concordance. Concordance is a sample-based measure that in this context represents the probability that the severity scores for two different fractures can differentiate their KL scores. As an example, if fracture case A were to have a severity score that was less than that of fracture case B, and case A had a KL score of 0, while case B had a worse KL score, the observations would be deemed concordant. As previously mentioned, the concordance values can range from 0 to 1, where 1 represents a perfect differentiation and 0.5 represents a differentiation resulting from chance.

Each component of the expedited fracture severity metric was normalized and then compared to the corresponding KL scores to determine their individual ability to predict the joint outcome. An additional expedited analysis was run on just the 20 cases from the initial severity metric. The results were re-normalized and the combined score

weighting was re-calculated for just the 20 cases. The calculated weighting for just the 20 cases was not very different from what was calculated for all 30 cases. The 20 cases weighting was 35% fracture energy, 5% articular dispersion, and 60% overall dispersion, which was quite similar to the 33%, 6%, and 61% weightings, respectively, for the 30 cases.

The concordance between each component and KL score for all 30 cases was found to be 68.3%, 68.3%, and 68.9% for the fracture energy, articular dispersion, and overall dispersion, respectively (Figure 45). After analyzing just the 20 cases included in the full metric analysis, each component showed an increase in concordance with the KL score. The fracture energy component had a slight improvement in concordance to 69.4%. That is approximately 10% less than the full metric, which realized 79.6% concordance. The concordance between the expedited overall dispersion and the KL score jumped to 72% for the 20 cases. The full severity metric values for this component had 79% concordance, only 7% higher than the expedited metric component. Finally, the concordance calculated between the expedited articular dispersion and the KL score for the 20 cases was 69.4%. This is about 9% less than the full metric, which was able to obtain 78.3% concordance with the KL score.

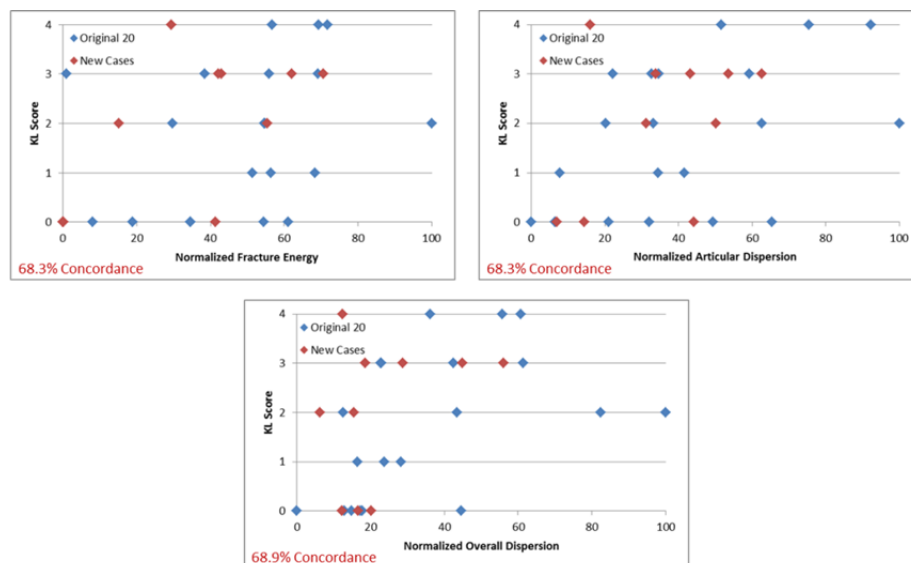


Figure 45: Comparison between normalized expedited severity components and KL scores.

The combined expedited severity metric scores showed a moderate predictive capability, having a 75.2% concordance with the KL scores when all 30 cases were analyzed (Figure 46). When the combined scores for the 20 common cases between the full severity metric and the expedited severity metric were compared to the KL score, a concordance of 79.6% was found. This was roughly 8% lower than the full metric, which had a concordance value of 87.9%.

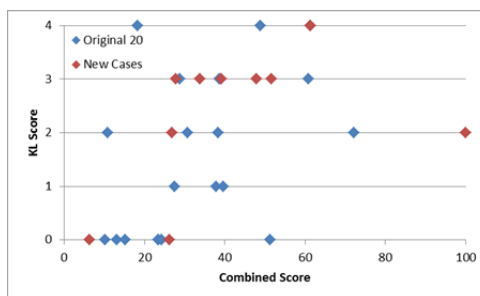


Figure 46: Comparison between the combined severity scores of the expedited metric and the KL scores.

OA Development Comparison

The ability of the expedited severity metric to distinguish differing levels of post-traumatic OA severity, i.e. differentiating KL scores, is important. However, a larger purpose of the metric is to simply be able to predict if PTOA develops at all.

Differentiating between patients that do not develop PTOA (i.e., KL scores of 0 or 1) from those that do (KL score ≥ 2) is a more vital role for the expedited severity metric. As a result, further analyses were done to see how much the expedited severity metric values varied between these groups, in addition to measuring the ability of the metric to predict OA develop.

In addition to the analyses previously mentioned, the group of cases that did not develop PTOA was compared to the group of cases that did. Because no assumptions can be made on the normality of the data distribution, and as previously mentioned, the KL scores are categorical, a Wilcoxon Ranked Sum test was used to test for significant differences between the cases with and without post-traumatic OA. This was done for each component of the expedited metric, in addition to the combined severity score.

The cases that did not develop PTOA differed significantly ($p < 0.05$) from those that did for two of the three components (Figure 47). The most significant difference was in overall dispersion ($p = 0.021$). The differences in articular dispersion were the next most significant ($p = 0.024$). The only component whose values did not significantly differ was fracture energy ($p = 0.079$). While the fracture energy component was not statistically significant, it was close to being so. After the components were combined into a severity score, the resulting scores were additionally compared using the same significance criteria and the same statistical analysis. While comparisons between the two groups were important for each component, the combined severity score differences would prove to be the most important as it is the final outcome of the expedited severity metric. A significant difference was found between the cases in terms of OA development, with a p-value of 0.004 using the Wilcoxon Ranked Sum test (Figure 47).

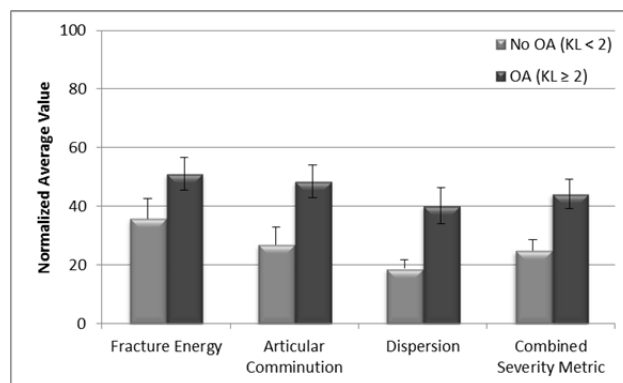


Figure 47: Comparison between the expedited severity values for cases with OA vs. no OA development.

As discussed, further analysis was done to see how the expedited severity metric performed in predicting PTOA development. If a threshold value was set, and a combined severity score was found to be below this threshold, then the expedited metric would predict no PTOA development. However, if the combined score was greater than or equal to the threshold value, then the metric would predict PTOA development. A receiver operating characteristic (ROC) analysis was performed on the expedited severity data to measure this ability.

The ROC analysis varied the severity threshold of the analysis then developed contingency tables for each threshold value (Table 6). The contingency table would contain the number of cases that the PTOA outcome correctly differentiated (true positive (TP) and true negative (TN) values), and the number of cases incorrectly differentiated (false positive (FP) and false negative (FN) values). From each contingency table, statistical rates could be determined measuring the predictive ability of the expedited severity metric at that threshold value.

Table 6: Contingency table for a threshold value of 27.75

		Actual Outcome	
		OA	No OA
Predicted Outcome	OA	(TP) 15	(FP) 3
	No OA	(FN) 3	(TN) 9

The statistical rates utilized in this analysis were the True Positive Rate (TPR), or sensitivity of the metric, and the False Positive Rate (FPR), or specificity of the metric subtracted from one. An ROC curve was generated showing the results for varying threshold values (Figure 48). The ROC curve graphs the TPR versus the FPR where any point at or below the diagonal of the graph (represented as the red dotted line) would represent predictability equivalent to or worse than that resulting from chance. A perfect classification would be represented by a point in the (0, 1) location of the graph. At this point, the metric would have no errors in predicting PTOA outcome. The expedited severity metric showed a good ability to predict PTOA outcome with the best results presented at a threshold value of 27.75 (represented by the green point on the ROC curve).

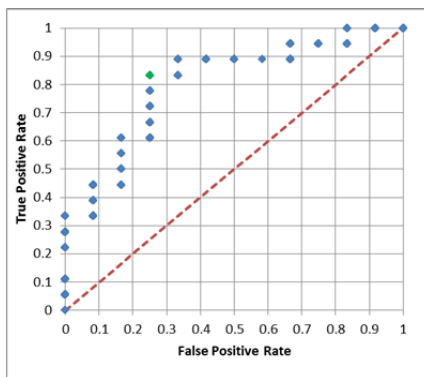


Figure 48: Receiver Operating Characteristic (ROC) curve for varying severity thresholds of the expedited severity metric

Calculation Time

The full severity metric required roughly 8-10 hours, beginning from a CT scan of a fractured ankle, to obtain a severity score for the fracture. One of the main goals in the development of the expedited metric was to substantially reduce this time, ideally from the order of hours down to minutes. Along with reducing the overall calculation time, the secondary goal was to reduce the amount of user intervention required.

The average time for the expedited analysis to develop a severity score was just under 15 minutes (14.9 minutes) for the 30 cases analyzed (14.3 minutes for the 20 initial cases) (Figure 49). This was a dramatic decline from the 8-10 hours required for the full severity metric.

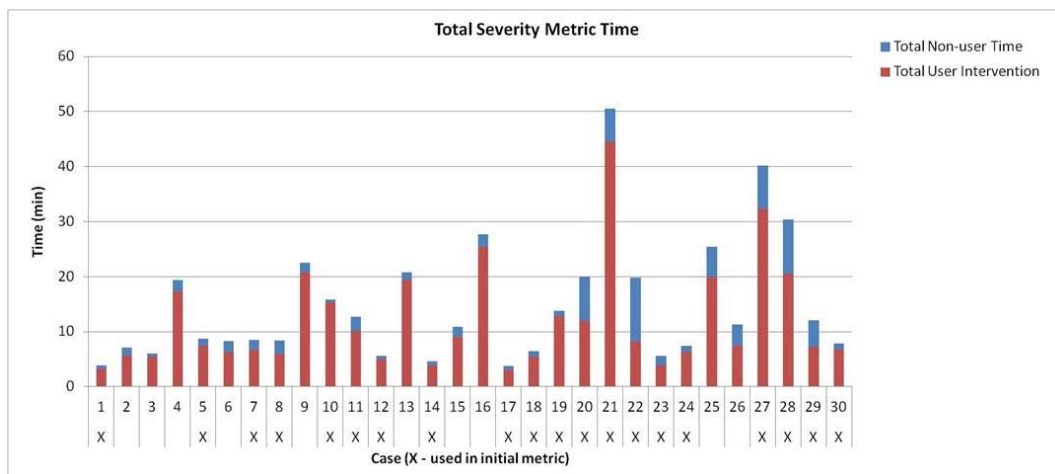


Figure 49: Breakdown of total calculation time for the expedited severity metric.

The amount of user intervention averaged to be roughly 12 min, or 80%, of the total time. The user intervention was broken down into five different steps: Open/Crop Image, Initial Segmentation, Patient Info/Articular Slice, Initial Segmentation Check, and Segmentation Adjustments. Figure 50 shows the variation in total user intervention time along with the amount of time for each step considered user intervention.

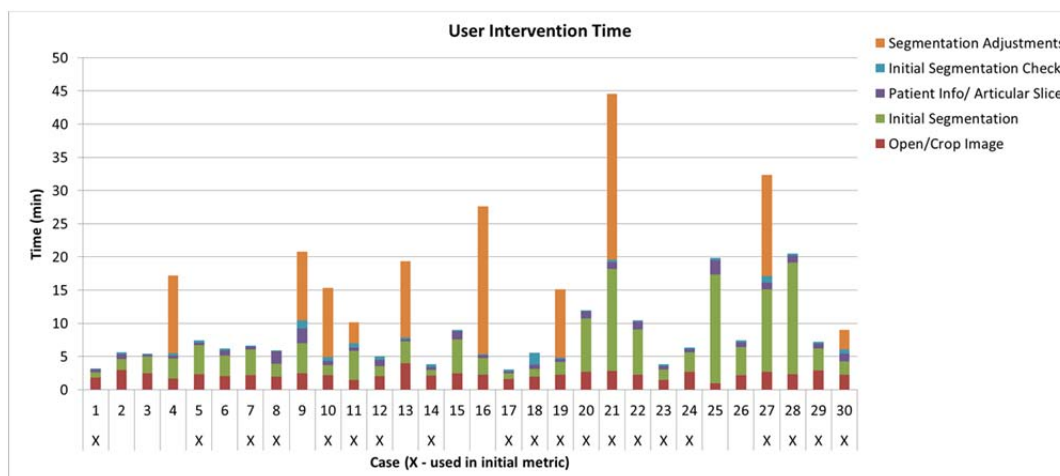


Figure 50: Breakdown of total user intervention time for the expedited severity metric.

Open/Crop Image required the user to open the original DICOM image files and crop the image down to a region of interest (ROI) to include the fractured bone. The average time to open and crop the images was roughly 2 minutes. Next the user performed an initial, rough, watershed segmentation of the tibia, which on average required roughly 4.5 minutes to perform. The Patient Info/Articular Slice step averaged under a minute. This step had the user input patient-specific information such as height, weight, and KL score (if known). The articular slice was also calculated at this time, using the initial segmentation.

The user was then prompted to review the initial segmentation for any excess or missing fragments in an Initial Segmentation Check step. If an error was seen, the user could then choose to re-run the previous analysis starting at either the image cropping or watershed segmentation step, or could manually edit the segmentation. The review step averaged roughly 40 seconds to perform.

If problems were detected, the remaining time to develop an acceptable segmentation was registered in a Segmentation Adjustments step. Occasionally the user will come across a CT image that is extremely difficult to segment. In these cases, manual editing must be done to the segmentation. Of the 30 cases analyzed, 10 required some form of adjustment to the initial segmentation. The time for segmentation adjustments ranged from 3 to 25 minutes, averaging a little over 12 minutes for those 10 cases.

The amount of non-user computation time ranged from half a minute to almost 12 minutes, with an average of roughly 3 minutes. This portion of the code was broken down into two sets of operations. The first of these took the segmentation, applied the anisotropic diffusion filter to the image, and performed the GLCM analysis. The second took the GLCM results and calculated the severity components, along with the combined severity score. Figure 51 shows that essentially all of the non-user time was taken up in

applying the filter and performing the GLCM analysis. The majority of that time was taken up by the filter.

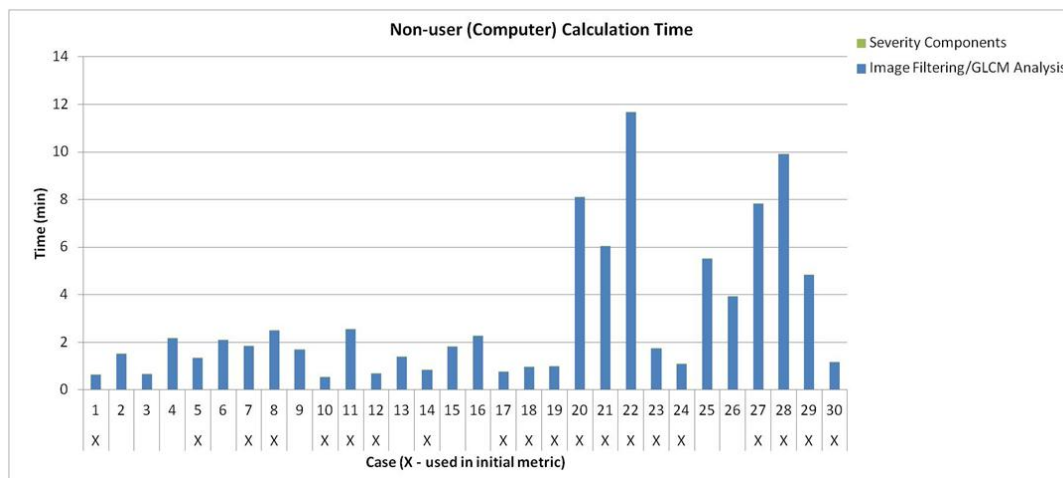


Figure 51: Breakdown of total non-user calculation time for the expedited severity metric.

Overall, the calculation time to obtain a severity score for the expedited severity analysis was greatly improved over the full severity metric. Taking the time from 8 hours to roughly 15 minutes is a major step in developing a metric that could be used clinically. Also, in the process of reducing the calculation time, the decrease of user intervention required would allow many more cases to be analyzed and many more severity scores to be obtained in a given period of time.

CHAPTER FIVE: DISCUSSION

Inter-/Intra-User Variability

Variability Test Setup

One of the intrinsic goals in the process of developing the expedited severity metric was that a novice user, with limited guidance and anatomical knowledge, would be able to consistently produce a severity score similar to that of an experienced knowledgeable user. Differences in the severity results between separate users or between one user's analyses at different times could cause significant decrement of the predictive reliability of the metric. To investigate this, an inter-/intra-user variability test was conducted to determine the variation and reproducibility of the expedited metric.

Because the severity metric is completely automated after the tibia has been segmented and the resulting segmentation approved, the results of the segmentation play a crucial role in determining the severity value. As a result, much of any differences in the severity metric values would most likely stem from differences in the segmentation of the tibia. Consequently, a large portion of the inter-/intra-user variability comparisons needed to focus on differences in the user segmentations.

The inter-/intra-user variability test was designed to include 4 different users, two of whom were very familiar with Matlab, and fairly to very familiar with the expedited severity metric process (Users A and B). The other two users were fairly familiar with Matlab, but were new to the expedited severity metric process (Users C and D). A User's Manual was written to provide consistent guidance (Appendix). This manual was written to easily guide the user, while also reducing variability due to differences in instructions between users. Five different cases were chosen for the inter-/intra-user test. (The nomenclature used was distinct from that for the previous 30 cases discussed). These five comparison cases were chosen to span the range in severity levels, to expose the user to varying steps of the manual, and to vary the amount of user intervention for each case.

Each user ran each case at least once, while User A re-ran the same five cases a second time, approximately two months after the first analysis.

Calculation times for each user were not included in the results of this analysis. While the time it takes to obtain a severity result is important to the utility of the expedited severity metric, that was not a focus of this investigation. This was done so that each user would not feel rushed to complete each case and could take their time to produce quality results. It is assumed that after a short number of cases analyzed, the time required for a novice user to complete the analysis for each case would drop dramatically, approaching that of an experienced user. After some time, the user would ideally not need to read through the manual for every case, but rather would use it solely as a reference for unusual cases.

Segmentation Comparison

Multiple different bases were used to analyze the differences in segmentations between the users. The first such basis was to compare the overall volume of the segmentations over the length of the fracture. This gave a rough estimation of any major differences in the segmentation, and of potential missing fragments between users. The second basis for comparison was the total convex hull volume over the length of the fracture. This measurement was felt to give further insight into potential missing fragments, especially ones that were greatly dispersed.

The final basis for comparison of the segmentation was the Dice Similarity Coefficient (DSC). Dice analysis compares the overlap between two volumes (segmentations in this instance). One volume was set as the “truth” segmentation (volume A). This segmentation was chosen to be User A’s first run. Each other segmentation was then compared to the “truth” segmentation. The DSC value is calculated by dividing the total combined volume by twice the volume common to the

two (Equation 13). A perfect overlap between the segmentations results in a DSC value of 1, while no overlap will result in a value of 0.

Equation 13:
$$DSC = \frac{2(A \cap B)}{A + B}$$

The results of the segmentation comparisons between the different users were very encouraging (Figure 52). The largest percent difference came from Case IV. This difference stemmed from a between-user difference in the first identified fractured slice. This case had a distal first fracture slice starting in the metaphyseal region of the bone, which can make it difficult to determine the first fractured slice. While these differences caused noticeable variations in volume analyzed, they caused only negligible differences in the overall severity values. Results for the convex hull volumes were similar.

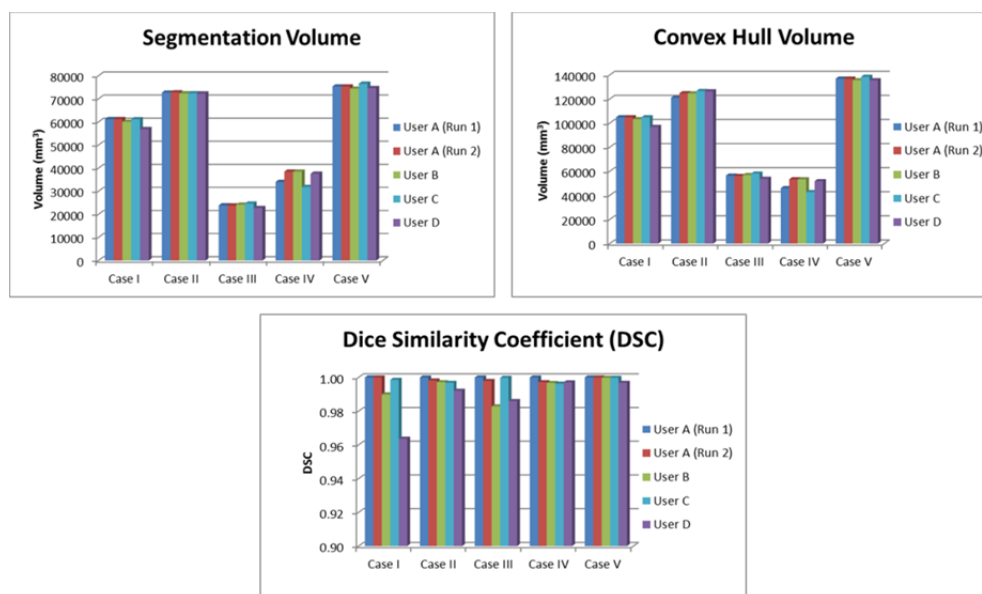


Figure 52: Initial results for the inter/intra user variation between user segmentations.

Results for the DSC showed very good agreement, ranging no lower than a 0.96 comparison to User A's 1st run. However, given the fairly significant difference seen

between this value (User D's Case I analysis) and the other DSC values, further investigation was deemed necessary. Upon investigation, it was found that User D had excessively cropped the image, cutting off portions of the tibia from the analysis (Figure 53).

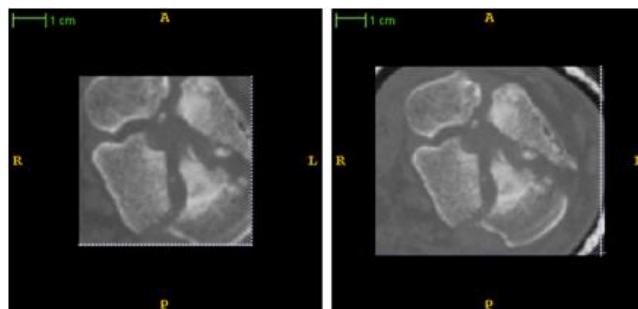


Figure 53: Differences in image cropping for User D's 1st and 2nd runs (1st Run - Left, 2nd Run - Right).

It was found that this error had stemmed from an instruction that was misleading in the cropping step of the user's manual. Additional investigation discovered that improper cropping was present in both Case I and II for User D, with the most severe seen in Case I. The error in the manual was fixed and User D was asked to rerun the expedited analysis for those two cases approximately 2 months after the first analysis. The new analysis resulted in images showing appropriate cropping and also resulted in improved segmentation results. The segmentation volume reduced from 15.6% difference to User A's first run to nearly 0% difference for Case I, and from 9.2% difference to 5.7% difference for Case II. Similar results were also seen for convex hull volumes. The most promising change was seen for the DSC value, which increased from 0.964 to 0.999 for Case I. Case II also showed an improvement in its DSC value, but not nearly as dramatic as Case I (from 0.992 to 0.997). From this point on, User D's second run for Cases I and II will be presented since the first run was proven inaccurate.

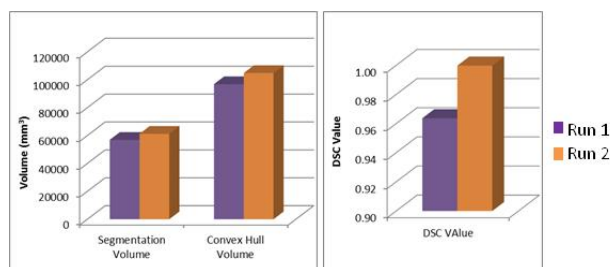


Figure 54: Effect of re-run for User D on segmentation results for Case I.

Articular Slice Comparison

Besides the segmentation, one of the other important factors in determining the severity values is the location of the articular surface. When determining the fracture energy component, it is important that an accurate and consistent articular slice be chosen so that an appropriate registration can be made to the surrogate curve. A significant error in the articular slice location could have significant effects on the resulting value.

Additionally, when determining the articular dispersion component, the articular slice location determines the area analyzed for articular disruption. If this is significantly inaccurate, then the wrong region would be analyzed, and an inaccurate representation of the articular disruption could result.

When the user crops the initial CT image, there may be differences in the region of interest (ROI) in all three directions of cropping. Such cropping differences could result in significantly different articular slice values. While these values might be significantly different, that does not mean that a different articular slice would necessarily be chosen. For example, when observing the results from the inter-/intra-user variability test, the most pronounced differences were observed for Case IV, which had articular slice values ranging from 56 to 135. Even though the numbers of slices were greatly different between users, Figure 55 showed good agreement and precision in calculating a consistent articular slice.

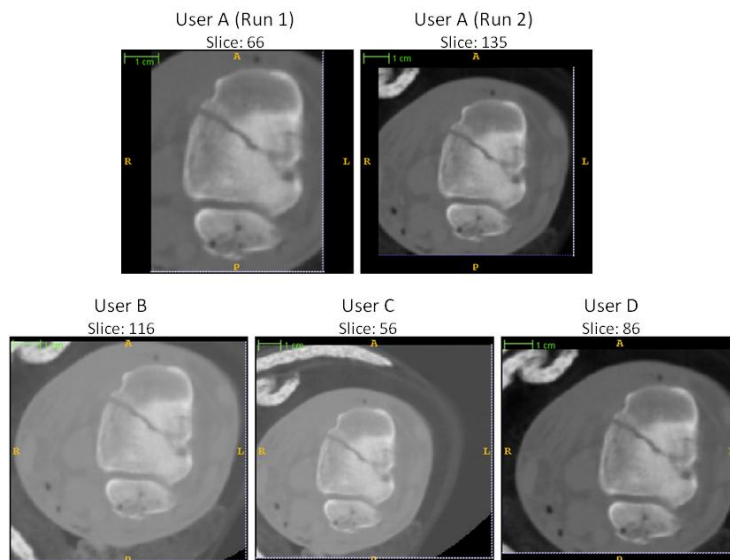


Figure 55: Differences in the articular slice between users for Case IV.

Severity Results Comparison

While the segmentation of the tibia and the location of the articular slice are important factors in determining the fracture severity values, the most important variation to investigate for the inter-/intra-user test was the variation in the severity values themselves. The fracture energy, articular dispersion, overall dispersion, and combined severity values were compared for each user's analysis of each case. The results again showed good agreement between users (Figure 56). As mentioned earlier, even though significant differences could be seen between the users' segmentations for Case 4, the resulting severity values showed almost no difference, with overall dispersion being the only component having any noticeable variation.

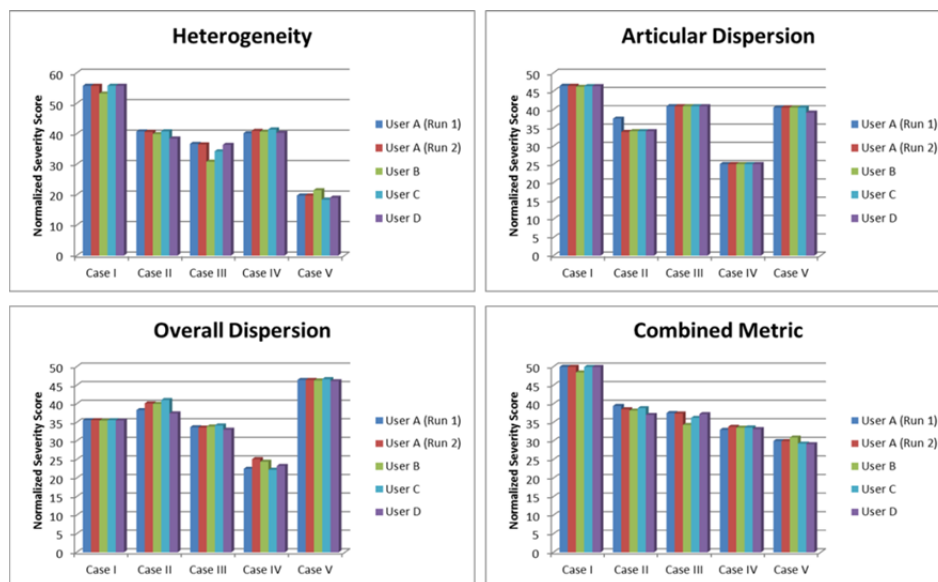


Figure 56: Differences in components and overall fracture severity values between users in the inter-/intra-user variability test.

When comparing the combined values, there was little variation. The greatest difference was an 8% difference between User A and B for Case III. Even so, if the severity values obtained by each user were used to stratify the cases, almost the same order would be obtained by each user (Figure 57). Overall the expedited severity metric showed excellent agreement between users. With the guidance of a user's manual in addition to some presumed anatomical knowledge (tibia, fibula, proximal, distal, etc.) each user was able to produce consistent results regardless of level of experience with the expedited metric code.

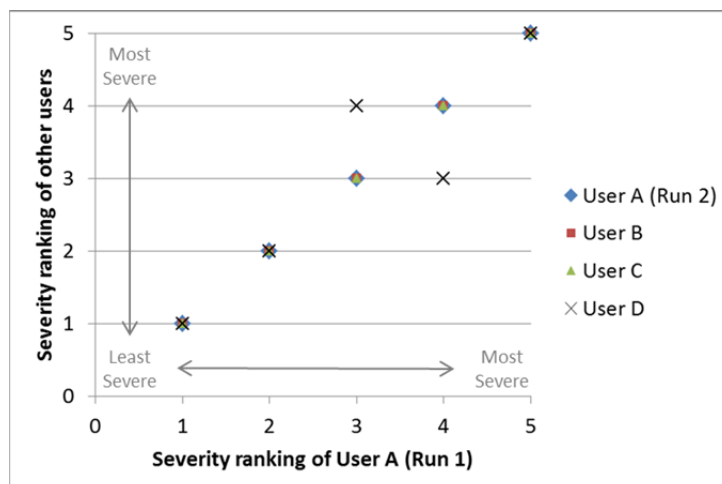


Figure 57: Variation in severity stratification for combined severity scores between users in the inter-/intra-user variability test

Advantages of the Expedited Severity Metric

The expedited fracture severity metric possesses attributes that make it more practical for clinical application than the prior full fracture severity metric. The first, and most significant, is the calculation time required to obtain a severity score. At about 15, minutes this is significantly less time than the 8 hours required for the prior severity metric. The significant reduction in time will allow CT scans to be rapidly analyzed, so that the surgeon can quickly obtain a severity score to assist in treatment decisions.

The second advantage of the expedited metric is its ability to determine a severity score without an accurate segmentation of the bone. The full severity metric required a very accurate segmentation of the tibia to obtain its score. Through the implementation of the convex hull along with the GLCM textural analysis, the expedited metric is capable of performing its analysis with only a rough segmentation. Furthermore, if any errors in the segmentation are found which require manual editing, the expedited metric would be the more ideal metric to use. Because only a rough segmentation is required, the user is not required to meticulously analyze the image for bone edges as is the case

for the full fracture severity metric. Not having to scrutinize the image to as high a degree allows for manual edits to the segmentation to be made faster in the expedited severity metric. The average time to make edits to the 10 cases requiring manual edits was only about 12 minutes for the expedited metric. It is doubtful that the quality of manual edits required for the full severity could be made in as short a time.

The third and final significant advantage of the expedited metric is producing a severity score that reliably predicts PTOA development, without the need of an intact contralateral limb in the CT scan. Through the development of surrogate models for the intact limbs, the expedited metric was able to replace the intact limbs for taring purposes in the metric calculation. This is an important step in developing a clinically applicable expedited metric, because it is very difficult to reliably obtain the contralateral limb in a CT scan. Additionally, without the need for the intact limb, retrospective analyses are possible. This will allow for an increase in patient numbers in the expedited analysis by including past fractures captured without the intact limb in the CT scan volume. An additional retrospective application utilizing the expedited analysis could be to analyze past literature claiming advantages for certain treatments over others.

Future Applications

Clinical Application

Given its good predictive performance and the greatly reduced processing time, clinical application of the fracture severity becomes much more practical with the expedited metric. Surgeons can now have an objective, quantitative representation of the overall severity of the fracture. Because it can be obtained prior to the surgery, there is potential to replace the current subjective classification systems (AO/OTA, Rüedi and Allgöwer). With the expedited metric in place, a surgeon will have an objective numerical score to determine severity of joint insult, to aid in development of an appropriate course of action for reconstruction.

In addition, the expedited metric will assist surgeons in separating damage to the joint from the initial trauma and damage attributable to chronic mechanical factors. Utilizing the expedited metric in this assessment would allow for comparisons to be made between treatment methods. The subjectivity and inconsistency between surgeons in classifying the fractures through traditional classification systems has made it difficult to provide evidence on which method is best for certain fracture severities. This issue is rooted in the inability to appropriately differentiate sources contributing to PTOA development. With the expedited metric allowing this differentiation to be done, further progress and research can be done to more definitively show the advantages and disadvantages of one surgical method over another.

Translation to Other Joints

Currently, the expedited severity metric is only designed to analyze fractures of the tibial plafond. However, the metric does have potential to be applied to other joints which also are subject to PTOA development, such as the knee or the wrist. The ability of the metric to be able to translate to other joints would allow even further usage and applicability in the clinical setting.

The principles behind the full severity metric are based on fracture mechanics of bone, which are universal to any fracture. Because the expedited metric was developed around those same principles, it should be able to be applied to any fracture of bone, at least in theory. In order to do this, CT images of the intact limbs would need to be taken so that a surrogate representation of the intact limb could be developed, just as was done for the ankle in this research. Additionally, patient outcomes would need to be obtained at a follow-up exam so that appropriate model parameters (e.g. weighting factors) could be attained.

Major Extremity Trauma Research Consortium (METRC)

Currently the Major Extremity Trauma Research Consortium, or METRC, is a research collaboration consisting of 23 Core Civilian Trauma Centers, 4 Military Treatment Facilities, and 27 Satellite Centers located throughout the United States. Started in 2009, it receives funding from the Department of Defense to improve the clinical and functional outcomes and quality of life for service members and civilians who have sustained high-energy trauma to the extremities.

While the 30 cases here analyzed is a reasonable number for determining the efficacy of the expedited metric, METRC has the potential to greatly increase the number of cases available for analysis. Utilizing this larger group, numbering into the hundreds, an even stronger decimation of the predictive power of the expedited metric would be possible. Additionally, because the cases are from multiple centers around the country, different treatment methods are likely used to treat the wounds. The 30 cases used for the present series for the expedited metric were mostly treated by external fixation and limited internal fixation. Other institutions may be more inclined to use more extensive internal fixation. Comparing the outcomes for each of the surgical methods for cases of similar severity could shed better light on which surgical methods work best. Also, due to the normalization methods used in calculating the expedited metric, most, if not all, of the CT images available should be able to be analyzed. The only requirement is that the CTs contain the entire length of the fracture. This ability to analyze almost every case presented underscores the potential of the expedited severity metric.

Limitations

The expedited metric does have its limitations. The greatest of these is its potential to become obsolete. The full severity metric would be preferable for clinical analysis if it were not for its large calculation time, since it provides a greater ability to predict PTOA outcome. As previously mentioned, a significant portion of the calculation

time for the full severity metric is consumed in making adjustments to provide an accurate segmentation of a bone and its fragments. With advancements in computer and imaging technology, the time and amount of user intervention required to obtain these segmentations will likely be reduced to the point where it would be feasible to use the full severity metric instead of the expedited metric. While some segmentation methods currently exist and appear to be effective in their initial stages [57], they have not been thoroughly investigated in their true ability to consistently and easily obtain accurate segmentations. Pending such improvements to the full metric, however, the expedited metric is a useful tool.

An important consideration when reviewing the results of the expedited metric is that perfect 100% concordance with KL is not necessarily to be expected in the results. Because chronic mechanical factors also influence the outcome of the joint, as indicated through the literature, expecting 100% concordance would be unrealistic. As a result, it is actually promising that 100% concordance is not achieved in the results.

Another limitation of the expedited metric is the number of cases analyzed. As previously discussed, 30 cases are sufficient for the preliminary analysis of the metric to determine its merit. However, adding more cases would further validate the statistical significance and predictability of the metric and provide more relevance to the concordance values. With the addition of more cases at the University of Iowa Hospitals and Clinics through the same NIH grant funding this research, and the addition of cases from the METRC study, further knowledge of the efficacy of the metric can be determined.

Another important limitation of the expedited severity metric is the abstraction of the theory behind the metric. Utilizing the GLCM to measure the heterogeneity, or disruption, of the CT image texture, and then converting that value into a severity score is a very abstract process to follow and understand. While the idea of capturing the disruption of the fracture may be comprehensible, in-depth details of the expedited

severity metric process may lead to hesitation to fully accept the results, posing issues for routine clinical use and implementation.

In addition to the above limitations, there is room for improvement in the ability of the metric to identify an accurate first fractured slice. While the current method is sufficient for most fractures, it can miss fracture lines that extend proximally through the tibia but that have little displacement or dispersion. Inaccuracies are additionally found when the fracture includes the metaphyseal region of the bone, since the cancellous structures compromise accurate recognition of fractured fragments. Because this bears upon determination of the length of the fracture, improvements in accuracy of fragment identification would certainly make the metric more robust, and thus improve its ability to predict PTOA development.

The final limitation of the expedited metric is the surrogate model curve used for the fracture energy. While the curve shows a good relationship between cases, further adjustments could possibly be done. Other relationships and better filtering techniques could help to improve the relationships further, allowing for a more accurate representation of the energy. Additionally, other forms of curves could be fitted to the data for normalization. Bilinear curve fitting was chosen due to its simplicity: it produced fracture energy values capable of predicting PTOA outcome, a reasonable basis for its use for present purposes.

CHAPTER 6: CONCLUSION

The ability to reliably assess the severity of articular fractures is a crucial part of managing their treatment. The prevention of post-traumatic osteoarthritis is one of the primary goals for a surgeon dealing with articular fractures. Being able to predict which surgical method is most likely to provide the best outcome for the patient is an important issue in this regard. However, current classification methods are highly subjective and inconsistent. An assessment method is needed that would enable distinguishing the relative influence of damage from the initial trauma versus chronic stress aberrations following surgery. The present lack of ability to discriminate between these critical factors in clinical care has inhibited major treatment advancements, and it is this need that led previous investigators to develop an objective CT-based fracture severity metric.

The prior introduction of a comprehensive assessment methodology provided a reliable and valuable measure of severity for fractures of the tibial plafond. This metric used the principles of fracture mechanics to relate the interfragmentary surface area of a fractured bone to the amount of energy absorbed by the bone during the trauma. Adding in measures of articular comminution, along with the displacement and dispersion of tibial fragments, further refined the predictive power of the severity metric. However, the amount of time and resources required to obtain this comprehensive fracture severity metric made its clinical use impractical. For this reason, an expedited fracture severity assessment methodology has been developed which is more suitable for clinical use.

The expedited metric discussed in this thesis presents a solution to the issues limiting the usefulness of the full fracture severity metric. In a relatively short amount of time (~15 minutes), the expedited methodology is able to take a CT scan of a fractured tibial plafond and produce a severity score capable of predicting the development of PTOA in that joint. The work discussed here also has provided a severity score that may be obtained without the inclusion of the intact contralateral limb in the CT scan. Through

the use of edge-preserving image filters, along with other anthropometric normalization methods, a surrogate representation of the intact limb was developed and utilized in the expedited analysis. This expedited metric will ideally aid in the development of surgical treatments designed to improve the quality of life of the patient after such a severe trauma. Clinical studies involving a much larger number of fracture patients, and incorporating this assessment methodology, will need to be completed in order further establish the value of this approach. With further refinement and development of the severity metric, the methodology could be applied to other joints susceptible to PTOA development, further advancing the benefits of the expedited metric in the clinical setting.

APPENDIX: EXPEDITED FRACTURE SEVERITY ANALYSIS: USER MANUAL

Written by: Tony Kilburg

Last Updated: 12/1/11

Table of Contents

1) Set Up Initial Paths for Destination Folders.	94
2) Run the First Section of the Code	94
a) <i>Crop the CT image</i>	94
b) <i>Watershed Segmentation of Tibia</i>	99
i) Rotate Image	99
ii) Choose Cortical Value	100
iii) Excess Fragment Removal	101
c) <i>Input Patient Information</i>	103
d) <i>Segmentation Check</i>	103
3) Manually Edit Segmentations (if necessary)	106
a) <i>Open ITK-Snap Program</i>	106
b) <i>Open CT NifTi image</i>	106
c) <i>Open Segmentation of Tibia</i>	107
d) <i>Load Volume Rendering of Tibia</i>	107
e) <i>Setup for Tibia Adjustments</i>	108
f) <i>Make Necessary Adjustments to the Tibia Label.</i>	108
g) <i>Save the Adjusted Segmentation</i>	108
4) Run the Second Section of Code.....	109
a) <i>Input Approximations for Manual Edits</i>	109
b) <i>Segmentation Final Check</i>	109
5) Run the Third Section of Code	109
6) Run the Fourth Section of Code (optional)	109

Acknowledgements

I would like to thank Andrew Kern, Erin Main, and Noelle Klocke for their assistance in the development and editing of this manual.

Introductory Comments

When running the code, if an error occurs and the program ends before completing the analysis simply return to the editor window, select the section of code, and rerun the program (CONTROL + RETURN). If the program fails again, delete the patient's file causing problems and rerun the program.

Instructions for the process will be in black text. **Important notes will be in red text.** **Additional guidance for a certain step will be in blue text.**

Items Needed to Obtain a Severity Score:

- DICOM images or a NifTi image of the fractured limb
- Patient's height and weight
- KL score (necessary for concordance and/or p-value scores, but not severity score)

1) Set Up Initial Paths for Destination Folders.

Be sure that each of these folders exists before the analysis is run.

- a) dicom_folder: Folder containing ALL the dicom images wanted for analysis.
- b) cases_folder: Folder where patient's files are stored during the initial process of the analysis.
- c) positive_results_folder: Folder where cases that have a satisfactory tibia segmentation are stored.
- d) negative_results_folder: Folder where cases that DO NOT have a satisfactory segmentation are stored.
- e) Surrogate_data_folder: Folder containing the data containing the intact surrogate information and normalization parameters.

2) Run the First Section of the Code

Steps a) through f) will be repeated for each individual patient. Some steps may not be necessary if they have already been previously completed. To run a section of code, click the section (section should become highlighted in yellow), and press CONTROL+RETURN.

a) Crop the CT image

- i) Crop on Proximal End: Choose the proximal most slice containing fractured tibia in the image.

Try to leave about 10-20 slices between the chosen slice and the first slice showing evidence of fracture. If the first slice containing a fractured fragment cannot be determined, choosing slice number 1 is the safest option so as to not cut off any part of the fracture.

- (1) Two figures will appear on the screen (Figure 1) *(it takes some processing time before the figure appears)*. If the desired slice number is known, click "Choose Value". If you would like to change the range of the images, click "Change Range."

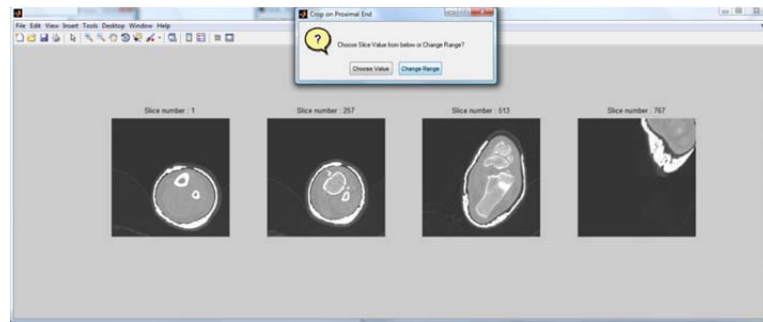


Figure 1: Initial Images for Proximal/Distal CT Cropping

- (a) Choose Value – Enter the desired slice number. (Figure 2)
- (b) Change Range – Enter the lower and upper desired slice values (Figure 3).

Repeat this until the desired slice number is known, then click “Choose Value” and follow “(a) Choose Value” above.

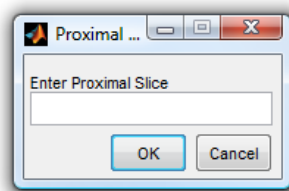


Figure 2: Choose Value Prompt

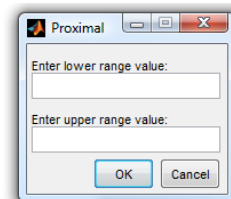


Figure 3: Change Range Prompt

Proximal Slice Guidance

A step-by-step guidance through the proximal portion of the cropping process will be explained here. If guidance is not necessary, proceed to “Distal Slice Guidance” on page 95.

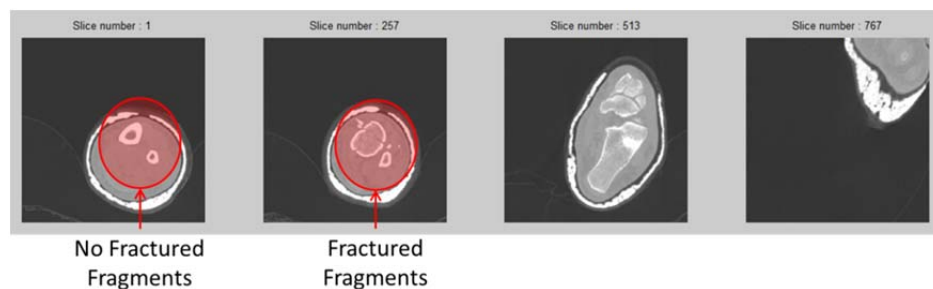


Figure 4: Initial Cropping Images (Proximal Crop)

Here, no noticeable fragment is seen in slice 1; however slice 257 does have fractured fragments. Due to the large difference between these two numbers, choosing “Change Range” would be an appropriate choice. 1 would be the suggested value for the lower range value while 257 would be the suggested value for the higher range value since we know the first fractured slice must lie somewhere between those.

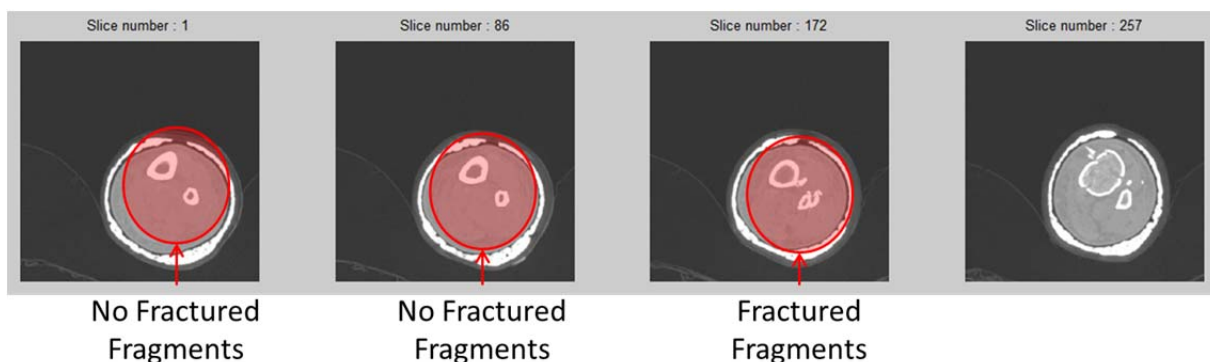


Figure 5: Cropping Images after Changing the Range (Proximal Crop)

Here slices 1 and 86 do not have fractured fragments while slices 172 and 257 do. We now know the first fractured slice lies between 86 and 172. This is still a large difference between slices so “Change Range” would again be an appropriate choice where 86 and 172 are chosen as the lower and upper range values respectively. This process was repeated until Figure 6 below was obtained.

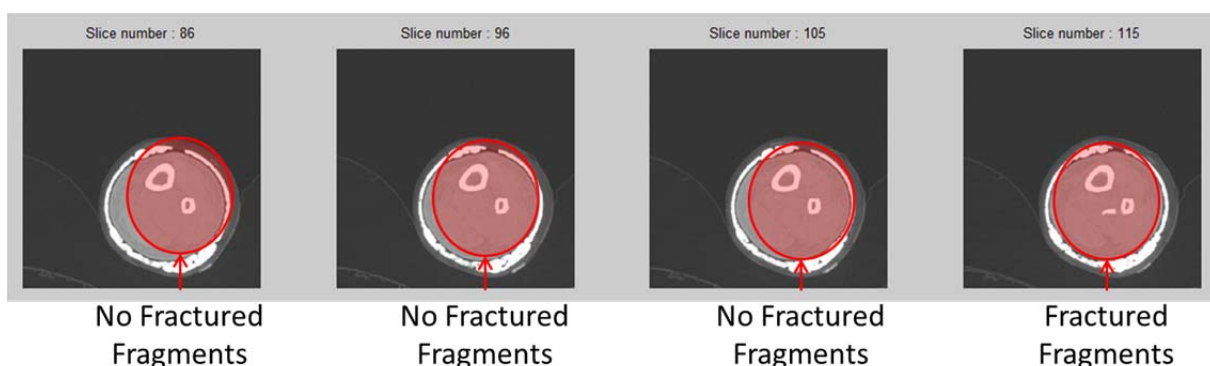


Figure 6: Final Cropping Images (Proximal Crop)

Here slices 86, 96, and 105 all show no fractured fragments while slice 115 shows a fractured fragment. Slice 105 and 115 are a small enough range to make a first slice decision, so selecting “Choose Value” would be appropriate. Given that we want a cushion between our chosen slice and the actual first slice, a value of 100 would be an appropriate value given that we know the first fractured slice lies between slices 105 and 115.

- ii) Crop on Distal End: Choose the distal most slice of the image containing tibia.

Try to leave about 10-20 slices between the chosen slice and the last slice containing the distal most section of the tibia.

- (1) Follow the steps outlined in “(1) Two figures will appear...” of the previous section

Distal Slice Guidance

A step-by-step guidance through the distal portion of the cropping process will be explained here. *If guidance is not necessary, proceed to “iii) Crop the boundaries of the image” on page 97.*

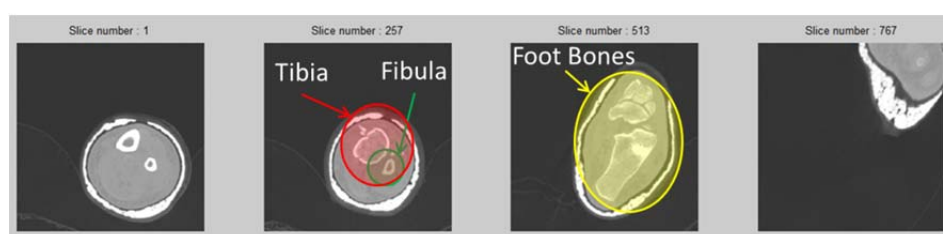


Figure 7: Initial Cropping Images (Distal Crop)

The purpose of this step is to identify the last slice of the tibia. In order to do that it is important to identify and track the bones through the process. The initial image usually will have an image containing the tibia and fibula and then one containing foot bones.

Change the range to these two slices (257 lower and 513 upper).

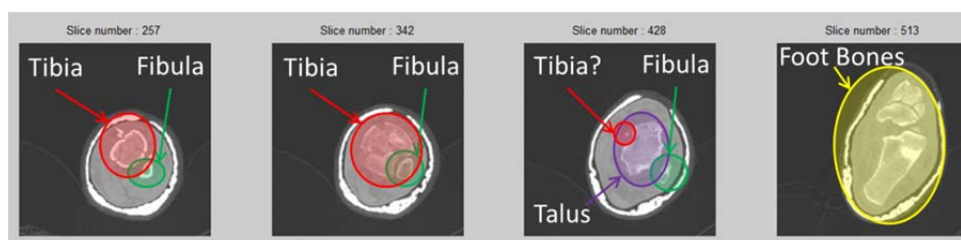


Figure 8: Images after Initially Changing the Range (Distal Crop)

In the adjusted images, start with the proximal slice and track the tibia as the slices move distally. As you can see in the 428 slice, there exist the talus, fibula, and what looks like a small portion of the medial malleolus of the tibia. The medial malleolus is generally the most distal portion of the tibia and is the structure to be looking for in the distal segments. It is important to notice the location of the fibula in the picture because the distal portion of the fibula can occasionally be mistaken for the medial malleolus of the tibia. Its location is important because the malleolus is typically located on the opposite side of the fibula. In this case, because of the uncertainty if the small fragment in slice 428 is tibia, extending choosing a value larger than that would be advantageous. However, extending it all the way to 513 would be a bit extreme. In these cases a slight extension to ensure the fragment will be gone would be appropriate. Possible chosen values for changing the range could be 342 for the lower value and 450 for the upper value.

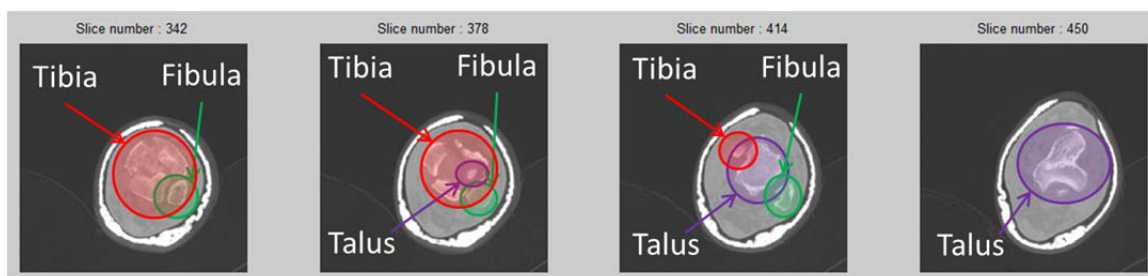


Figure 9: Images after a Secondary Changing of the Range(Proximal Crop)

Again, starting from the proximal slice, track the tibia while moving distally through the slices. You can see the initial portion of the talus appear while the tibia beginning to disappear in slice 378. In slice 414, the talus is easily seen while a small portion of the tibia appears to be remaining. It is difficult at times to truly follow the regression of the tibia as you move through the articular region of the tibia. In these instances, it is helpful to change the range to a smaller region to track this regression. This was done by changing the range to 378 for the lower value and 450 for the upper value.

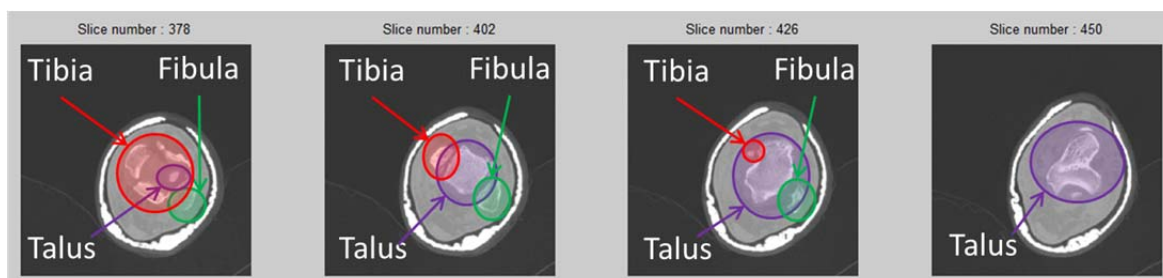


Figure 10: Images with a More Concentrated View of Tibial Regression

Tracking the tibia through these images is a bit easier with the tighter range. You can see a small portion of the medial malleolus of the tibia in slice 426 as suspected earlier. It is now known that the most distal portion of the tibia lies between slice 426 and 450. This range is slightly too large, so changing the range to these values would be necessary.

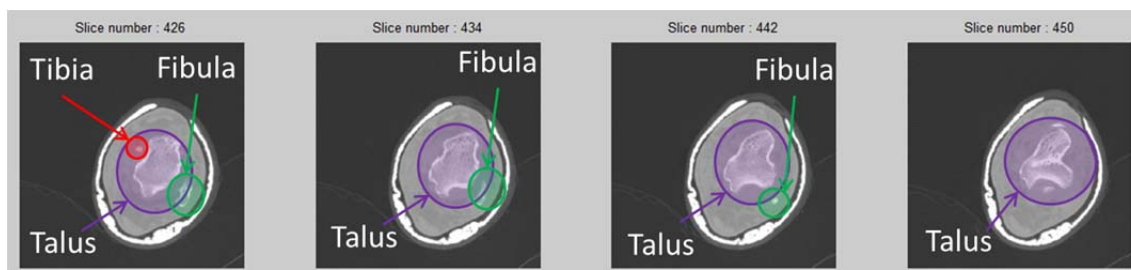


Figure 11: Final Cropping Images

As mentioned previously, you can see a small fragment of the tibia in slice 426, but that fragment is gone in slice 434. With the smaller range between the numbers it would be an appropriate time to choose a value. As with the proximal slice, some cushion between the actual slice and the chosen slice is necessary. As a result, an appropriate chosen slice value would be 440.

iii) Crop the boundaries of the image

Try to locate the outer most boundaries of the bone while choosing points for this step. Only a rough approximation is required so an exact location is not necessary. Use the crosshairs to determine the location for cropping. Only one click for each direction of cropping. (Approximate bone boundaries are shown in the yellow dotted lines in Figure 12)

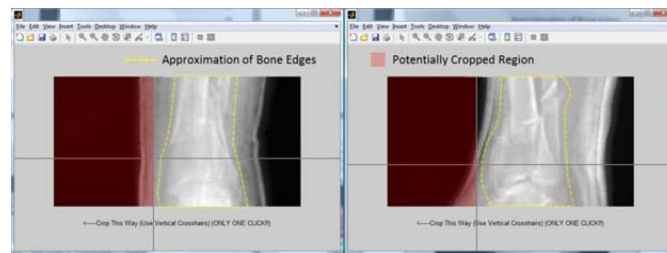


Figure 12: Frontal and Sagittal Plane Cropping

- (1) Crop the images in the frontal plane
 - (a) Figures like those shown in Figure 12 above will appear.
 - (b) Select the point to crop the left side of the image.
 - (c) Select the point to crop the right side of the image.
- (2) Crop the images in the sagittal plane.
 - (a) Repeat the same steps done for the frontal plane above.

b) Watershed Segmentation of Tibia

i) Rotate Image

The goal of this step is to rotate the image so that as much of the tibia, fibula, and talus can be seen.

- (1) Figure 13 will appear *(it takes some processing time before the figure appears)*. If rotation is necessary, click “Yes” to rotate the images to the best position where the tibia, fibula, talus, and fractured fragments can best be differentiated (example shown in Figure 14). Once the position has been found, click “No.”

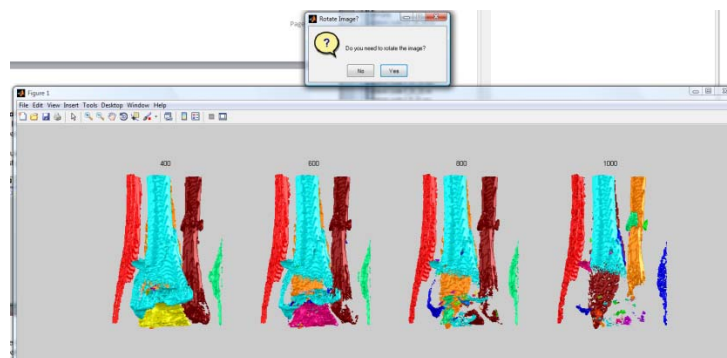


Figure 13: Rotate Image Figures

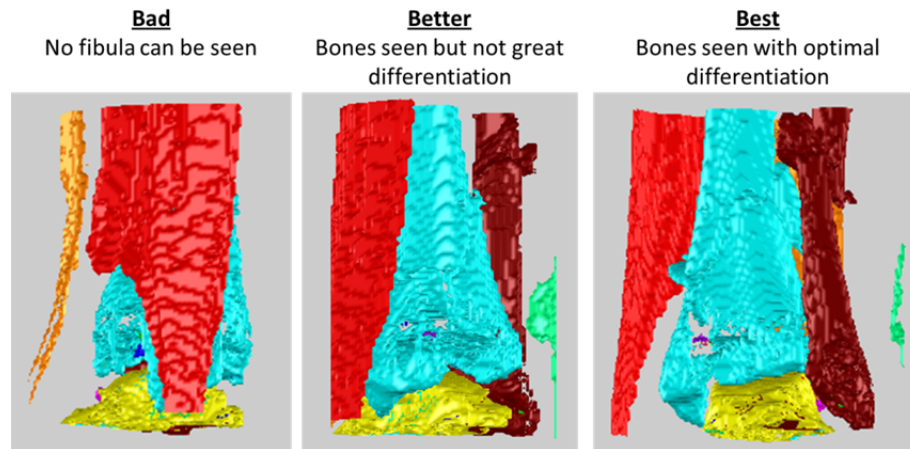


Figure 14: Example of Best Rotational Position

ii) Choose Cortical Value

The goal of this step is to choose the smallest cortical value that will differentiate the tibia, fibula, and talus from each other. Multiples of 25 are the smallest increments necessary.

Suggested minimum value: 300 Suggested maximum value: 1000

(Be sure no tibia fragment is attached to the fibula and vice versa)

(1) Figure 15a will appear. If the desired cortical value is known, click “Choose Value”. Otherwise, click “Change Range” and Figure 15b will appear. Change the ranges until the desired cortical value is determined and then click “Choose Value.” Figure 15c will appear to input the desired cortical value.

(Note: The rotate image prompt will become available after each change to the cortical value range. Refer to instructions “i) Rotate Image” above for details if necessary)

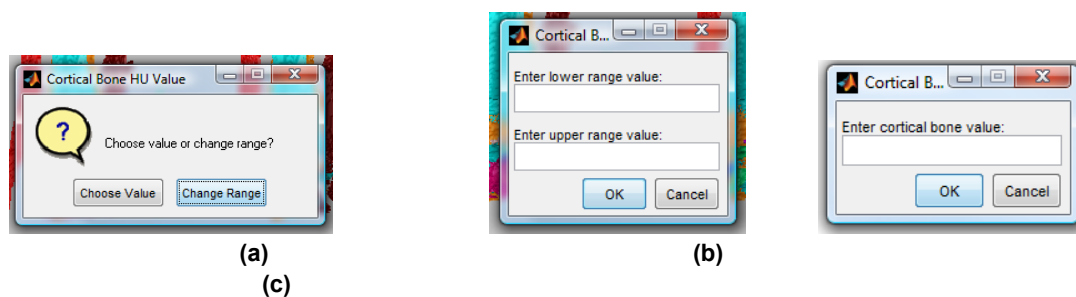


Figure 15: Cortical Value Figures. (a) Initial Prompt (b) “Change Range” Prompt (c) “Choose Value” Prompt

iii) Excess Fragment Removal

The goal of this step is to remove any fragments that are not part of the tibia.

(1) Figure 16 will appear (*it takes some processing time before the figure appears*). Review the volume for fragments that are not part of the tibia then press the **SPACEBAR**. Figure 17 will then appear. *If Figure 17 does not appear shortly after pressing the SPACEBAR, select the Command Window in MATLAB and press the SPACEBAR in this location.*

(a) If any tibia fragment is far from the main volume of tibia OR any fragment that is not tibia is close to the main volume, click “Yes” in Figure 17.

If every fragment of the tibia is close to the main volume AND every fragment that is not tibia is far from the main volume, click “No” in Figure 17.

If there is any uncertainty, click “Yes.”

(A fragment is considered far from the main volume if there is significant spacing seen between the fragment and the main volume)

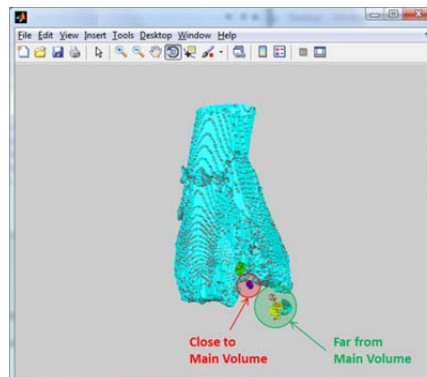


Figure 16: Volume Rendering of Tibia Fragments

(2) If “No” was chosen, skip ahead to “c) *Input Patient Information*” on page 101 for instructions.

If “Yes” was chosen, a figure just like Figure 16 will appear. See instructions (a) – (d) below. *From here on out anything that appears in Figure 16 is considered part of the tibia. Anything that is not tibia needs to be manually removed.*

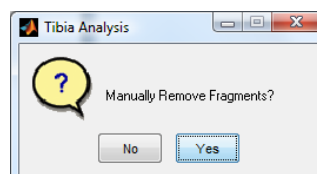


Figure 17: Disconnected Fragments Figure

- (a) Remove the desired fragments (selected one at a time).
(Repeat steps (i) – (iv) until all excess fragments have been removed)

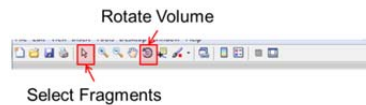


Figure 18: Toolbar for Fragment Removal

See Figure 18 for which tools to use for rotating the volume and selecting the fragments.

- (i) Click in the general working area of the figure to allow the toolbar to become active.
- (ii) Rotate the volume to a position where the desired fragment can be seen
- (iii) Select the fragment
- (iv) Press the SPACEBAR. *(Any other key will erase the fragment from view but will not actually erase it from the tibia segmentation)*

(NOTE: If you accidentally erase the main volume, return to the command window in MATLAB, press CONTROL + C to terminate the program, return to the editor window and restart the code)

- (b) After the final fragment has been removed the figure will reappear. Press the SPACEBAR to conclude the fragment removal.

(NOTE: The toolbar must be inactive at this step. If the toolbar is active and no fragment is to be removed, select the background of the figure and press the SPACEBAR to reload the image. If the background is not selected, it is possible that the main volume was selected while rotating the volume and that pressing the spacebar without selecting the background first will delete the main volume)

- (c) Figure 19 will appear. Click “Yes” if every desired fragment has been removed. If a fragment was missed or this step was prematurely encountered, click “No.”

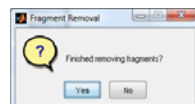


Figure 19: Post Fragment Removal Prompt



Figure 20: Segmentation Completion Prompt

- (d) Figure 16 will reappear for inspection of the volume for any remaining excess fragments. After inspecting the volume, press the SPACEBAR. Figure 20 above will appear. If any additional

fragments can be removed via this step exist, click “Yes” and repeat instructions (a) – (c) until all excess fragments are removed. If the segmentation is correct, click “No.”

(NOTE: If there are any disconnected tibia fragments, it is most likely that they will still remain separate from the main volume. This is fine; the goal is to simply fuse as many fragments as possible together.)

c) **Input Patient Information**

- i) Figure 21 will appear asking for the patient information *(it takes some processing time before the figure appears)*. Input the patient’s height, weight, and their KL score (if available) into the appropriate sections. Once completed click “OK.”

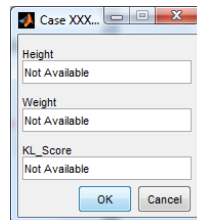


Figure 21: Patient Information Prompt

d) **Segmentation Check**

- i) Figure 22 will appear for inspection of the segmentation results *(it may take some processing time before the figure appears)*.

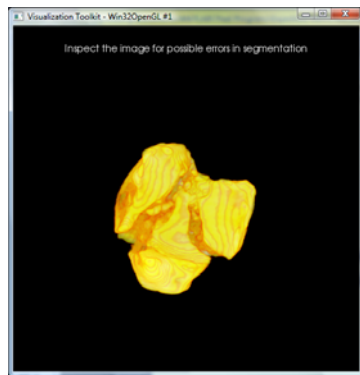


Figure 22: Segmentation Results Check



Figure 23: Examples of Possible Segmentation Errors

- ii) Inspect the image for possible errors in segmentation.

Possible errors (Figure 23) are excess fragments from the fibula or talus being included in the segmentation or a fragment of the tibia missing from the segmentation. Also be aware that the epiphysis of the tibia can appear thin. Be careful not to confuse this with a missing tibial fragment.

- iii) Once inspection is completed, close out the window. Figure 24 will appear. If no errors have been found, click “Yes” and return to “a) Crop the CT Image” to begin the next patient. If errors have been found, click “No” and see further instructions below.

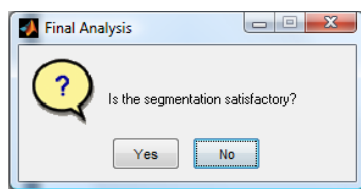


Figure 24: Satisfactory Segmentation Prompt

- (1) Figure 25 will appear. If you feel the segmentation could be fixed by recropping the image and/or resegmenting the tibia, click “Rerun Segmentation.” If you feel the error requires manually editing the segmentation, click “Manually Edit Segmentation.” *See the appropriate section below for further instructions.*

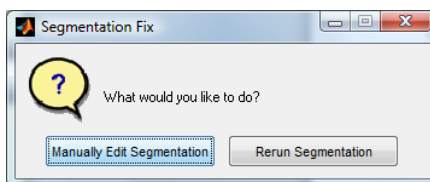


Figure 25: Method of Segmentation Fix Prompt

“Rerun Segmentation” Process:

- (a) Figure 26 will appear. If you feel that the error in segmentation occurred in the Watershed Segmentation step, click “Watershed Segmentation.” However, if you feel that the error occurred while cropping the CT image, click “Opening/Cropping Image.”

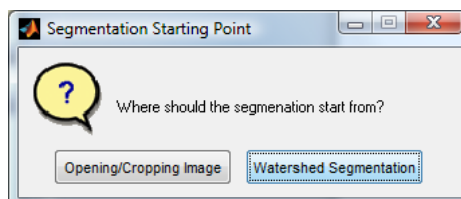


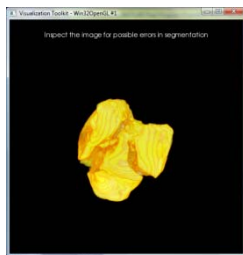
Figure 26: Rerun Segmentation Starting Point

Cases chosen to be rerun will automatically begin at the specified location.

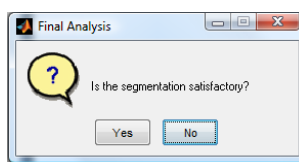
- (b) For cases restarting at the “Opening/Cropping Image” location, refer back to section “a) Crop the CT image” on page 92 and continue through “b) Watershed Segmentation of Tibia” for instructions.
- (c) For cases restarting at the “Watershed Segmentation” location, refer back to section “b) Watershed Segmentation of Tibia” on page 97 and complete that section for instructions.

(d) Segmentation Secondary Check

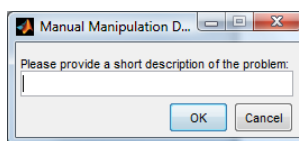
- (i) Figure 27 will appear for inspection of the segmentation results.

**Figure 27: Segmentation Results Check**

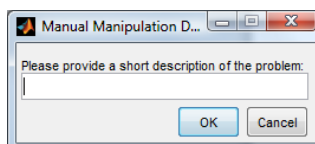
- (ii) Inspect the image for possible errors in segmentation.
- (iii) Once inspection is completed, close the window. Figure 28 will appear. If no errors have been found, click “Yes”. If errors have been found, click “No” and see instructions below.

**Figure 28: Satisfactory Segmentation Prompt**

- Each case that fails its rerun will automatically be subject to manual editing. As a result, Figure 29 will appear. Provide a short description of the error to aid the user in the manual edit procedure.

**Figure 29: Manual Edit Description****“Manually Edit Segmentation” Process:**

- (i) Figure 30 will appear. Provide a description to aid the user for manual editing.

**Figure 30: Manual Edit Description**

Return to step “a) Crop the CT Image” unless all patients have been run.

3) Manually Edit Segmentations (if necessary)

(If no manual edits are necessary, continue to “5) Run the Third Section of Code” on page 107 for the next instructions)

(Repeat steps for each patient)

a) Open ITK-Snap Program

- i) Open the Start Menu and look for the ITK-Snap Icon (Figure 31). Open the ITK-Snap Program.
- ii) After the program opens, Figure 32 should be seen.

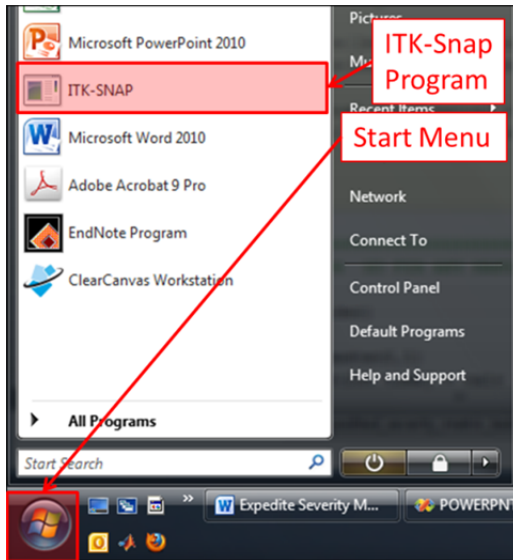


Figure 31: ITK-Snap Icon and Start Menu Location

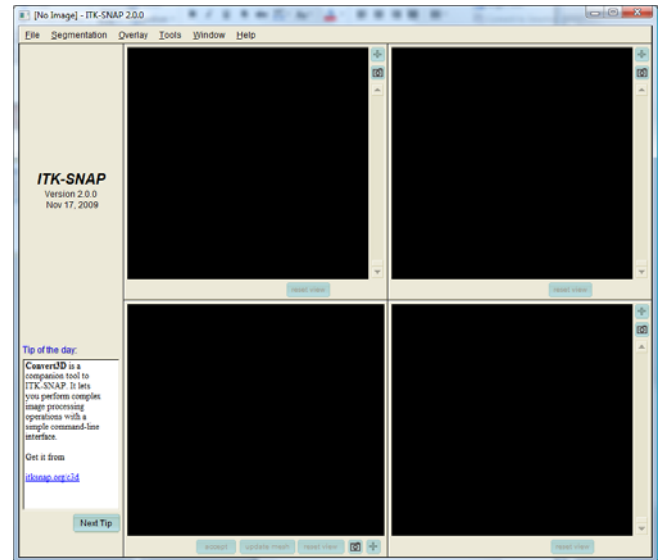


Figure 32: ITK-Snap Program

b) Open CT NifTi image

- i) Proceed to “File” then “Open Greyscale Image.”
- ii) Figure 33 should appear. Select “Browse...” and navigate to the location specified through the negative_results_folder variable.

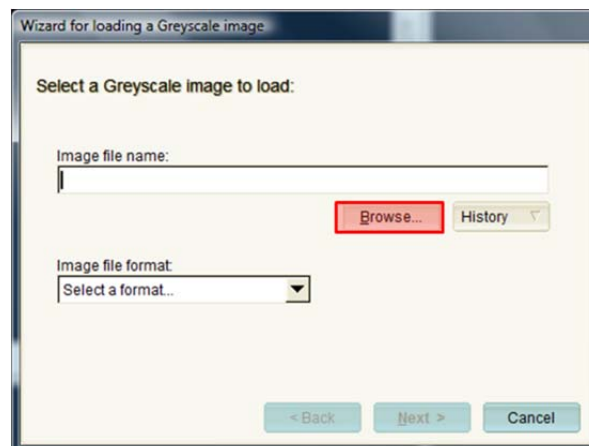


Figure 33: Open Greyscale Image Prompt

- iii) Open the patient's CT NifTi image.
 - (1) Open the Patient's Folder -> Fracture NifTi -> Fracture ROI
- iv) Select the "Next" option from Figure 33. Figure 34 should then appear. Select "Finish" to open the NifTi image. The CT image should then be loaded in ITK-Snap.

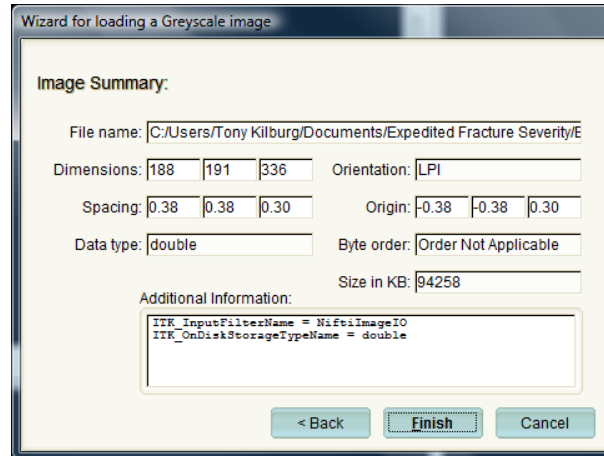


Figure 34: ITK Image Summary Prompt

c) Open Segmentation of Tibia

- i) Proceed to "Segmentation" then "Load From Image..." Figure 33 should appear. Select "Browse..."
- ii) Navigate to the previously mentioned Fracture NifTi folder.
- iii) Open Fracture_Tibia. Select "Next" and then "Finish" to load the segmentation.

d) Load Volume Rendering of Tibia

- i) Select "update mesh" in the bottom left window in ITK-Snap (Figure 35). The volume rendering of the tibia should appear in that window.

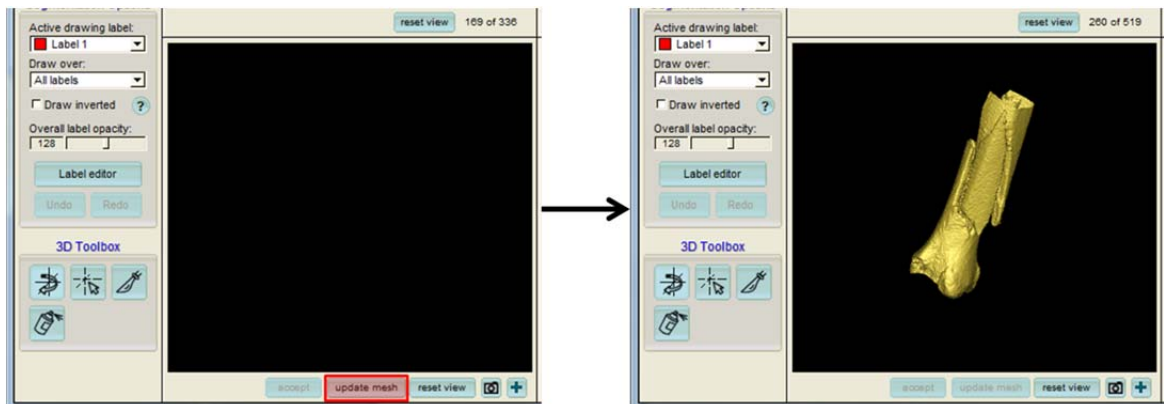


Figure 35: Updating Segmentation Mesh

e) Setup for Tibia Adjustments

(Refer to Figure 36 for the location of mentioned tools)

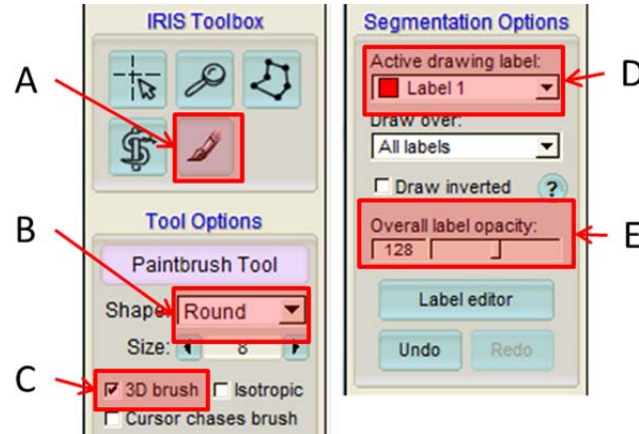


Figure 36: ITK Toolbar: (A) Paintbrush (B) Paintbrush Shape (C) 3D Brush Checkbox (D) Active Label (E) Label Opacity

- i) Select the Paintbrush on the IRIS Toolbox (Figure 36A). The paintbrush will be used to manually add to or erase from the segmentation.
 - ii) Select the shape of the paintbrush (Figure 36B). The suggested shape is round, but square can also work.
 - iii) Select for the paintbrush to be a 3D brush (Figure 36C). This is not required, but it does help reduce the work on every slice of the image.
 - iv) Be sure that the label of the tibia is chosen in the active label (Figure 36D). The label color is the same color as the color of the mask in the windows. It is often 1 or the highest numbered label.
 - v) If necessary, adjust the opacity of the label so that both the image and label can be seen (Figure 36E).
- f) Make Necessary Adjustments to the Tibia Label.**
Suggestion is to edit the label in the transverse plane (upper left window in ITK-Snap).
- (1) To add to the label, use the left mouse button.
 - (2) To remove from the label, use the right mouse button.
- (NOTE: If removing label be sure to remove the entire unwanted label. Any small portion of the label remaining may affect the end results. After all removal is done, it is often helpful to update the mesh and review the 3D volume for possible portions missed.)*
- g) Save the Adjusted Segmentation**
- i) After all adjustments are complete, proceed to “Segmentation” then “Save As Image...”
 - ii) Figure 33 should appear. Select “Browse...” and navigate to the Fracture NifTi folder again.
 - iii) Locate the “Fracture_Tibia” file and overwrite the previous file with the updated segmentation.
 - iv) Close the ITK-Snap program once all manual edits are complete.

4) Run the Second Section of Code

(This process will be repeated for each patient that was manually edited).

To run a section of code, click the section (section should become highlighted in yellow), and press CONTROL+RETURN.

a) **Input Approximations for Manual Edits**

- i) Figure 37 will appear. Input an approximation of the time taken for editing the patient mentioned.

b) **Segmentation Final Check**

- i) Figure 38 will appear for inspection of the segmentation. After inspection, close the window.
- ii) Figure 39 will appear. If no errors have been found, click “Yes.” If errors have been found, click “No” and refer back to “3) *Manually Edit Segmentations*” on page 104 and fix what is wrong with the segmentation at the completion of this section.

(If manual edits need to be redone, rerun this section at the completion of those edits.)

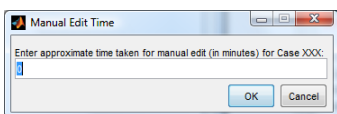


Figure 37: Time for Manual Edit Input

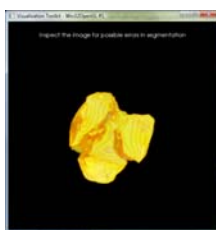


Figure 38: Final Segmentation Check

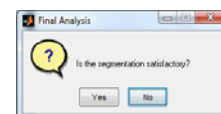


Figure 39: Satisfactory Segmentation Prompt

5) Run the Third Section of Code

This section requires no user intervention. Allow the code to run to completion for severity scores.

The final severity scores can be found in the variable “severity_score_list”. This list shows each patient’s initials along with their normalized Fracture Energy, Articular Comminution, and Dispersion severity scores. The final column shows the final combined severity score for each case.

6) Run the Fourth Section of Code (optional)

Run this section if:

The concordance values when compared to KL scores for each component (Fracture Energy, Articular Comminution, Dispersion, and Combined Score) are desired.

(Results found in fx_energy_conc, art_comm_conc, dispersion_conc, and combined_conc variables)

AND/OR

The p-values from a Wilcoxon Ranked Sum statistical analysis between cases that developed OA and those that did not are desired.

(Results found in fx_energy_p, art_comm_p, dispersion_p, and combined_p variables)

(Note: Only the cases that have a KL score listed will be used in the analysis.)

REFERENCES

1. Bernstein, J., et al., *Musculoskeletal medicine*. 1st ed. 2003, Rosemont, Ill.: American Academy of Orthopaedic Surgeons. xxiv, 490 p., 44 p. of plates.
2. Bonar, S.K. and J.L. Marsh, *Tibial Plafond Fractures: Changing Principles of Treatment*. J Am Acad Orthop Surg, 1994. **2**(6): p. 297-305.
3. Rosenberg, Z.S., J. Beltran, and J.T. Bencardino, *From the RSNA refresher courses - MR imaging of the ankle and foot*. Radiographics, 2000. **20**: p. S153-S179.
4. Sands, A., et al., *Clinical and functional outcomes of internal fixation of displaced pilon fractures*. Clin Orthop Relat Res, 1998(347): p. 131-7.
5. Seggl, W., R. Szyszkowitz, and W. Grechenig, *Tibial pilon fractures*. Current Orthopaedics, 1999. **13**(1): p. 42-52.
6. Kellam, J.F. and J.P. Waddell, *Fractures of the Distal Tibial Metaphysis with Intra-Articular Extension - Distal Tibial Explosion Fracture*. Journal of Trauma-Injury Infection and Critical Care, 1979. **19**(8): p. 593-601.
7. Lauge-Hansen, N., *Fractures of the ankle. V. Pronation-dorsiflexion fracture*. AMA Arch Surg, 1953. **67**(6): p. 813-20.
8. Hunter, T.B., L.F. Peltier, and P.J. Lund, *Radiologic history exhibit - Musculoskeletal eponyms: Who are those guys?* Radiographics, 2000. **20**(3): p. 819-836.
9. Blauth, M., et al., *Surgical options for the treatment of severe tibial pilon fractures: a study of three techniques*. J Orthop Trauma, 2001. **15**(3): p. 153-60.
10. Germann, C.A., et al., *Orthopedic pitfalls in the ED: tibial plafond fractures*. American Journal of Emergency Medicine, 2005. **23**(3): p. 357-362.
11. Borrelli, J. and E. Ellis, *Pilon fractures - Assessment and treatment*. Orthopedic Clinics of North America, 2002. **33**(1): p. 231-+.
12. Beardsley, C., J.L. Marsh, and T. Brown, *Quantifying comminution as a measurement of severity of articular injury*. Clinical Orthopaedics and Related Research, 2004(423): p. 74-78.
13. Bone, L., et al., *External Fixation of Severely Comminuted and Open Tibial Pilon Fractures*. Clinical Orthopaedics and Related Research, 1993(292): p. 101-107.
14. de Boer, P. and R. Metcalfe, *Pilon fractures of the tibia*. Current Orthopaedics, 2003. **17**(3): p. 190-199.
15. Ruedi, T.P. and M. Allgower, *The operative treatment of intra-articular fractures of the lower end of the tibia*. Clin Orthop Relat Res, 1979(138): p. 105-10.
16. Boehler, L. and E.W.H.b. Groves, [*Technik der Knochenbruchbehandlung.*] *The Treatment of Fractures*. 1935, Bristol: J. Wright & Sons.

17. Gay, R. and J. Evrard, [*Recent Fractures of the Tibial Pilon in Adults*]. Rev Chir Orthop Reparatrice Appar Mot, 1963. **49**: p. 397-512.
18. Dirschl, D.R. and G.L. Adams, *A critical assessment of factors influencing reliability in the classification of fractures, using fractures of the tibial plafond as a model*. J Orthop Trauma, 1997. **11**(7): p. 471-6.
19. Swiontkowski, M.F., et al., *Interobserver variation in the AO/OTA fracture classification system for pilon fractures: is there a problem?* J Orthop Trauma, 1997. **11**(7): p. 467-70.
20. Humphrey, C.A., D.R. Dirschl, and T.J. Ellis, *Interobserver reliability of a CT-based fracture classification system*. J Orthop Trauma, 2005. **19**(9): p. 616-22.
21. Ayeni, J.P., *Pilon Fractures of the Tibia - a Study Based on 19 Cases*. Injury-International Journal of the Care of the Injured, 1988. **19**(2): p. 109-114.
22. Ovadia, D.N. and R.K. Beals, *Fractures of the Tibial Plafond*. Journal of Bone and Joint Surgery-American Volume, 1986. **68A**(4): p. 543-551.
23. Resch, H., S. Pechlaner, and K.P. Benedetto, [*Long-term results after conservative and surgical treatment of fractures of the distal end of the tibia*]. Aktuelle Traumatol, 1986. **16**(3): p. 117-23.
24. Harris, J.H. and W.H. Harris, *The radiology of emergency medicine*. 4th ed. / John H. Harris, Jr., William H. Harris. ed. 2000, Philadelphia ; London: Lippincott Williams & Wilkins.
25. Helfet, D.L., et al., *Intraarticular "pilon" fracture of the tibia*. Clin Orthop Relat Res, 1994(298): p. 221-8.
26. Brown, T.D., et al., *Posttraumatic osteoarthritis: A first estimate of incidence, prevalence, and burden of disease*. Journal of Orthopaedic Trauma, 2006. **20**(10): p. 739-744.
27. Bone, L.B., *Fractures of the tibial plafond. The pilon fracture*. Orthop Clin North Am, 1987. **18**(1): p. 95-104.
28. *Osteoarthritis of the Ankle*. 2010 [cited 2012 04/30]; Available from: <http://www.therafit.com/Injuries-Conditions/Ankle/Ankle-Issues/Osteoarthritis-of-the-Ankle/a~122/article.html>.
29. *Ankle Arthritis*. 2008 [cited 2012 04/30]; Available from: <http://footcareexpress.com/foot-orthotics/ankle-arthritis/>.
30. *Regenexx-SD Ankle Arthritis Testimonial*. 2010 [cited 2012 04/30]; Available from: <http://www.regenexx.com/2010/11/regenexx-sd-ankle-arthritis-testimonial/>.
31. Finerman, G., et al., *Biology and biomechanics of the traumatized synovial joint : the knee as a model*. 1992, Rosemont, IL: American Academy of Orthopaedic Surgeons. xv, 597 p.
32. Donohue, J.M., et al., *The Effects of Indirect Blunt Trauma on Adult Canine Articular-Cartilage*. Journal of Bone and Joint Surgery-American Volume, 1983. **65**(7): p. 948-957.

33. Brown, T.D., et al., *Contact stress aberrations following imprecise reduction of simple tibial plateau fractures*. J Orthop Res, 1988. **6**(6): p. 851-62.
34. Kim, H.A., et al., *Apoptotic chondrocyte death in human osteoarthritis*. Journal of Rheumatology, 2000. **27**(2): p. 455-462.
35. Marsh, J.L., et al., *Articular fractures: Does an anatomic reduction really change the result?* Journal of Bone and Joint Surgery-American Volume, 2002. **84A**(7): p. 1259-1271.
36. Marsh, J.L., D.P. Weigel, and D.R. Dirschl, *Tibial plafond fractures - How do these ankles function over time?* Journal of Bone and Joint Surgery-American Volume, 2003. **85A**(2): p. 287-295.
37. Burgess, A.R., et al., *Lower-Extremity Injuries in Drivers of Airbag-Equipped Automobiles - Clinical and Crash Reconstruction Correlations*. Journal of Trauma-Injury Infection and Critical Care, 1995. **38**(4): p. 509-516.
38. Rockwood, C.A., et al., *Rockwood and Green's fractures in adults*. 5th ed. / editors, Robert W. Bucholz, James D. Heckman. ed. 2001, Philadelphia ; London: Lippincott Williams & Wilkins.
39. Sirkin, M. and R. Sanders, *The treatment of pilon fractures*. Orthopedic Clinics of North America, 2001. **32**(1): p. 91-+.
40. Borrelli, J., et al., *Effect of impact load on articular cartilage: Development of an intra-articular fracture model*. Journal of Orthopaedic Trauma, 1997. **11**(5): p. 319-326.
41. Etter, C. and R. Ganz, *Long-Term Results of Tibial Plafond Fractures Treated with Open Reduction and Internal-Fixation*. Archives of Orthopaedic and Trauma Surgery, 1991. **110**(6): p. 277-283.
42. Thordarson, D.B., *Complications after treatment of tibial pilon fractures: prevention and management strategies*. J Am Acad Orthop Surg, 2000. **8**(4): p. 253-65.
43. Tornetta, P., et al., *Pilon Fractures - Treatment with Combined Internal and External Fixation*. Journal of Orthopaedic Trauma, 1993. **7**(6): p. 489-496.
44. Wyrsh, B., et al., *Operative treatment of fractures of the tibial plafond - A randomized prospective study*. Journal of Bone and Joint Surgery-American Volume, 1996. **78A**(11): p. 1646-1657.
45. Merchant, T.C. and F.R. Dietz, *Long-Term Follow-up after Fractures of the Tibial and Fibular Shafts*. Journal of Bone and Joint Surgery-American Volume, 1989. **71A**(4): p. 599-606.
46. Thomas, T.P., et al., *Objective CT-Based Metrics of Articular Fracture Severity to Assess Risk for Posttraumatic Osteoarthritis*. Journal of Orthopaedic Trauma, 2010. **24**(12): p. 764-769.

47. Kellgren, J.H. and J.S. Lawrence, *Radiological assessment of osteo-arthritis*. *Ann Rheum Dis*, 1957. **16**(4): p. 494-502.
48. Newton, T.E.E., *Radiology of the skull and brain. vol 5, Technical aspects of computed tomography*. 1981, St Louis: C V Mosby Co.
49. Prince, J.L. and J.M. Links, *Medical imaging signals and systems*. 2006, Upper Saddle River, NJ: Pearson Prentice Hall.
50. Ruff, C.B. and F.P. Leo, *Use of Computed-Tomography in Skeletal Structure Research*. *Yearbook of Physical Anthropology*, 1986. **29**: p. 181-196.
51. Eldevik, K., W. Nordhoy, and A. Skretting, *Relationship between sharpness and noise in CT images reconstructed with different kernels*. *Radiation Protection Dosimetry*, 2010. **139**(1-3): p. 430-433.
52. Anderson, D.D., et al., *Quantifying tibial plafond fracture severity: Absorbed energy and fragment displacement agree with clinical rank ordering*. *Journal of Orthopaedic Research*, 2008. **26**(8): p. 1046-1052.
53. Thomas, T.P., *Development and Implementation of CT-based Measures for Objective Fracture Severity Assessment*, in *Biomedical Engineering*. 2007, University of Iowa: Iowa City, IA. p. 105.
54. Rittinger, P.v., *Lehrbuch der Aufbereitungskunde in ihrer neuesten Entwicklung und Ausbildung systematisch dargestellt*. 1867: Berlin.
55. Beardsley, C.L., et al., *Interfragmentary surface area as an index of comminution severity in cortical bone impact*. *J Orthop Res*, 2005. **23**(3): p. 686-90.
56. Currey, J.D., K. Brear, and P. Zioupos, *The effects of ageing and changes in mineral content in degrading the toughness of human femora*. *Journal of Biomechanics*, 1996. **29**(2): p. 257-260.
57. Thomas, T.P., et al., *ASB Clinical Biomechanics Award Paper 2010 Virtual pre-operative reconstruction planning for comminuted articular fractures*. *Clinical Biomechanics*, 2011. **26**(2): p. 109-115.
58. Thomas, T.P., et al., *A method for the estimation of normative bone surface area to aid in objective CT-based fracture severity assessment*. *Iowa Orthop J*, 2008. **28**: p. 9-13.
59. Associates, W., *Anthropometric Source Book, Vol. I: Anthropometry for Designers*. 1978, Washington DC: National Aeronautics and Space Administration.
60. Kroon, D.J. *Image Edge Enhancing Coherence Filter Toolbox*. 2009 Sep 2010 [cited 2011; Available from: <http://www.mathworks.com/matlabcentral/fileexchange/25449-image-edge-enhancing-coherence-filter-toolbox>.